METAMORPHISM AND ELEMENT REDISTRIBUTION: INVESTIGATIONS OF AG-BEARING AND ASSOCIATED MINERALS IN THE ARCTIC VOLCANOGENIC MASSIVE SULFIDE DEPOSIT, SOUTHWEST BROOKS RANGE, NORTHWEST ALASKA

By

Bonnie Nell Broman

RECOMMENDED:

Dr. Kenneth Severin

Dr. Mary Keskinen

Dr. Rainer Newberry, Advisory Committee Chair

Dr. Paul McCarthy
Chair, Department of Geology and Geophysics

APPROVED:

Dr. Paul Layer
Dean, College of Natural Science and Mathematics

Dr. John Eichelberger
Dean of the Graduate School

4/22/14
Date

METAMORPHISM AND ELEMENT REDISTRIBUTION: INVESTIGATIONS OF AG-BEARING AND ASSOCIATED MINERALS IN THE ARCTIC VOLCANOGENIC MASSIVE SULFIDE DEPOSIT, SOUTHWEST BROOKS RANGE, NORTHWEST ALASKA

A

THESIS

Presented to the Faculty

of the University of Alaska Fairbanks

in Partial Fulfillment of the Requirements

for the Degree of

MASTER OF SCIENCE

By

Bonnie Nell Broman, B.S.

Fairbanks, Alaska

May 2014

Abstract

The Arctic Cu-Zn-Pb-Ag volcanogenic massive sulfide (VMS) deposit is the largest deposit in the Ambler Belt, SW Brooks Range. Electron microprobe and XRF examination of ~200 samples shows appreciable (>0.5 %) Ag present in galena, fahlore, and bornite; each contains variable Ag. Core logging and XRF analyses show that complex elemental zoning is present, consistent with folding but with only minor (cm-scale?) spatial metal migration.

Arctic galena averages 0.02 - 0.9 wt% Ag and displays a Bi-Ag correlation, indicating a coupled substitution of $Bi^{3+}$and Ag^{+} for Pb^{2+}. Fahlore $[(Cu,Ag)_{10}(Fe,Zn)_2(As,Sb)_4S_{13}]$ contains 0.1 -16 wt% Ag; variable As-Sb contents indicate a range from tennantite to tetrahedrite. Ag increases with Sb; high Ag is only present in tetrahedrite. FeS in sphalerite [(Zn,Fe)S] of ~0.5 to ~13 mol% shows spatial patterns, with higher FeS closer to graphitic rocks. FeS in sphalerite increases with decreasing fS_2; higher FeS sphalerite at Arctic is present with pyrrhotite, arsenopyrite and (Ag-rich) tetrahedrite.

Redistribution of Ag took place during regional metamorphism: the original high fS_2-fO_2 VMS assemblage was altered with conversion of barite to Ba silicates (loss of O_2 and S_2). Variable fS_2-fO_2 conditions caused by graphite in host rocks versus barite in VMS rocks caused variable Ag mineralogy.

Table of Contents **Page**

List of Figures **Page**

Page

Page

Page

List of Tables **Page**

List of Appendices

Page

Acknowledgements

This adventure began when I was 7…when I decided I wanted to become a geologist. And for that I have no one to thank other than my grandmother (my farmor), who loves geology just as much as I do now, for piquing my interest in this wonderful field! I spent the rest of my childhood striving to do my best in the various math and sciences in order to achieve my goal. So the first group of people I'd like to thank are all of my teachers, advisors, mentors—specifically the math and science folks—who pushed and guided me through my primary education. A special thanks goes out to Mr. Bob Williams, Currituck County High School Chemistry, for really opening my eyes to the world of chemistry and for making learning so much fun! As I continued my education toward one day becoming a geologist, I moved to the mountains of North Carolina to begin my college career at Appalachian State University—what better place to learn about rocks than in the middle of the oldest mountain range in North America! I was lucky to have had the opportunity to study under some really great geologists, so I want to thank y'all for contributing my geologic understanding and career.

I decided to try out a different industry (after spending a few years in the environmental field) and was lucky enough to have found Rainer Newberry's name while googling mineral exploration in Alaska. He put me in touch with one of his then-current graduate students, Stephanie Mrozek for a job opportunity. I want to thank Steph very much for getting me started and teaching me the ropes in exploration geology. I've learned a LOT of valuable lessons, both geologic and industry-wise, from you. Not only have we developed a strong working relationship, but you will always remain one of my dearest and closest friends…no matter our geographic distance! Thank you for all your support and patience, advice, and encouragement during long work days and grad school!

I'll always remember the day I first met Rainer Newberry. I was headed to the middle of nowhere Alaska, not knowing what was in store for me. I show up at the airport under the understanding that I was supposed to meet Rainer at the airport to fly out to the Nixon Fork mine…well I had no idea who he was or what he even looked like! I knew instantly the moment I saw him…pink shoes, pink shirt, crazy hair, field

pack…he is the picture perfect geologist. And as they say, the rest is history. I want to thank you Rainer from the bottom of my heart for being such an amazing advisor and mentor. Your willingness and eagerness to help any of your students out at the drop of a hat is truly amazing. Thank you for putting up with all my silliness over the years…and thank you very much for helping me start my career as an exploration geologist. I have truly learned an amazing amount from you and I can't say this enough, but...THANK YOU! You put me in contact with Evan Twelker, who helped me get involved with this great project that developed into my Master's research—Arctic! Thank you, Evan, for everything you've helped me out with and all your advice and support…you really are great!

Speaking of Arctic, I want to thank NovaCopper for all the financial support, both tuition assistance and providing consistent work for me for the last 4 years. I want to thank all the geologic staff (Evan Twelker, Scott Petsel, Stuart Morris, Andy West, Kim Streeter, Joe Piekenbrock, and Rick van Nieuwenhuyse…among many others) who have been involved with the project for the length of time I've been there. Each of you has provided a great deal of advice, and ideas, and valuable discussions regarding my work. Rick—thank you very much for reviewing my thesis and providing your insightful comments and suggestions...and educating me about the price of tea in China!

A very special thank you to my committee: Dr. Rainer Newberry, Dr. Ken Severin, and Dr. Mary Keskinen. I couldn't haven't gotten through all the paperwork without your help and reminders!! And thank you for all of your hard work and valuable comments on this thesis. Thank you especially to Ken and all of his help and the help of all staff at the AIL (Advanced Instrumentation Lab)…I definitely couldn't have gotten through my enormous sample and data sets without you guys!

I'd like to thank my family and friends for all of their love and support. For everyone who has stood by my side and backed me up, encouraging me that I can finish; thank you very much. Your love and support always came through at the right times. Most importantly, thank you to my Fairbanks family—Jill Kooistra and Michelle Deal. You metals are truly special and I'm very grateful that we were all in this together! I

couldn't have made it through all the late night geochem or geostat homeworks without our combined crazy conversations and your endless supplies of comic relief! We really had a great time…and it's just the tip of the iceberg! We've many more nights of fun and geologic adventures ahead of us! I look forward to working with you two in the future! Thank you very very very much you two for being there for me. I love you guys!

Chapter 1 Introduction

1.1 The Arctic VMS Deposit

The Arctic volcanogenic massive sulfide (VMS) deposit is a poly-metallic deposit characterized by massive to semi-massive lenses of sulfide mineralization enriched in Cu, Zn, Pb, Ag, and Au. My thesis is meant to characterize ore mineralogy and bulk metal distributions throughout the Arctic deposit by investigating metal content, mineral associations, and metal distributions using geometallurgical and mineralogic techniques. Once characterized, I intend to better understand what causes the variations seen. I use these results in a larger framework of geometallurgical modeling to provide a base for predicting mineral process performance and mine planning considering the geological variability of the ore.

1.2 Location

The Arctic VMS deposit, hereafter referred to as Arctic, is located approximately 400 kilometers northwest of Fairbanks, Alaska and approximately 220 kilometers east of Kotzebue, Alaska. Arctic is the largest and highest grade deposit identified to date within the Ambler VMS Belt. The Ambler VMS Belt is defined by multiple metamorphosed VMS deposits and is hosted within the Ambler Sequence. The Ambler VMS Belt trends east-west for over 110 kilometers along the southern flank of the Brooks Range. Arctic is centrally located within the Ambler VMS Belt approximately 36 kilometers northeast of the village of Kobuk, Alaska (Figure 1.1).

Figure 1.1: Site location map. The Arctic VMS deposit is located ~400km NW of Fairbanks AK and is centrally located within the Ambler VMS belt.

The mineral rights for the majority of the Ambler District are controlled by NovaCopper Inc. (Figure 1.1), although Teck Resources Ltd. controls the Smucker deposit located at the western extremity of the district and Andover Mining Corp. controls the Sun deposit located at the eastern extremity of the district. The Arctic deposit has an indicated resource of 23.8 million tonnes (Mt) at 3.26% Cu, 4.45% Zn, 0.76% Pb, 53.2 g/t Ag, and 0.71 g/t Au and an inferred resource of 3.4 Mt at 3.22% Cu, 3.84% Zn, 0.58% Pb, 41.5 g/t Ag, and 0.59 g/t Au (Wilkins et al., 2013).

1.3 Geology of the Ambler District

The Ambler District experienced hydrothermal alteration in the Devonian (Schmidt, 1988), blueschist-greenschist metamorphism in the Jurassic (Dusel-Bacon et al., 1989), and multiple episodes of folding and deformation from the Jurassic through the Cretaceous (Newberry et al., 1997). Rocks of the Ambler VMS Belt experienced a single blueschist to greenschist facies P-T event, reflecting tectonic loading followed by decompression. Dusel-Bacon et al. (1989) reports the last greenschist metamorphic phase resulted in a semi-penetrative cleavage (defined by the alignment of

muscovite+chlorite and dislocations in the S1 foliation). The rocks contain post-kinematic helicitic albite porphyroblasts, randomly oriented biotite, and partial to total replacement of garnet by chlorite. K-Ar dating on metamorphic micas suggests early-mid Cretaceous cooling ages (Dusel-Bacon et al, 1989).

The Ambler Sequence—comprised of about two-thirds felsic plus mafic metavolcanic rocks and one-third metasedimentary rocks—is the host for VMS mineralization (Figure 1.1). Metarhyolite commonly contains blue quartz eyes and feldspar megacrysts and is spatially associated with mineralization. Metamafics are typically massive pods or lenses 700-1850m thick. Metasedimentary rocks are distinguished primarily by non-igneous mineralogy and include calcareous, pelitic, and carbonaceous schist (Till et al., 2008).

U-Pb ages of 378-386 Ma from metarhyolite are consistent with conodont ages of mid to late Devonian (Till et al., 2008). Feldspar-phengite thermobarometry from a metarhyolite sample indicates temperature and pressure of 376 ºC and 10.3kb (Patrick 1995); Schmidt (1983) suggests a pressure of ~6kbar. These are consistent with conditions near the greenschist/blueschist boundary, and are compatible with the presence of the high-pressure mineral cymrite (a Ba phyllosilicate) and metamorphic conditions implied by the silicate assemblages and composition (Hsu, 1994; Abbott and Bandy, 2008). Schmidt (1986) suggests low fluid/rock ratios during metamorphism and limited elemental migration.

1.3.1 Arctic Geologic Units

The geologic units at Arctic are complexly interfingered and deformed (Figures 1.2 and 1.3). Five ore zones containing 1-18 meter thick semi-massive to massive sulfide lenses are present (Wilkins et al., 2013). The mineralization is associated with rocks interpreted as altered metavolcanic and is typically bounded by graphitic rocks (Figure 1.3).

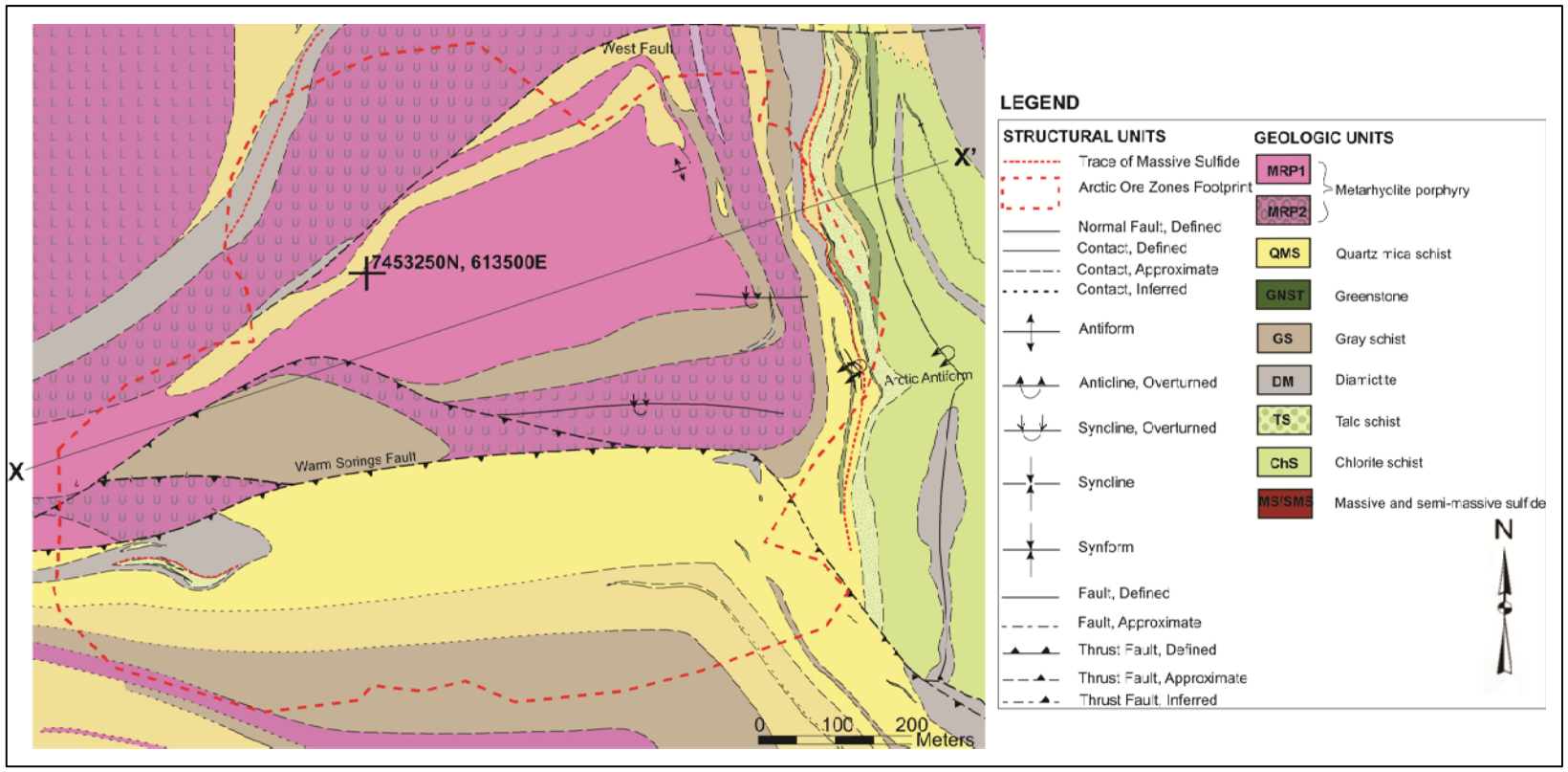

Figure 1.2: Local geologic map of the Arctic VMS deposit. The mineralized footprint is outlined in a red dashed line. UTM coordinate grid, NAD83, zone 4. Cross-section X-X' is shown in Figure 1.3. Modified from unpublished NovaCopper data.

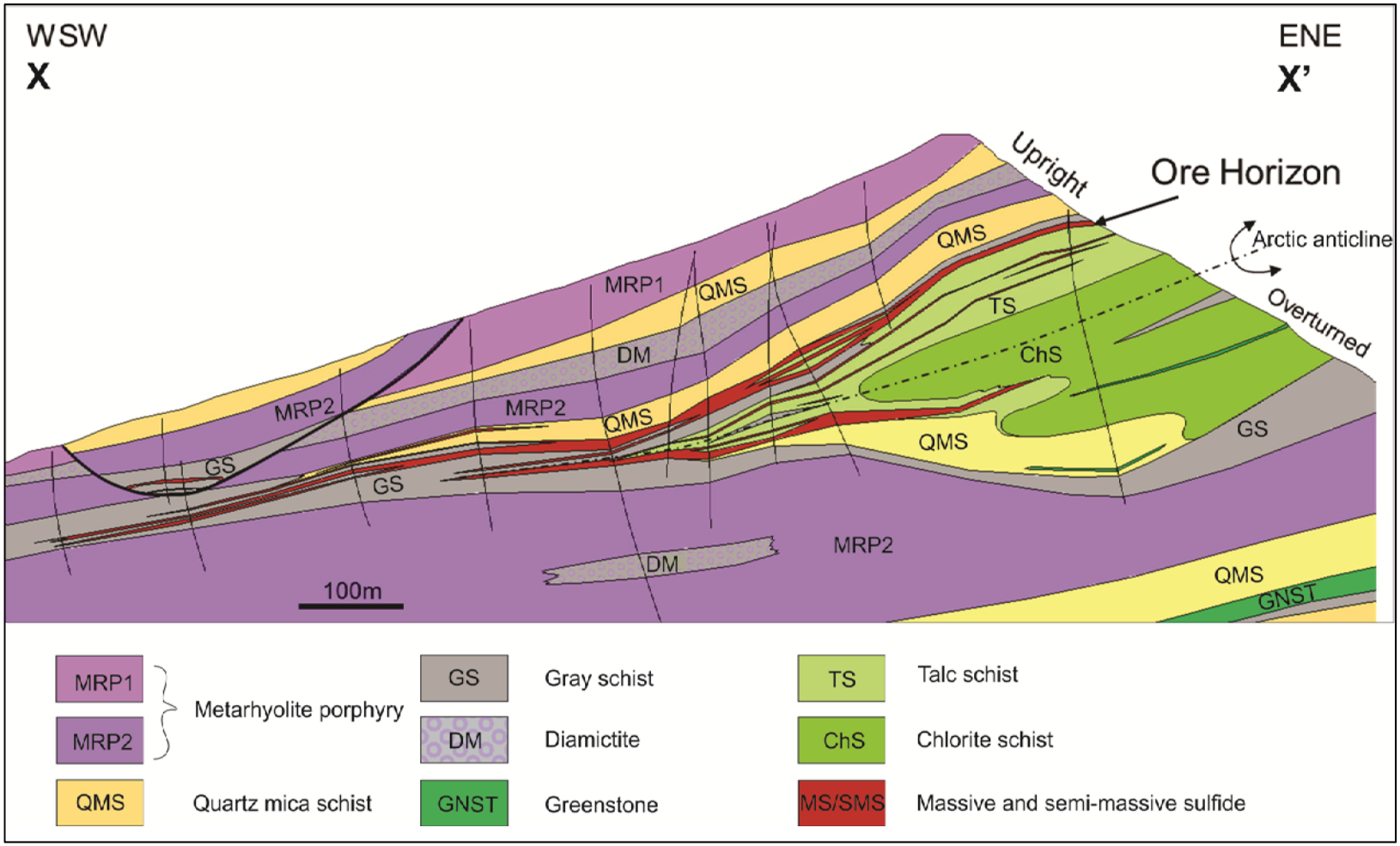

Figure 1.3: Cross-section of the Arctic VMS deposit and associated geologic units. View direction to the northwest. Modified from unpublished NovaCopper data.

Rocks interpreted as metasedimentary include a Gray Schist (GS) unit defined by ~1-10% graphite with disseminated pyrite + pyrrhotite, and a Diamictite (DM) unit characterized by meta-rhyolite porphyry (MRP) clasts in a sedimentary matrix.

Rocks interpreted as metafelsic include Quartz Mica Schist (QMS) and Meta-Rhyolite Porphyry MRP. QMS contains albite porphyroblasts in a gray-green quartz-mica groundmass. MRP contains quartz and feldspar megacrysts in a schistose matrix. Two varieties (MRP1 and MRP2; Figure 1.3) are distinguished based on their immobile elemental compositions (Twelker, 2008). Greenstone (GNST) consists of fine-grained plagioclase, amphibole, chlorite, epidote, white mica, and quartz $\pm$ garnet. Chlorite Schist (ChS) and Talc Schist (TS) are interpreted as metasomatically altered rocks of several types, characterized by abundant chlorite and talc, respectively.

Massive (>50% sulfide minerals) and semi-massive (30-50% sulfide minerals) sulfide are both dominated by pyrite (py). Other major minerals include chalcopyrite (cpy), sphalerite (spl), galena (gal), tetrahedrite-tennantite (tet-tn), bornite (bn), and pyrrhotite (po). Accessory ore minerals include arsenopyrite (asp), magnetite (mag), and electrum. Textures and grain sizes depend on the mineral. Typically py is massive and porphyroblastic; cpy, gal, and spl are disseminated and finer-grained. Tet-Tn occurs as disseminated blebs or in veinlets associated with cpy. Compositional banding is variably present.

1.3.2 Local Structural Framework

Early workers (e.g., Russell, 1977, 1995; Schmidt, 1983) treated mineralization at the Arctic Deposit as part of an upright stratigraphic sequence. Subsequent reinterpretation (Wilkins et al., 2013) suggested the entire Ambler Sequence at Arctic is overturned. Proffett (1999) suggested an F2 fold with mineralization as part of an isoclinal anticline (Figure 1.3). That is, the two major ore horizons are actually one that is folded onto itself. Lindberg (2004) called this fold the Arctic Antiform (Figures 1.2 and 1.3) but interpreted it to be an F1 fold. He further suggested multiple folding of two

main mineralized horizons as opposed to numerous individual mineralized beds (the model of Russell, 1977). Most workers support the recumbent arctic anticline model, but opinion varies concerning the orientation of the fold and the degree to which this fold is refolded and (or) thrust faulted. That is, in detail (Figure 1.3) more than two ore horizons are present; these are modeled as fold or thrust repeats. Major folding in the region is consistent with late-Jurassic/mid-Cretaceous Brooks Range contraction (Chutas, 2008).

1.3.3 Hydrothermal Alteration

Interpretation of hydrothermal alteration is complicated by the metamorphic over-printing. However, workers agree that the chlorite-rich and talc-rich units represent Mg-addition and Na-depletion during VMS formation. Based on immobile element ratios and residual textures, Schmidt (1988) and Twelker (2008) claim that these rocks are predominantly altered metarhyolite. Chlorite-rich and talc-rich rocks are currently interpreted (Figure 1.3) as underlying the ore zones and represent a feeder zone for VMS mineralization.

1.4 Arctic as a Kuroko-Type VMS Deposit

Most workers postulate that before metamorphism, Arctic resembled the unmetamorphosed Kuroko deposits of Japan. Overall bulk metal content of Kuroko and Arctic are comparable (Table 1.1) and support the thesis that these two deposits might have started life with similar mineralogy and form.

Table 1.1: Overall Bulk Metal Content of Typical Kuroko and Typical Arctic Sulfide

'AVERAGE'	Cu	Pb	Zn	Fe	Ca	Ba	Al
	Wt%						
KUROKO	3	1.8	11.6	12	1.3	15	1
ARCTIC	4.1	1.3	6.5	12	1.7	>10*	1.1
	Ag	**Bi**	**As**	**Sb**	**Au**	**Mo**	
	ppm						
KUROKO	199	52	2662	246	2.6	97	
ARCTIC	70	112	1238	257	1	14	

Data from Arctic compiled from Rigby et al., 2008 and unpublished assays. Data from Kuroko compiled from Glasby et al., 2008. *Arctic Ba numbers are based on limited barium assay data.

An idealized Kuroko deposit displays extensive metal and mineral zoning (Glasby et al., 2008; Figure 1.4). Barite, Pb, and Zn are more abundant in the upper and outer parts of the deposit ('black' and 'baritic' ores); Cu and silica are more abundant in the lower and central parts of the deposit ('yellow' and 'stockwork' ores). All the ores are dominated by pyrite. In addition (Lambert and Sato, 1974; Kitazono and Ueno, 2003; Glasby et al., 2008):

- Stockwork ore is quartz-rich with accessory chalcopyrite;
- Yellow ore contains chalcopyrite with occasional quartz;
- Black ore contains sphalerite, galena, chalcopyrite, bornite, pyrite, tetrahedrite-tennantite (fahlore), digenite, electrum, and barite; and
- Barite ore is mostly barite.

Finally, Kuroko sphalerite is Fe-poor, galena is Ag-poor, the silver is mostly hosted by Cu-Ag-sulfides, and bismuthenite is commonly found in these deposits (Kitazono and Ueno, 2003).

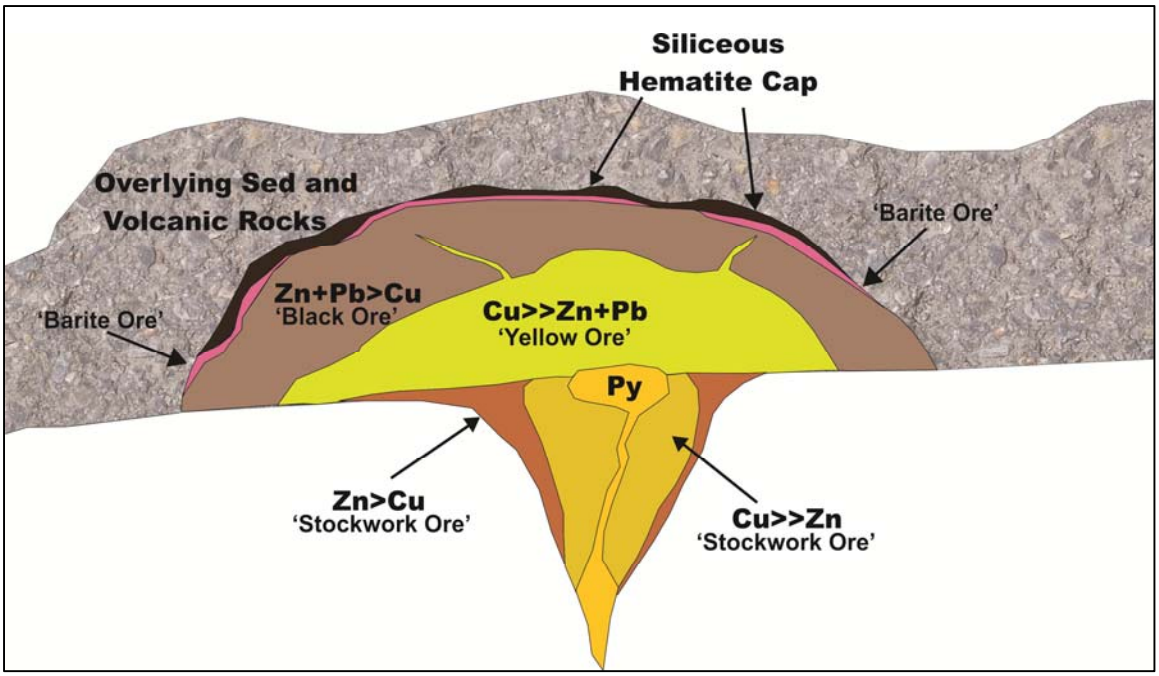

Figure 1.4: Illustration of representative metal zoning and ore zones in an unmetamorphosed Kuroko-style VMS deposit.

Although the metal contents of Arctic are quite similar to an average Kuroko deposit (Table 1.1), the mineralogy is quite different (Table 1.2). Stephens and Cameron (1970) reported that galena contains 0.1-0.3% Ag (and substantial Bi) and reported trace to 1% Ag in 'tennantite'. In addition, Arctic displays a mineralogical zoning not seen at Kuroko. By and large, low sulfidation state (fS_2) minerals—such as arsenopyrite and pyrrhotite—occur in the NW and the high fS_2 assemblage of bornite + pyrite is present in the SE (Schmidt, 1983; Figure 1.5).

Table 1.2: Summary Table Contrasting Mineralogy of Arctic with Typical Kuroko Deposits

KUROKO	ARCTIC
SULFIDES	
Low Fe Sphalerite	Variably high Fe Sphalerite
Ag-Cu sulfide minerals	
Galena (Ag absent)	Galena–argentiferous
Fahlore (low Ag)	Fahlore –variable Ag
Bornite	Local bornite
Pyrite	Pyrite porphyroblasts
Bismuthenite	+Arsenopyrite
	+Pyrrhotite
SILICATES/SULFATES	
Barite	Barite+Cymrite+Ba silicates
Sericite (muscovite)	Ba-Phengite
	Variable Fe-chlorite
Mg-Chlorite	+Ba-Phlogopite+Biotite
	+Talc

Kuroko mineralogic data modified from Lambert and Sato (1974), Urabe and Marumo (1991), Kitazono and Ueno (2003), and Glasby et al. (2008). Arctic mineralogical data modified from Schmidt (1983, 1988) and Schmandt (2009).

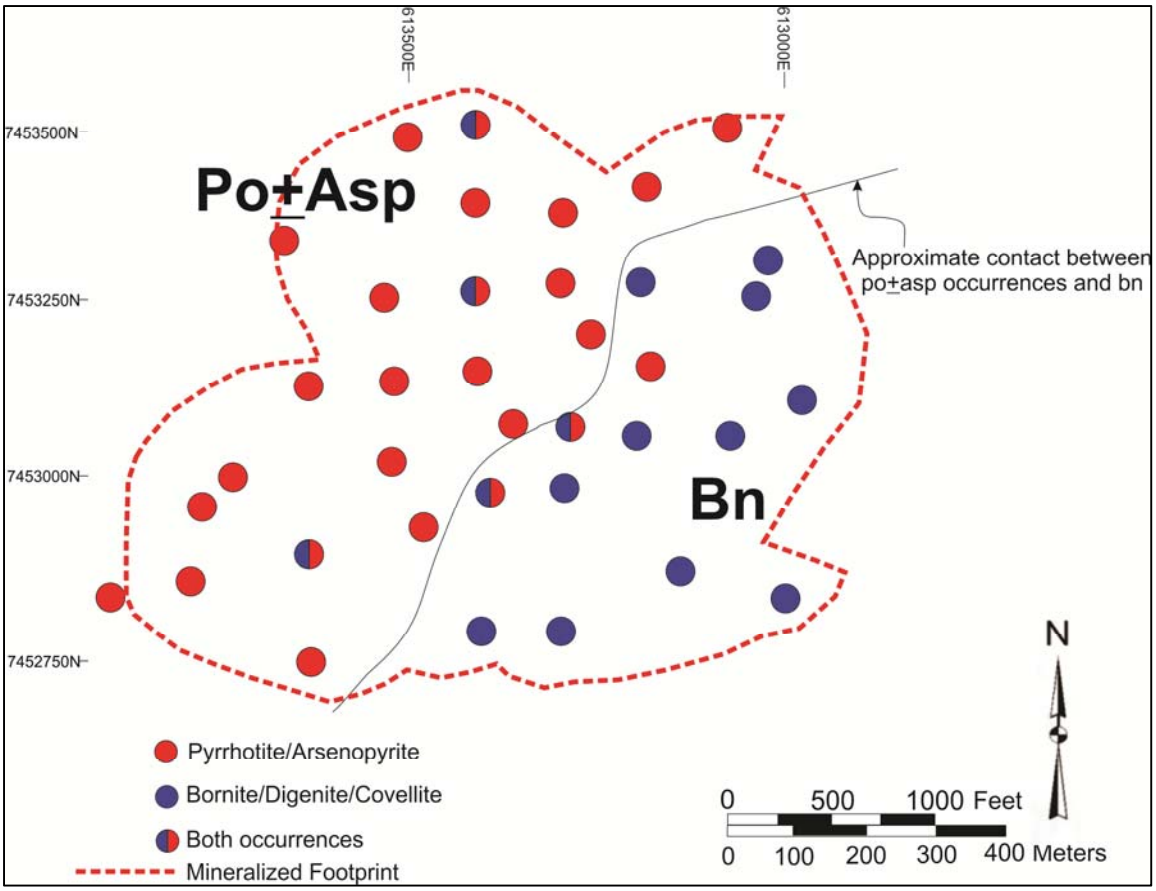

Figure 1.5: Schematic diagram modified from Schmidt (1983) displaying typical Arctic mineral assemblages. Low fS_2 minerals are present in the NW and high fS_2 minerals in the SE portion of the Arctic deposit (Po=pyrrhotite, Asp=arsenopyrite, Bn=bornite). UTM grid is NAD83, Zone 4.

1.5 Structural-Mineralogical Interpretations of the Arctic Deposit

Schmidt (1983) postulated that Arctic consisted of a series of stacked lenses, each zoned from a high oxidation state (fO_2)'core' to a low fO_2 margin, and that the zoning was due to chemical interaction between fluids debouched on the ocean floor and carbonaceous sediments. In contrast, the current model for VMS deposits (Lambert and Sato, 1974; Glasby et al., 2008) is that they are replacements under a sulfate mound. The current structural interpretation of Artic is that the multiple ore lenses are folded repeats (Figure 1.3) rather than stacked lenses. However there is no agreement about the structural details. Possible models include (1) one complexly folded horizon, (2) some combination of folding and low angle faulting of one horizon, and (3) multiple folded lenses.

An alternative to Schmidt (1983) regarding the mineralogy and mineralogical zoning at Arctic is that the minerals were originally similar to those associated with a Kuroko style deposit and that the processes associated with deep burial metamorphism changed their character and distribution. This would seem at least plausible given that the coarse, porphyroblastic pyrite noted by all workers (e.g., Schmidt, 1983, Schmandt, 2009) is widely accepted as a 'metamorphic' ore texture (e.g., Craig and Vokes, 1993). The most obviously redistributed element is barium, which occurs as barite, as cymrite [$BaAl_2Si_2(O,OH)_8*H_2O$], and as Ba-bearing muscovite, phlogopite, and biotite at Arctic (Schmidt, 1988; Schmandt, 2009). In contrast, Ba occurs exclusively as barite in Kuroko deposits. Barite requires relatively high fS_2 and fO_2 conditions, and turning it into a Ba-silicate releases significant S_2. Conversely, graphite requires and stabilizes low fO_2 conditions. Hence, conditions during metamorphism will vary—even at constant P,T—depending on the relative supply of graphite (reducing) versus barite (oxidizing).

1.6 Purpose of this Study

Previous work, based on limited samples, indicated major mineralogical differences between Arctic and the unmetamorphosed Kuroko deposits. My objective is to better quantify the mineralogy and mineral compositions at Arctic and to better define their spatial patterns. Of particular interest is the current distribution of Ag among the various phases and how that changes through the deposit. My working hypothesis is that elements have been redistributed (if only locally) during metamorphism and that variations in metamorphic oxidation and sulfidation states have influenced mineralogy and mineral compositions. I also investigate metal ratios to look for zonation patterns that represent some combination of original Kuroko deposit zoning and later metal redistribution. I employed data from previous studies (Schmidt, 1983 and Schmandt, 2009) in conjunction with new data to map the fS_2 and fO_2 conditions in the deposit.

1.7 Methodology and Analytical Techniques

Microprobe analyses were made from 195 Arctic deposit samples. Thirty two were single samples taken from individual drill holes (including 25 samples with some minerals previously analyzed by Schmandt in 2009). An additional 162 samples were taken from each of the five defined mineralized horizons within each of 4 drill holes. Samples were collected on a centimeter scale and quartered drill core was cut into small billets for petrographic studies (Figures 1.6 and 1.7). The samples taken represent a wide geographic area (Figure 1.6) and encompass all the various ore horizons (Figure 1.7). The cross-sections illustrate the structural complexity as a single overturned anticline but do not attempt to explain the relationship between the five sulfide-rich layers (Figure 1.7).

I analyzed these samples using a Cameca SX-50 electron microprobe at the Advanced Instrumentation Laboratory (AIL) at the University of Alaska (UAF). Samples were analyzed by Wavelength Dispersive Spectrometers (WDS) using a 25kV accelerating voltage and 40-100 nA beam current (Appendix 4). Analytical routines were calibrated using well-characterized mineral standards. Interferences between Pb and Bi and between As and Sb were taken into account. I employed two WDS routines, one of which included Ag, Bi, Sb, and As for investigating Ag in fahlore and galena. The other included Mn, Fe, Zn, and S for sphalerite. Most grains were analyzed 3-5 times and the results averaged. Table 1.3 gives approximate detection limits, based on replicate analyses of analytical blanks (e.g., Ag-free galena).

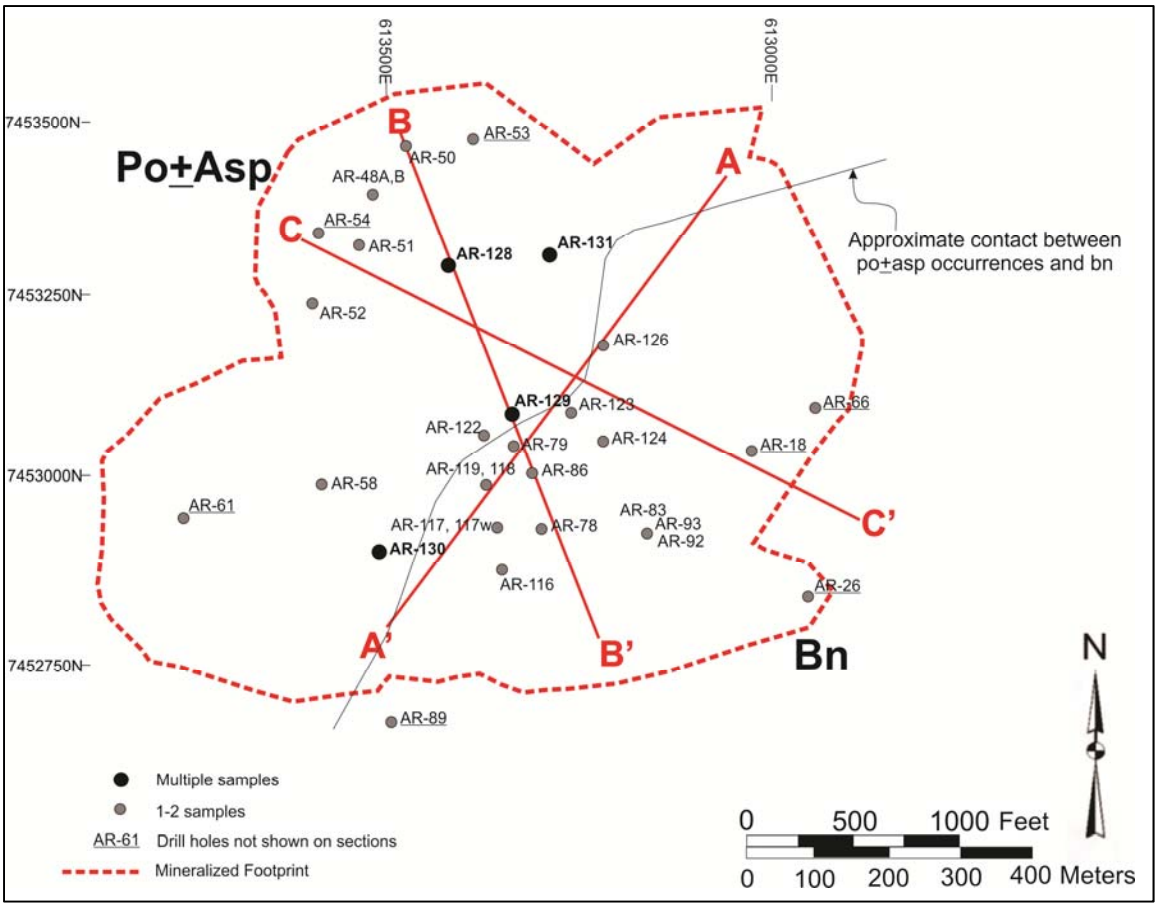

Figure 1.6: Sample location map. This map shows drill holes with multiple samples vs. 1-2 samples; the approximate Schmidt (1983) boundary between po±asp and bn occurrences; and cross-section lines. (Po= pyrrhotite, Asp= arsenopyrite, Bn= bornite). UTM grid is NAD83, Zone 4.

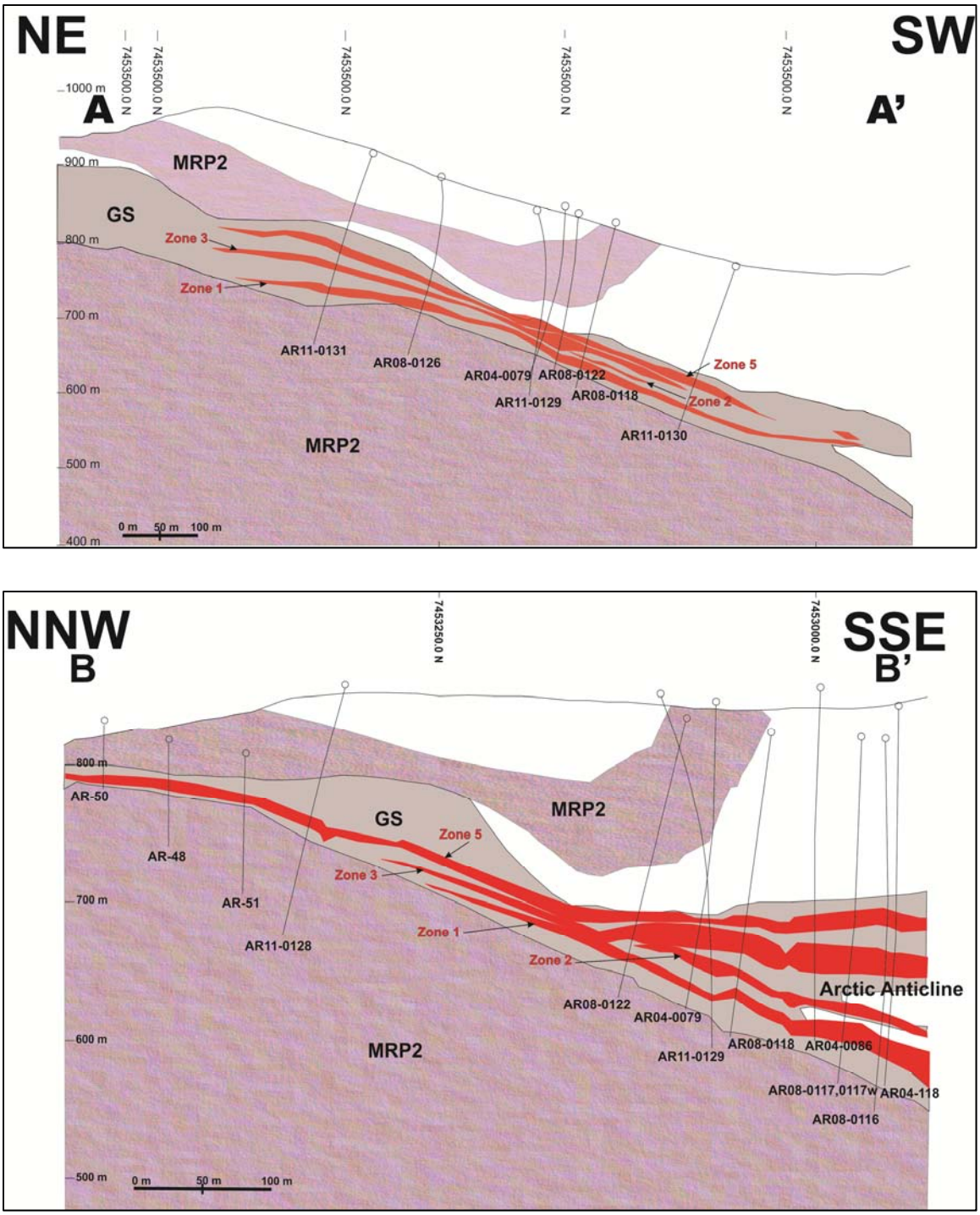

Figure 1.7: Cross-sections through the Arctic Deposit featuring drill holes sampled for this study. Red bodies represent sulfide ore horizons, defined as Zones 1-5. A-A' fold axis closure is not shown because the section is drawn parallel to the fold axis. White space represents other rock types. This figure is continued on the next page.

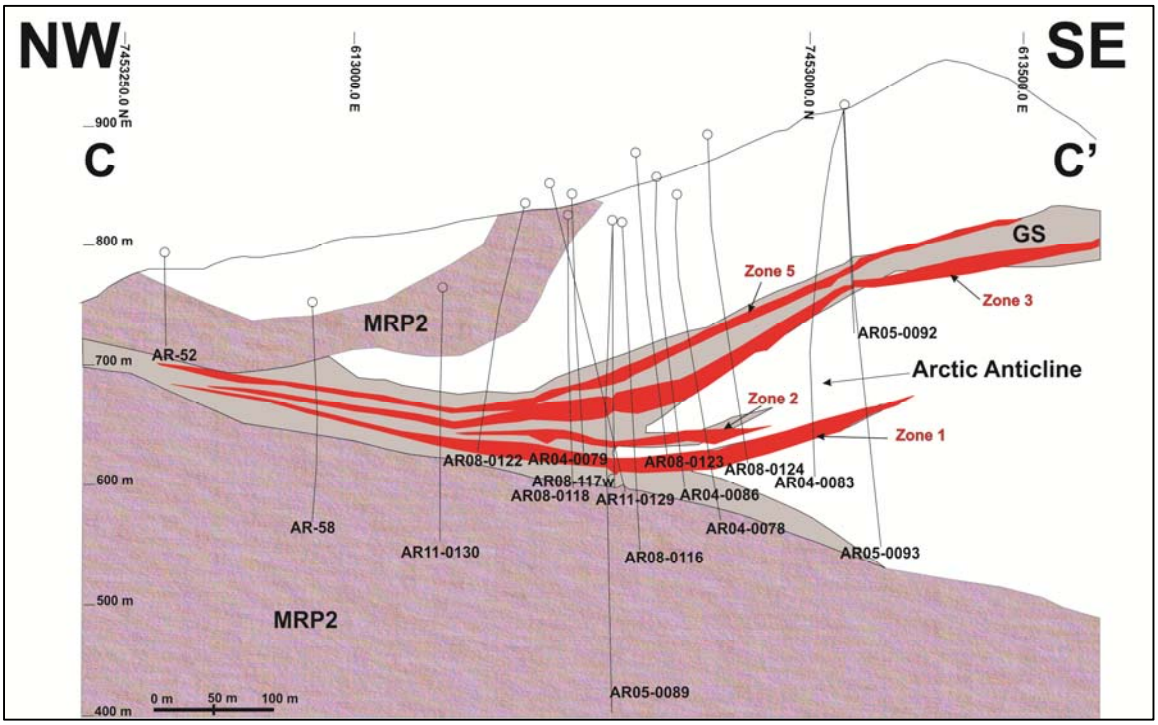

Figure 1.7 cont.: Cross-sections through the Arctic Deposit featuring drill holes sampled for this study. Red bodies represent sulfide ore horizons, defined as Zones 1-5. A-A' fold axis closure is not shown because the section is drawn parallel to the fold axis. White space represents other rock types.

Table 1.3: Analytical Detection Limits (Wt%)

Ag	Sb	Bi	As
0.08	0.05	0.19	0.08

Detection limits are three times the standard deviation for each element on pure Galena (PbS).

Pulverized pellets from crushed portions of 28 samples submitted for polished thin sections were made and analyzed using the PANalytical X-Ray Fluorescence (XRF) Spectrometer at UAF's Advanced Instrumentation Laboratory. Samples were chosen based on elevated Ag contents determined with a hand-held XRF analyzer. I made pulverized sulfide-rich pellets using 10 wt% MultiMix PXR 225 to act as a binding agent and assist with pulverization (van Zyl, 1982). I corrected values given by the PANalytical IQ+ software by employing results for international sulfide-rich standards KC-1 and MP-1.

Chapter 2 Metal Zoning and Fold Implications

2.1 Introduction

Unmetamorphosed VMS deposits display a characteristic shape and metal zoning (Lambert and Sato, 1974; Glasby et al., 2008) resulting from formation by hot water circulating through a growing sulfate-sulfide mound in a sub-marine environment. Typically, copper is more abundant in the underlying feeder/stockwork zone of the deposit whereas barite, Pb, and Zn are more abundant in the upper and outer parts of the VMS mound (Figure 1.4; Lambert and Sato, 1974; Kitazono and Ueno, 2003; Glasby et al., 2008). The overall deposit shape is that of a mushroom.

In contrast to unmetamorphosed Kuroko deposits, Arctic contains a series of separate sulfide lenses. From diamond drilling, these lenses are grouped into five "ore horizons," defined by possessing minable thickness, grade, and tonnage. Not all sulfide lenses are "ore horizons." Historically, each sulfide lens was viewed as a separate ore-forming event of debouching fluids onto the seafloor (e.g., Schmidt, 1983). Recognition of the overall vertical symmetry to the deposit with a near-identical felsic unit and graphitic phyllite above and below the zones of massive sulfide led to a model proposed by John Proffett (1999). Paul Lindberg (2004) further corroborated that the deposit was folded into a tight anticline, with the Cu-rich feeder constituting the core and southeast portion of the deposit (Figure 1.3). Based on the Kuroko model, a high Cu/Zn ratio with low total sulfur is characteristic of a VMS footwall feeder/stringer zone (Figure 1.4). Low Cu/Zn with high total sulfur and high Ba contents are characteristic of the massive sulfide mound containing the bulk of Pb and Zn (Figure 1.4) located immediately under the stratigraphic hangingwall.

Intense folding of VMS deposits is documented both elsewhere in the Ambler district (e.g., Newberry et al., 1997) and elsewhere in the world (Figure 2.1). However, the degree to which a single VMS deposit can be refolded is not well documented. Nor is it clear what the Arctic Deposit looked like before folding. Pre-folding models for

Australian deformed VMS deposits (Figure 2.1) vary from large massive sulfide and small Cu-stringer zones (Figure 2.1A, C) to an enormous stringer zone, sub-equal in extent to the massive sulfide (Figure 2.1B). I hypothesize, based on conversations with NovaCopper geologists, that the original, pre-folding stratigraphy and configuration at Arctic was something like that pictured in Figure 2.2. In this model, the footwall is variably altered, mostly metavolcanic rocks, the orebody is zoned from a lower zone of high Cu/Zn, footwall feeder/stringer style mineralization to an upper zone consisting of higher Zn, Pb, and Ba contents, capped by a graphitic mudstone designated as stratigraphic hangingwall rocks.

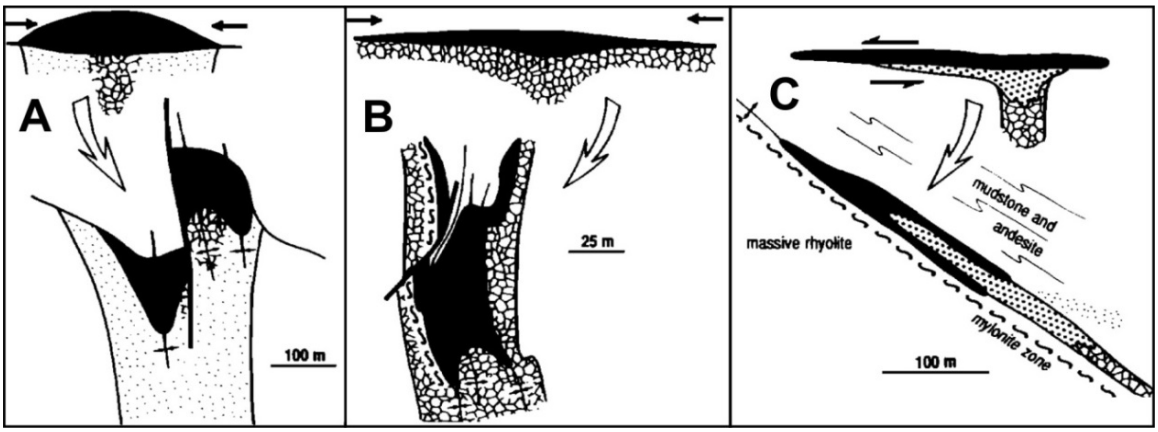

Figure 2.1: Representative cross-sections through folded and metamorphosed VMS deposits, showing postulated original cross-sections. A=Hellyer, B=Que River, C=Wilga, all in Australia. Black=massive sulfide, large stipple=Cu-pyrite, chickenwire=Cu-stringer zone, small stipple=footwall alterations. Modified from Large (1992).

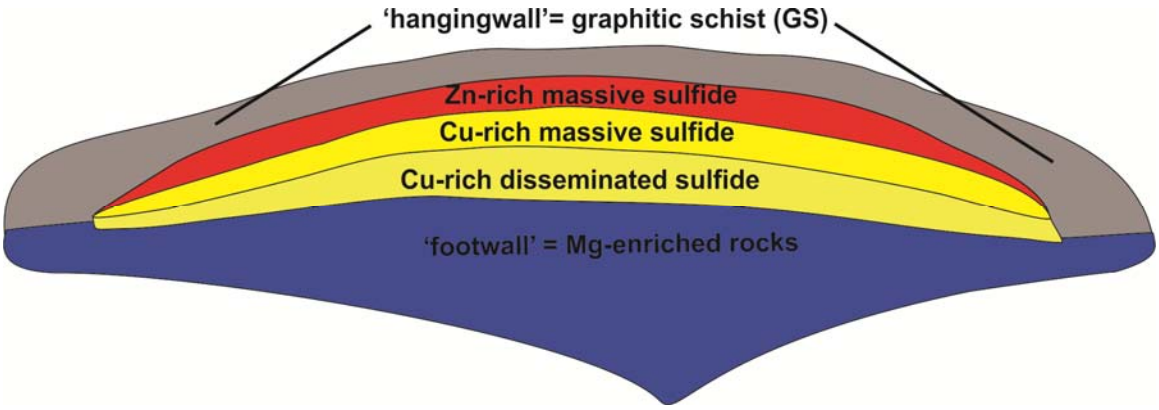

Figure 2.2: Theoretical model of the original pre-folding stratigraphy and configuration at Arctic.

However, a single isoclinal recumbent fold at Arctic should produce 2—not 5—ore horizons. Just how complicated is the folding? Folding of different styles and amplitudes is observed in the district (e.g., Figure 2.3A and B; Figure 1.2). Fold amplitudes range from less than 0.5 m (Figure 2.3A) to > 1 km (Figure 1.2). Based on these observations a single isoclinal recumbent fold model is almost certainly an oversimplification.

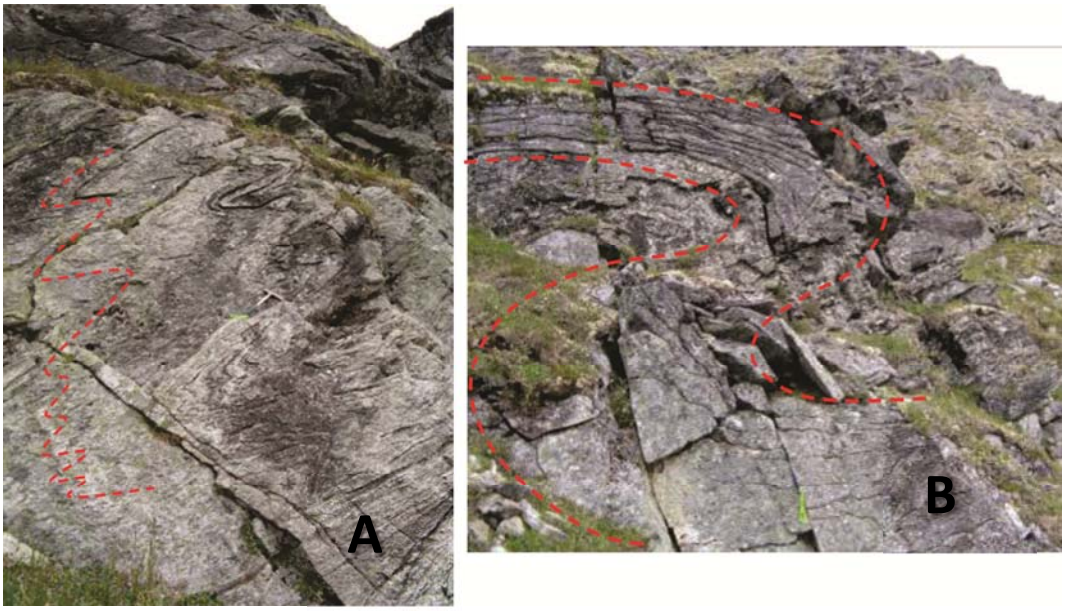

Figure 2.3: Examples of complicated folds observed on the east side of Arctic Ridge looking west. Folded horizons are drawn in red. A and B are approximately 4m and 10m wide respectively.

Most workers agree that Arctic fits a complex isoclinal recumbent fold model; however, the degree to which that fold is refolded and (or) thrust faulted is still under discussion. In this chapter, I examine metal ratios on a detailed scale in order to test the degree to which complex folding of my simple stratigraphic model can explain the configuration of the Arctic deposit. Essentially, can the ore horizons at Arctic be modeled as folded repeats of one horizon, isolated separate ore mounds, sheared repeats of the same horizon, or some combination of these?

One complication in applying the model of Figure 2.2 to Arctic is the consistent identification of the Gray Schist (GS) unit. This unit can be and has been confused with Quartz Mica Schist; a distinction based on qualitative assessment of 'greyness'. Recent

work (Twelker, 2008) has shown a compositional distinction, but such information is not readily available. Gray schist contains magnetic pyrrhotite (not always macroscopic) due to the metamorphism of pyrite in the presence of graphite (Hall, 1986; see also Chapter 3). Because the original footwall rocks were variably altered before metamorphism, their appearance is variable. The most reliable distinction of stratigraphic footwall from stratigraphic hangingwall (Figure 2.2) rocks (without compositional data) is the absence of graphite. Stratigraphic footwall rocks can be more reliably distinguished from stratigraphic hangingwall rocks, which have a more magnetic character. Consequently, I made detailed magnetic susceptibility measurements along with measuring metal concentrations to more reliably distinguish stratigraphic footwall and hangingwall rocks.

2.3 Methods

I used a Terraplus KT-9 Digital Magnetic Susceptibility Meter to measure magnetic properties in the rocks surrounding the ore zones. I made three measurements on a single piece of sawed core and averaged the results. Replicate measurements typically varied by less than 20%.

I examined metal zoning for four drill holes, AR11-0128, AR11-0129, AR11-0130, and AR11-0131, by using a handheld Thermo Scientific Niton XL3t XRF Analyzer. I employed the factory calibration which I checked with pressed pellet international standards. Concentrations >1% were within 10-20% of the amount present. The key difficulties are the extreme inhomogeneity of sulfides and the small (1 cm diameter) analysis area of the Niton Analyzer. A single analysis represents a 0.8 cm^2 area of the drill core, which might constitute a single pyrite porphryroblast. I worked around these problems by analyzing individual ~5-15cm pieces of sawed core and moving the Niton back and forth over the flat, sawed core surface for approximately 90 seconds. This technique is less accurate than a single analysis of a homogeneous sample, but yields reproducible results (Figure 2.4). I analyzed twenty 5-15 cm lengths of drill core 3 times over the course of a single day. Comparison of the results for major elements,

including Cu, Zn, Pb, S, and Ba (Figure 2.4), shows excellent reproducibility. This technique for collecting data for trace elements, such as Sb, Bi, and Ag, is less reproducible and was not further employed.

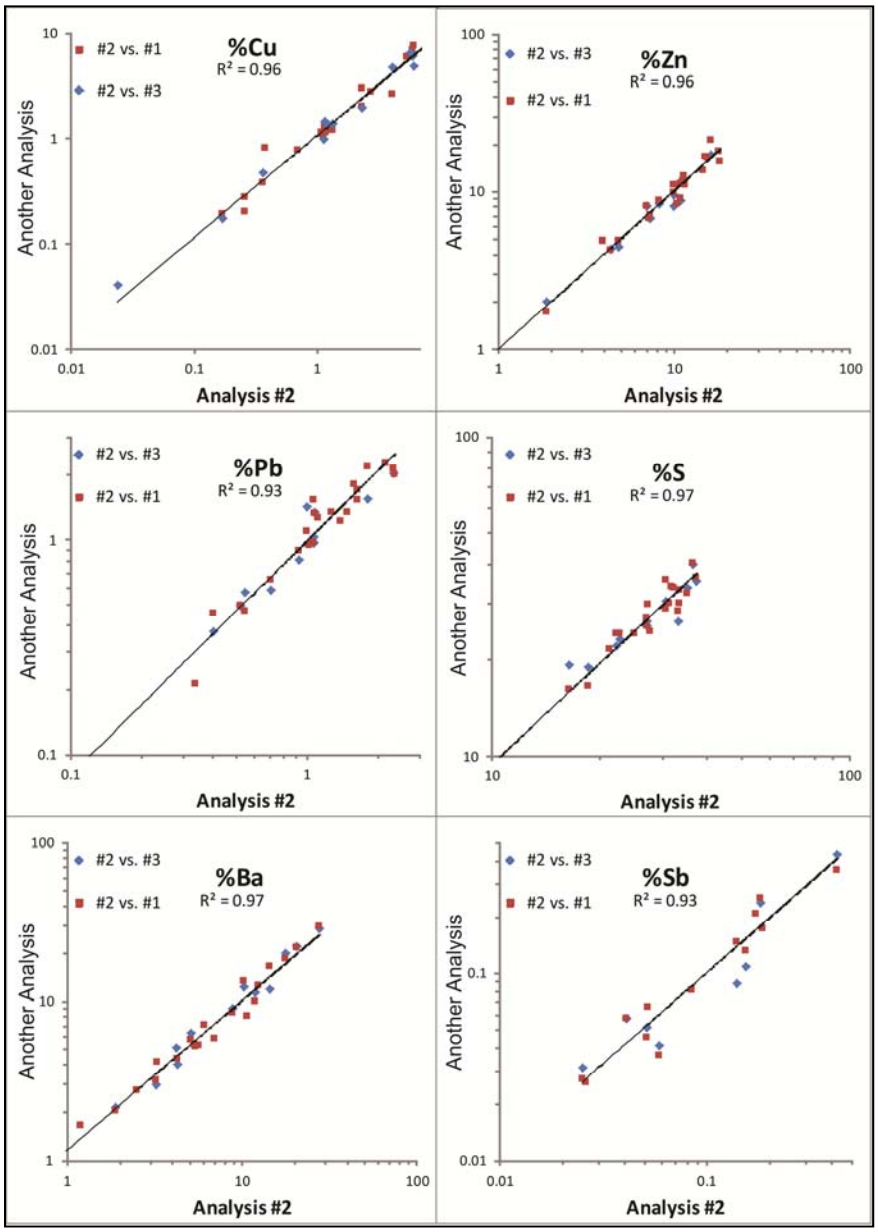

Figure 2.4: Niton reproducibility results for ~5-15cm lengths of core. Three analyses were separately made. Results for analyses 1 and 3 vs. 2 are shown for each. All values are in wt%. Replicated values agree within 10-20% for all but Sb.

2.3 Results

Figures 2.5 and 2.6 show that GS is magnetic (susceptibility generally > $1x10^{-3}$ SI), however, magnetic susceptibility drops approaching an ore zone. In contrast, footwall rocks (i.e, chlorite and (or) talc-rich schist, purple, Figure 2.6) yield magnetic susceptibilities of < 1 to <<1 x 10^{-3} SI. Massive sulfide horizons are variably magnetic due to the variable presence of magnetite and pyrrhotite.

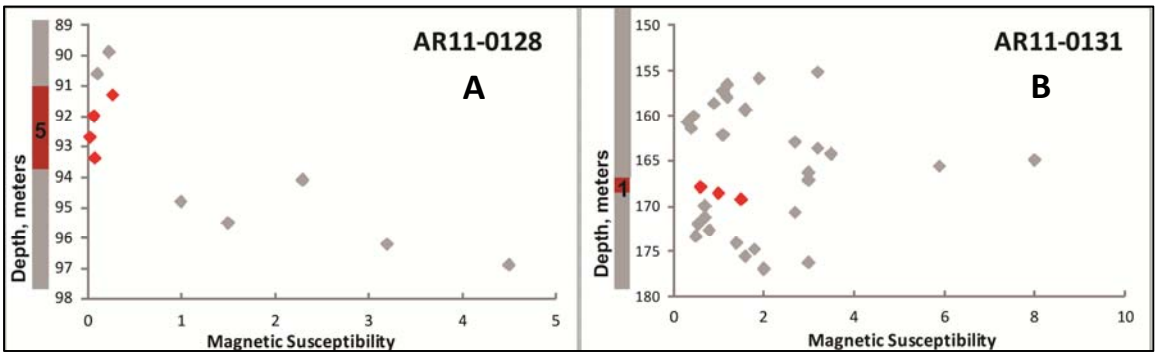

Figure 2.5: Magnetic susceptibility (SI units x 10-3) vs. depth for AR11-0128 and AR11-0131. GS intervals are indicated by gray boxes and ore zones are indicated by red boxes. GS shows high magnetic susceptibility due to the presence of pyrrhotite but generally drops approaching the ore horizon.

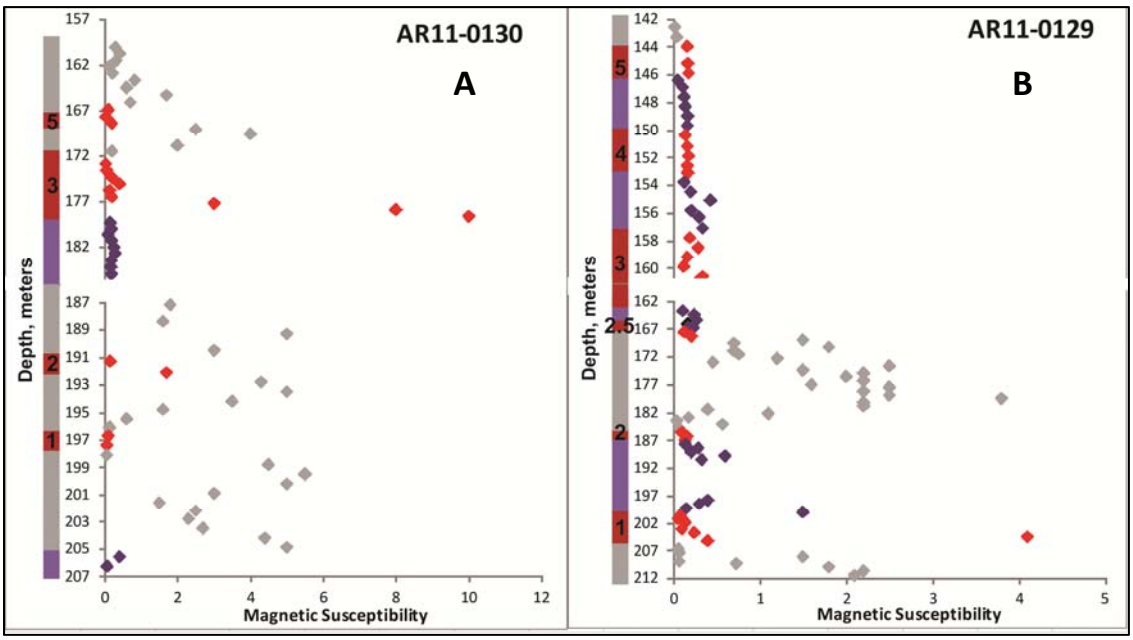

Figure 2.6: Magnetic susceptibility (SI units x 10 -3) vs depth for AR11-0129 and AR11-0130. GS intervals are indicated by gray boxes, ore zones by red boxes, and footwall rocks by purple boxes. Footwall rocks possess low magnetic susceptibility; ore zones are variably magnetic due to magnetite or pyrrhotite.

The variations in magnetic susceptibility (ms) above and below massive sulfide horizons confirm visually-determined identification of stratigraphic footwall and hangingwall rocks in the four drill holes. In particular, Zone 5 in drill hole AR-0128 (Figure 2.5A) and Zone 1 in drill hole AR-0131 (Figure 2.5B) do not show a simple asymmetric pattern expected for a simple sulfide lens. That is, the pattern is more complex than footwall (low ms) followed by ore (variable ms) followed by hangingwall (high ms) moving stratigraphically up through a section. Instead, stratigraphic hangingwall rocks (high ms) are present both above and below the ore (Figure 2.5B). The more complex drill holes AR-0130 and AR-0129 (Figure 2.6) show complicated patterns. In some cases massive sulfide layers are surrounded by stratigraphic footwall rocks (Zone 4 in AR-0129; Figure 2.6B), in some cases by stratigraphic hangingwall rocks (Zones 1 and 2 in AR-0130; Figure 2.6A), and in some cases they show the 'normal' stratigraphy of stratigraphic hangingwall rocks on one side and stratigraphic footwall rocks on the other (Zone 3 in AR-0130 and Zones 5, 2 in AR-0129; Figure 2.6). The lower two horizons of AR-0129 represent inverted stratigraphy—stratigraphic hangingwall rocks under massive sulfide (Zone 1, Figure 2.6B) under stratigraphic footwall rocks under massive sulfide (Zone 2, Figure 2.6B) under stratigraphic hangingwall rocks. In other words, Zones 1 and 2 in AR-0129 (Figure 2.6B) seemingly represent opposite limbs of an overturned recumbent anticline (Figure 2.7).

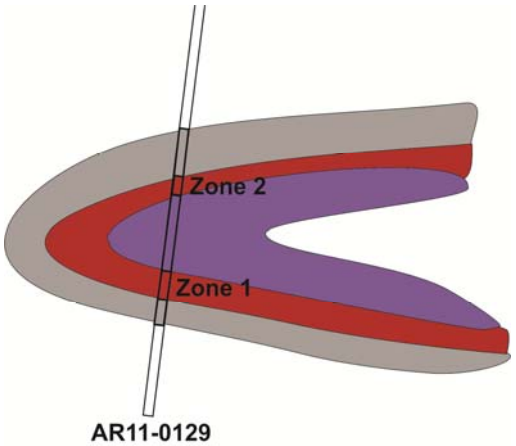

Figure 2.7: Zones 2 and 1 in AR11-0129 seemingly represent opposite limbs of an overturned recumbent anticline. See Figure 2.6B for magnetic susceptibility data.

Cu/Zn ratios and total metal contents show wide variations in each of the four drill holes, and generally support the complex models shown in Figures 2.5 and 2.6. If anything, the sulfide patterns are even more complicated than those suggested by the occurrence of hangingwall and footwall rock types. In particular, one would expect low Cu/Zn, high Ba, and high total sulfide to characterize ores near the stratigraphic hangingwall (GS) and high Cu/Zn, low Ba, and low total sulfide to characterize ores near the stratigraphic footwall. Because the Cu/Zn patterns seen are complex I describe them for each drill hole one at a time below.

AR-0128 contains one major ore horizon—Zone 5 (Figures 1.7 and 2.8). GS is present above and below this horizon (Figures 2.5 and 2.8). Figure 2.9 shows vertical changes in Cu/Zn ratio (A) and %S/100 (B)—that is total sulfur content—for this horizon. High Cu/Zn with low sulfur content, characteristic of a footwall feeder/stringer zone, alternates with Zn-rich (low Cu/Zn) massive sulfide zones. The low Cu/Zn (Zn-rich horizons) are adjacent to the stratigraphic hanging wall GS at both the upper and lower contacts, with another high sulfide, high Zn zone in the middle of the ore body (Figure 2.9). The highest Ba contents (up to 30%) are also in the middle massive sulfide zone. This data suggest that Zone 5 represents a complex series of overturned isoclinal folds and essentially a complex overturned anticline.

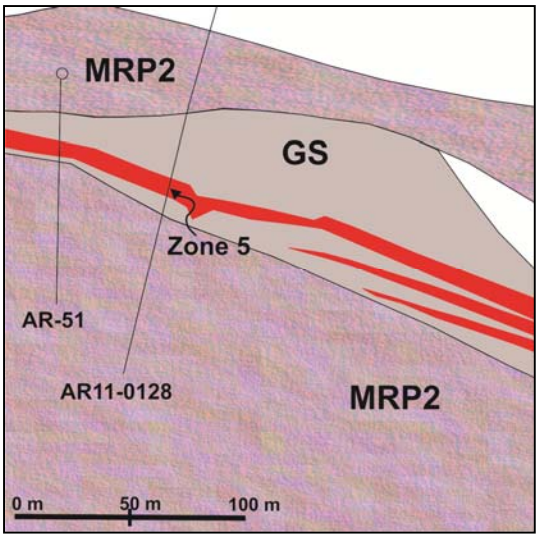

Figure 2.8: Cross-section through AR-0128. One ore zone (in red, Zone 5) is shown with gray schist (GS) present both above and below. Meta-rhyolite porphyry (MRP2) surrounds GS. See Figure 1.7 for cross-section location. White space represents other lithologies.

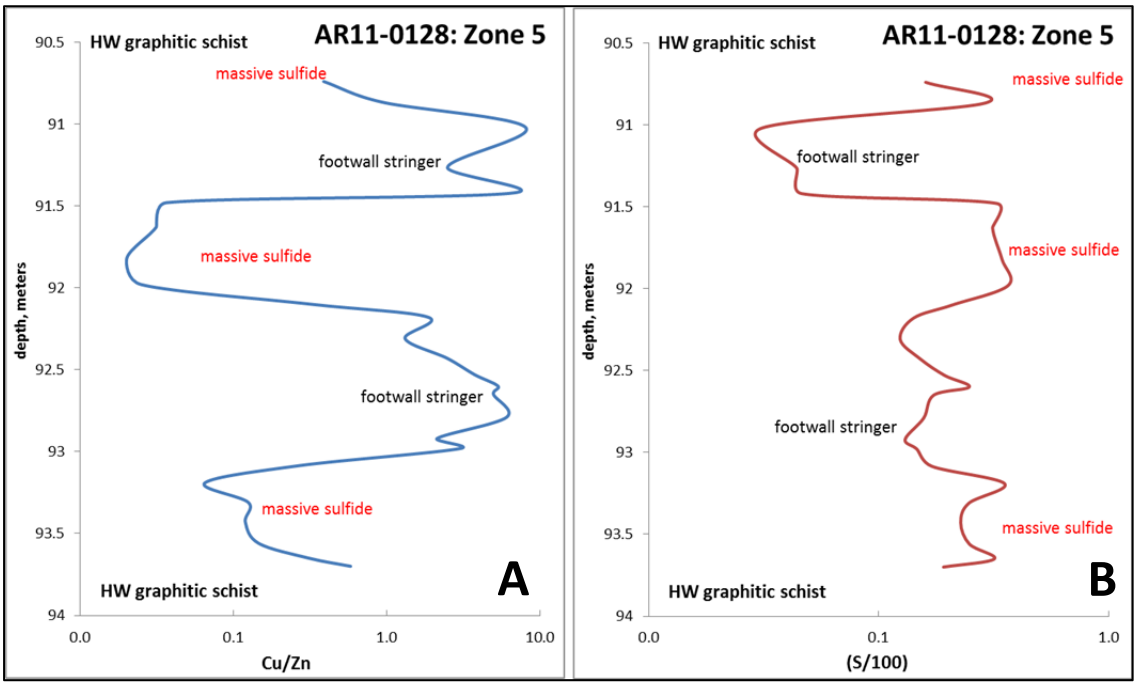

Figure 2.9: Compositional cross-section through massive sulfide in AR-0128. These graphs show apparent alternation between footwall and hangingwall associated ores determined using hand-held XRF, as described in the text. Cu/Zn = blue line (A); (S/100) = red (B).

AR-0131 contains three ore zones; the lowest one (Zone 1) is thickest and most significant (Figure 2.10). The other two zones consist of 20 cm of massive to semi-

massive sulfide, too thin for compositional zoning analysis. Both have low Cu/Zn ratios indicating proximity to hangingwall ore and both are surrounded by GS.

GS is present above and below Zone 1 in AR-0131 (Figures 2.5, 2.10). Figure 2.11 shows the vertical change in Cu/Zn ratios (blue line) and total sulfur (red line) in this zone. Each point represents the weighted average of two adjacent pieces of core; the total interval length for each point is 12-23 cm. Cu/Zn ratios are generally lower which is characteristic of the NW portion of the deposit. Vertically symmetric variations both in abundance of sulfide and Cu/Zn ratios are consistent with multiple isoclinal overturned folds.

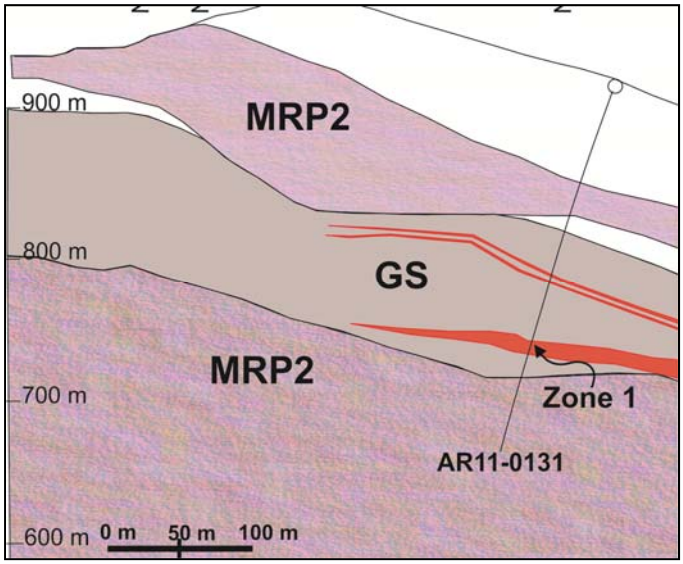

Figure 2.10: Cross-section through drill hole AR-0131. Three ore zones are surrounded by GS, in turn surrounded by MRP. Zone 1 accounts for the majority of sulfide; the upper two horizons are both 20 cm of massive to semi-massive sulfide. See Figure 1.7 for cross-section location. White space represents other lithologies.

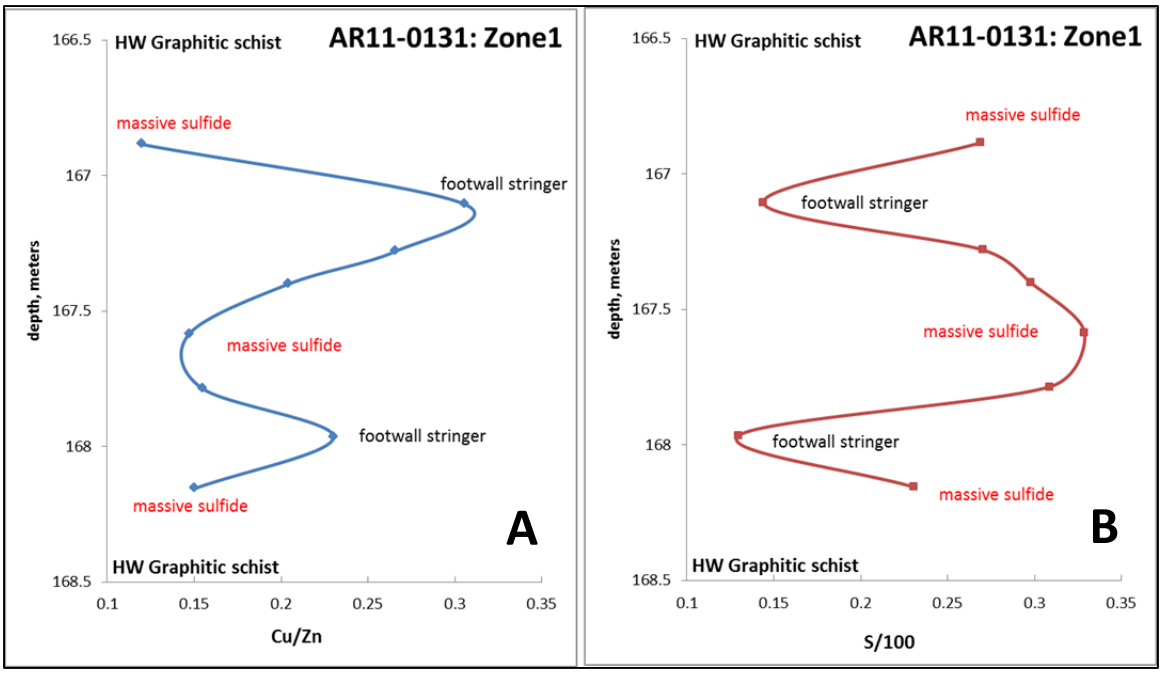

Figure 2.11: Compositional cross-section through massive sulfide Zone 1 in AR-0131. These graphs show apparent alternation between footwall and hangingwall associated ores. Each point is the weighted average of two pieces of drill core, using techniques described in the text. Cu/Zn = blue line (A); S/100 = red line (B).

AR-0130 contains four ore Zones: 5, 3, 2, and 1 (Figures 1.7, 2.6, 2.12). GS is present above and below all the zones (Figure 2.6). Figure 2.13 shows vertical Cu/Zn ratios for all ore horizons as the solid blue line. Each point represents the weighted average of two to three adjacent pieces of core; the total interval length for each point is ~15-20 cm. The uppermost Zones 5 and 3 display simple, vertically symmetric variations in Cu/Zn ratio (Figure 2.13). These Cu/Zn ratios suggest that each horizon constitutes a single isoclinal recumbent anticline with footwall associated ore in the center.

Multiple analyses conducted for Zones 1 and 2 of AR-0130 show excellent reproducibility of Cu/Zn ratios (Figure 2.14). Although variations in Cu/Zn ratios are not very great for these two zones, the reproducibility by multiple analyses indicates that the variations are real. The symmetrical zoning in both also suggests isoclinal recumbent folding, with the Zn-rich massive sulfide concentrated in the center of both ore horizons.

These ratios display the patterns also observed in drill holes AR-0128 and AR-0131, with two isoclinal overturned fold repeats (Figures 2.6, 2.11, 2.14).

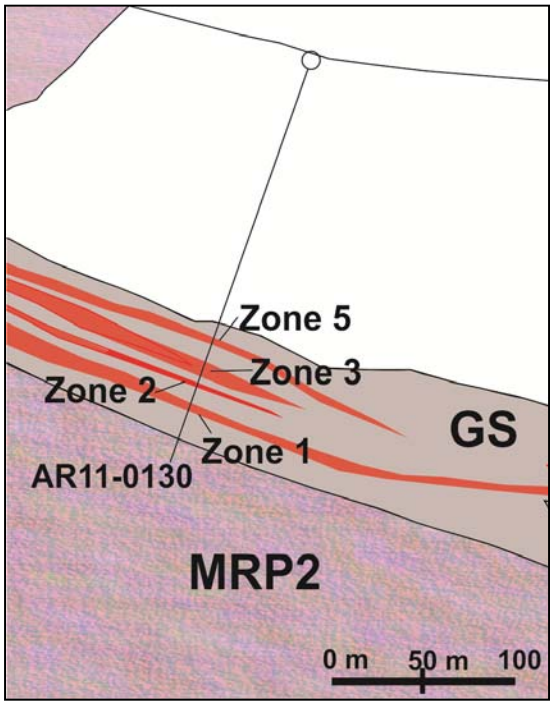

Figure 2.12: Cross-section through drill hole AR-0130. Four ore zones (5, 3, 2, and 1) are shown in red. GS is present both above and below the ore zones. See Figure 1.7 for location. White space represents other lithologies.

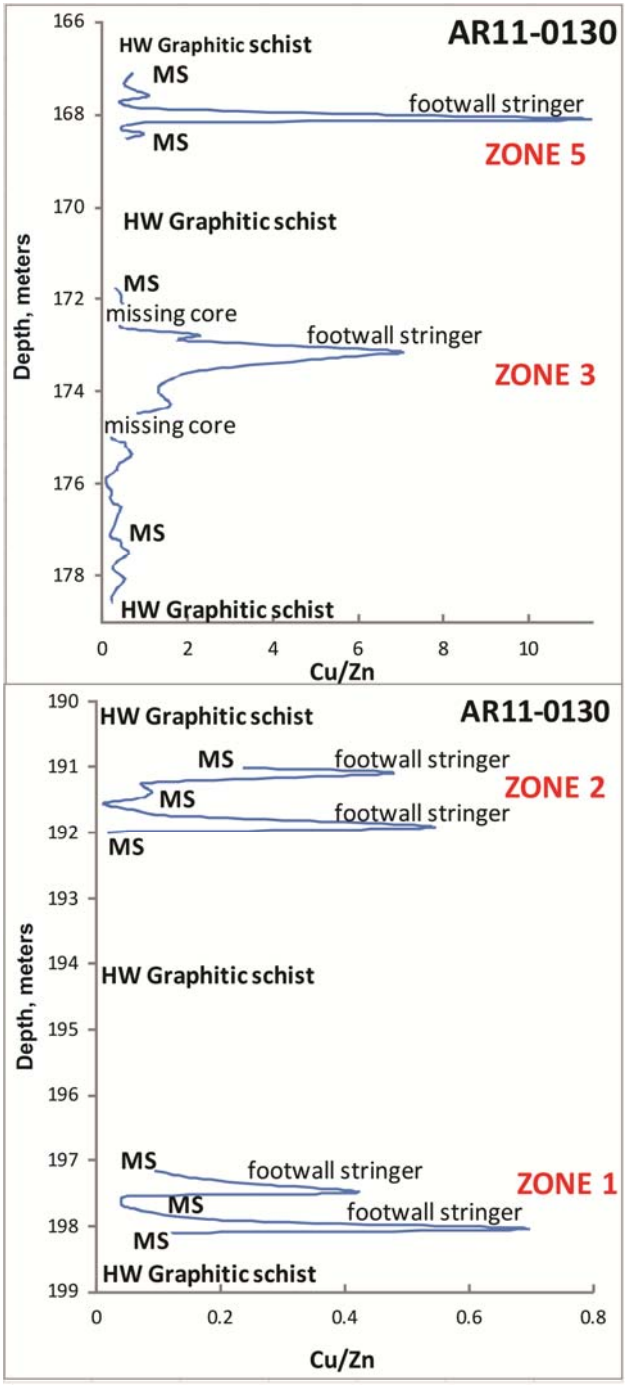

Figure 2.13: Vertical variation in Cu/Zn ratios for drill hole AR-0130. This graph shows symmetrical zoning from Zn-rich massive sulfide to Cu-rich footwall stringer-style mineralization within each ore horizon.

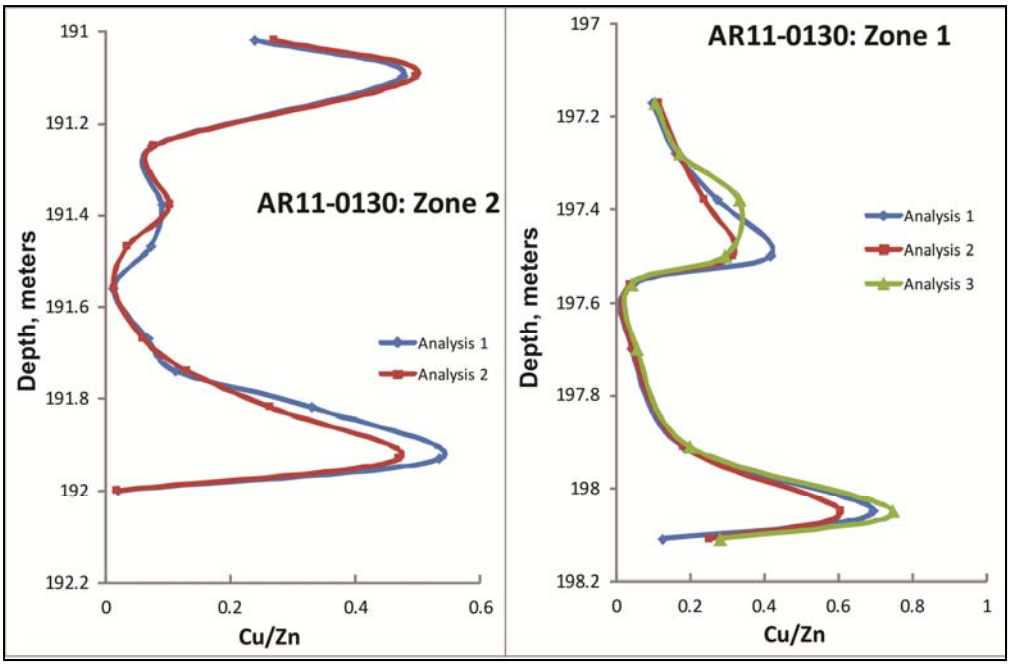

Figure 2.14: Close-up of vertical variations in Cu/Zn ratios for Zones 2 and 1 in AR-0130. These graphs show results of repeated analyses and excellent reproducibility. The symmetric changes in Cu/Zn ratios imply folding of a zoned massive sulfide sheet.

AR-0129 contains six ore zones: Zone 5, Zone 4, Zone 3, Zone 2, Zone 1 and the informally herein named Zone 2.5 (Figures 1.7 and 2.15). GS and footwall rocks (non-graphitic) are complexly interspersed with sulfide zones (Figures 2.6, 2.15, 2.16). Starting at the top, Zone 5 shows asymmetric metal zoning from GS to massive sulfide (Zn-rich) to footwall stringer-style (Cu-rich) into footwall rocks (Figure 2.16, top). Zones 4 and 3 show vertically symmetric variations in Cu/Zn ratios and are bounded above and below by footwall rocks (Figures 2.6, 2.15, 2.16). These variations suggest each represents a single over-turned recumbent syncline, with younger massive sulfide in the center flanked by older stringer zone sulfide.

A small (approximately 2.5 m thick) irregular ore horizon designated Zone 2.5 (Figures 2.15, 2.16) shows asymmetric variations in Cu/Zn ratios and bounding rocks that indicate it represents a single upside-down ore horizon. Zone 1 is similar to Zone 2.5 in that the asymmetric metal zoning and bounding rocks indicate it is a single upside-down horizon. Zone 2 is more complicated, although it displays overall asymmetric upright

zoning from a Cu-rich stringer zone base to a Cu-poor massive sulfide zone under GS. Zone 2 also contains a Cu-rich stringer zone, which might be infolded.

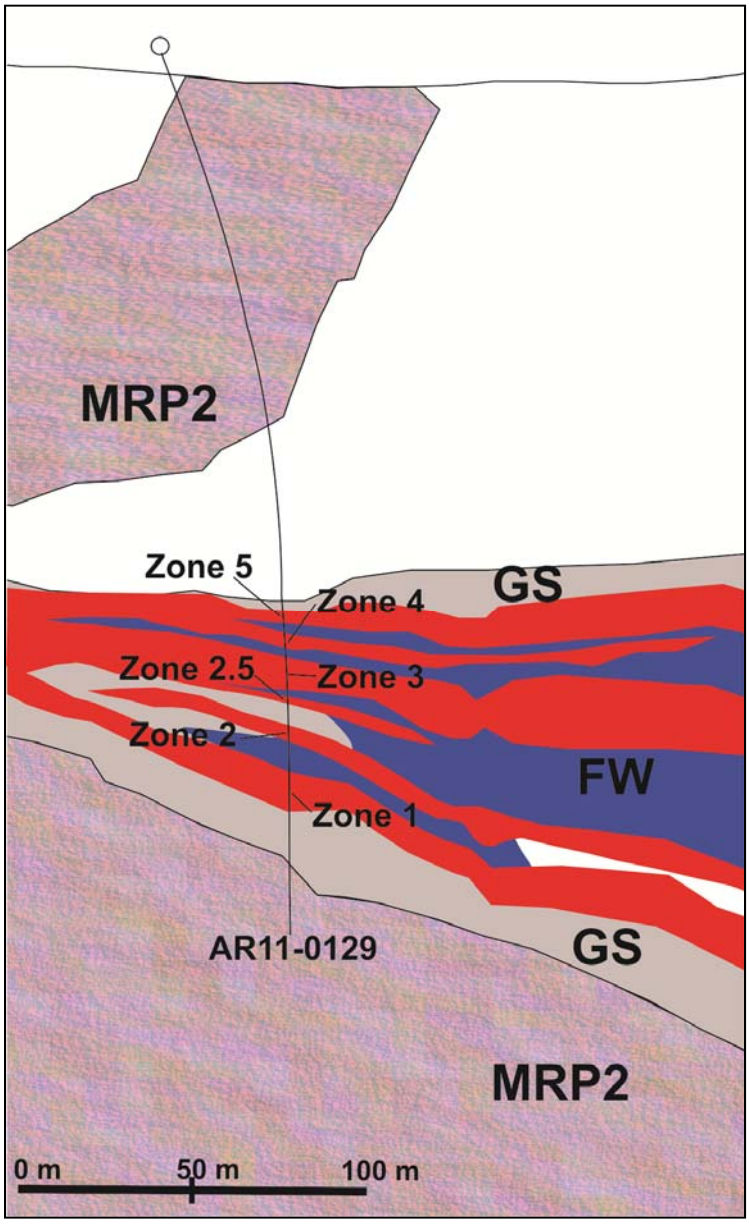

Figure 2.15: Cross-section through drill hole AR-0129. Six ore zones (5, 4, 3, 2.5, 2, and 1) are shown in red. GS and footwall rocks (FW) are complexly interfingered between ore zones, but GS lies above and below the ore package. See Figure 1.7 for location. White space represents other lithologies.

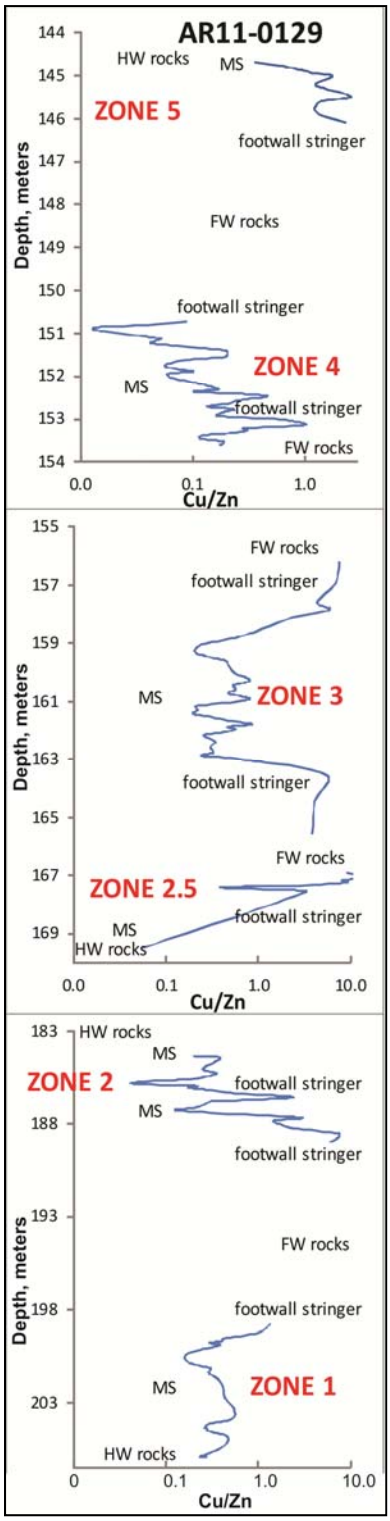

Figure 2.16: Vertical variation in Cu/Zn ratios for drill hole AR11-0129. This graph shows asymmetric zoning in Zones 5, 2.5, 2, and 1 with symmetrical zoning of Zn-rich massive sulfide surrounded by Cu-rich footwall stringer-style mineralization in Zones 4 and 3.

2.4 Discussion

Metal ratios examined at this detailed (tens of centimeters) scale reveal complex patterns not previously recognized in meter-scale assays of individual ore horizons. The repeated symmetries (and asymmetries) in vertical metal zoning suggest that complex folding, and not multiple original ore horizons, are responsible for the current juxtaposition of the ore horizons. Although individual holes can be described by such geometries, the challenge is to create a plausible geometry consistent with multiple drill holes. Such is attempted for section B-B' (Figure 2.17), perpendicular to the Arctic overturned anticline (see Figure 1.6 for location of the section).

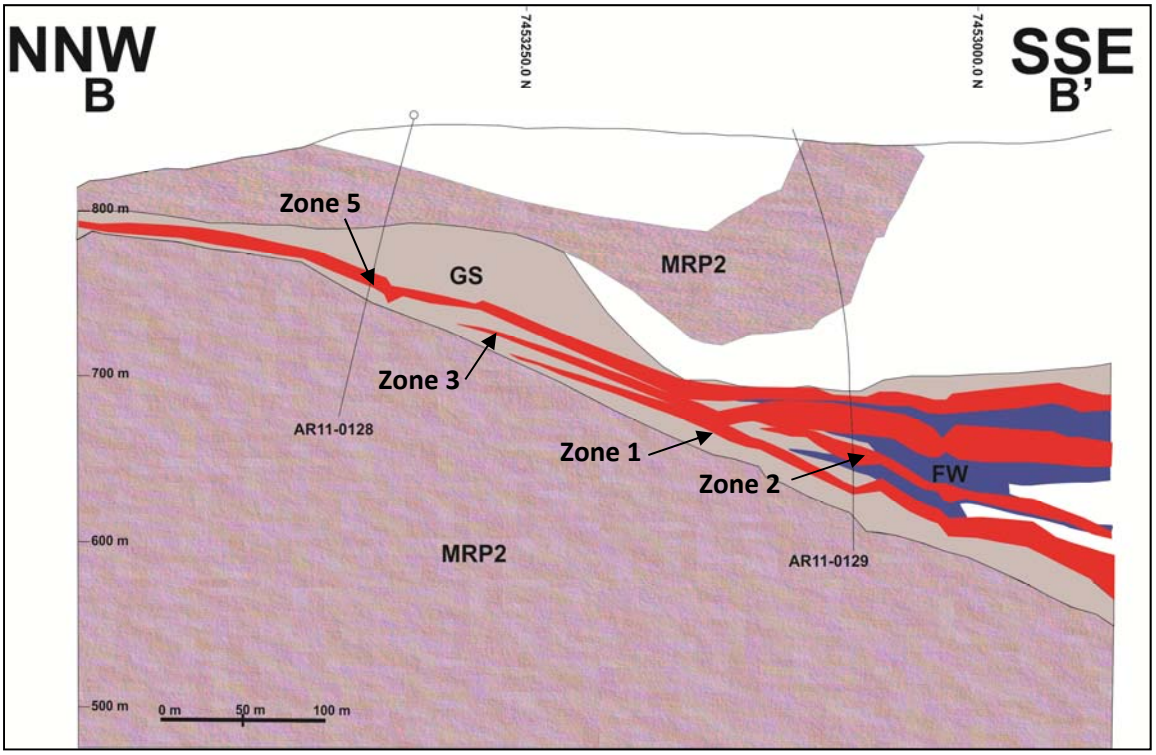

Figure 2.17: Generalized NNW-SSE cross-section B-B', perpendicular to the Arctic fold axis, modified to show only drill holes AR-0128 and AR-0129. Red = ore zones, GS = gray schist; MRP = metarhyolite porphyry; FW = footwall rocks. Cross-section location shown on Figure 1.6. White space represents other lithologies.

Drill holes AR-0128 and AR-0129, located on section B-B' (Figure 2.17), show a series of ore zones based on economic mining widths. The connections between drill

holes AR-0128 and AR-0129 are hypothetical as there is little drill data between the two. Thus the single 'Zone 5' of drill hole AR-0128 might correlate with any or all of the horizons in drill hole AR-0129. Similarly, the ore horizons shown in drill hole AR-0129 are simplified from a more detailed cross-section which shows six different horizons (Figure 2.15). Regardless, AR-0128 contains one ore horizon, which if folded by the simplest model, would resemble the pattern shown in Figure 2.18A. The actual pattern (Figure 2.9) shows three high Zn/Cu, high sulfide massive sulfide zones. Each zone is flanked by a high Cu/Zn, low sulfide stringer zone as shown in Figure 2.18B.

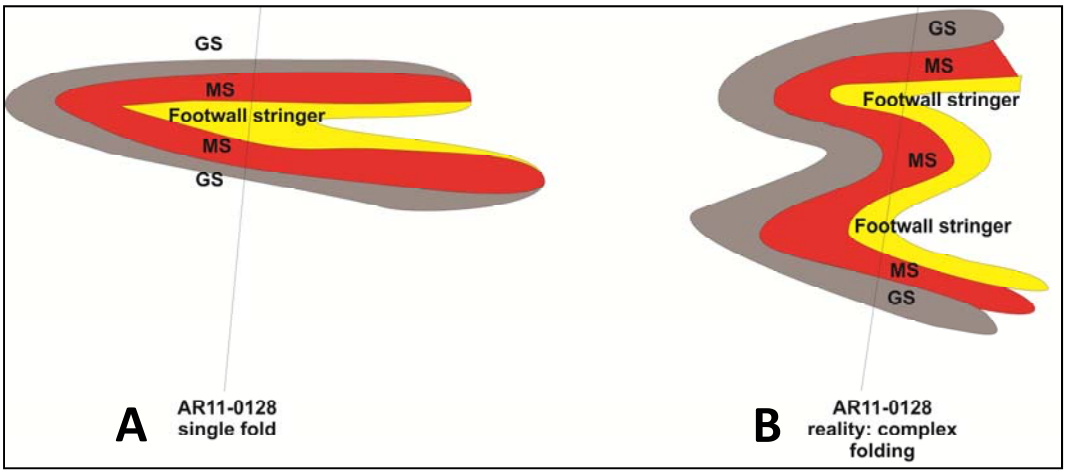

Figure 2.18: Expected simple geometry (A) and actual apparent geometry (B) of ore for drill hole AR-0128. GS = gray schist (hanging wall rock); MS = massive sulfide (Zn-rich horizons); footwall stringer = high Cu/Zn, low-total sulfide rock.

In contrast, at first glance drill hole AR-0129 intersects 4 different, unrelated ore horizons (Figure 2.17). In detail, however, the complex interfingering of footwall and hangingwall rocks (Figure 2.6B) and the complex asymmetric and symmetric metal zoning (Figure 2.16) are more readily explained by a series of tight isoclinal folds with an overall antiformal aspect (Figure 2.19). That is, the uppermost unit above the ore package and the lowermost unit below the ore package is the hangingwall GS unit. The ore package itself contains layers with footwall rock types as well as Cu-rich, stringer ore. The informally named Zone 2.5 is not recognized as a modeled ore zone, perhaps due to its irregular occurrence in other drill holes. An individual ore zone can consist of

one or more original ore layers as defined by asymmetric metal zoning from footwall to hangingwall ore.

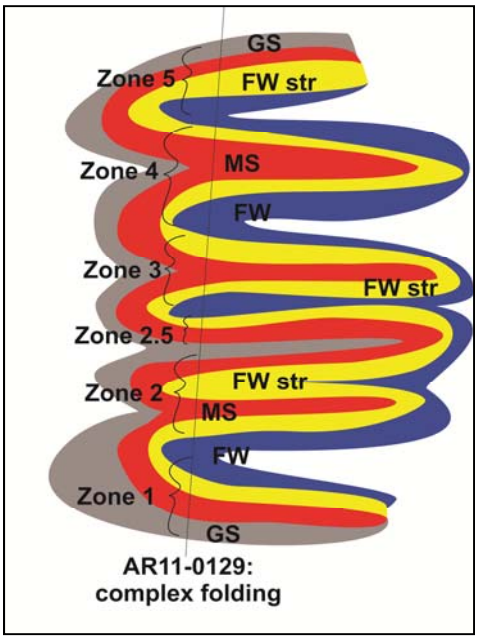

Figure 2.19: Interpretive geometry of drill hole AR-0129 created by multiple tight isoclinal folds. This is consistent with the observed variations in rocks and metal zoning. GS = gray schist (hanging wall rock); MS = massive sulfide (Zn-rich horizons); FW str= Footwall stringer zone (high Cu/Zn); FW=footwall rocks.

Figure 2.20 shows a plausible geometry for connecting drill holes AR-0128 and AR-0129 in terms of complex overturned, recumbent folds. AR-0128 exhibits symmetry consistent with the closure of a tight, complex anticline. AR-0129 contains symmetric and asymmetric metal zoning, consistent with multiple repeats of several fold limbs. Zones 5 and 1 in this drill hole appear to be the same limb with several folded repeats. In this model, Zone 5 in drill hole AR-0128 is the continuation of Zones 5, 4, and 3 in drill hole AR-0129 (Figure 2.20). Although two drill holes exist between holes AR-0128 and AR-0129 (Figure 1.7), without additional information it is not possible to say how they fit into this folding scheme.

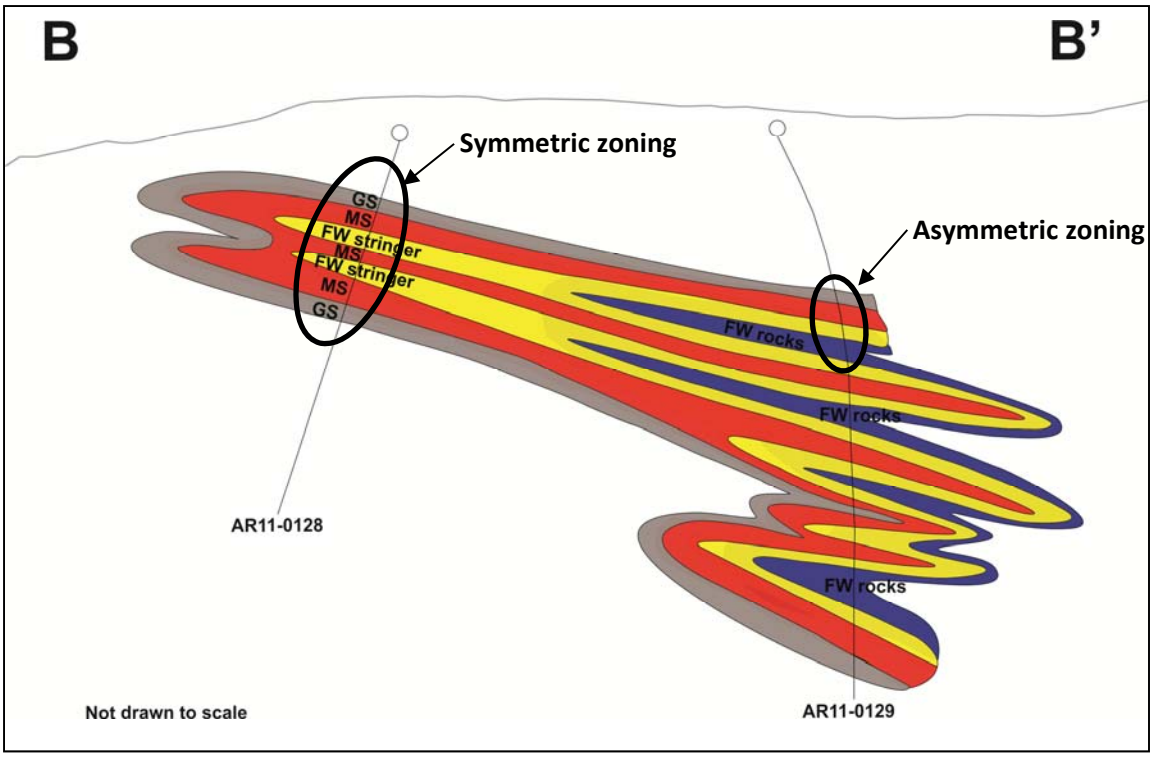

Figure 2.20: Schematic section B-B' showing the ore horizons of drill holes AR-0128 and AR-0129 connected by tight isoclinal folds. GS = gray schist; MS = massive sulfide (Zn-rich horizons); FW stringer = high Cu/Zn horizons; FW = footwall rocks. Figure is not drawn to scale so as to make folded horizons more apparent.

A similar exercise cannot be performed for AR-0130 and AR-0131, as these drill holes are spaced too far apart for correlations. However, possible folding geometries can be shown. Ore Zone 1 in hole AR-0131 shows a sequence similar to that in hole AR-0128, with a complex overturned, recumbent anticline (Figure 2.21B). Drill hole AR-0130 displays a more complex pattern, similar to that of drill hole AR-0129, but lacking the interfolded footwall rocks. An overturned recumbent anticline would be consistent with the pattern of ore zones identified in hole AR-0130 (Figure 2.21A). Zones 5 and 3 show simple symmetric metal zoning indicating these zones represent a single isoclinal fold. Zones 2 and 1 show multiple repeats similar to those of drill holes AR-0128 and AR-0131 (Figure 2.21A).

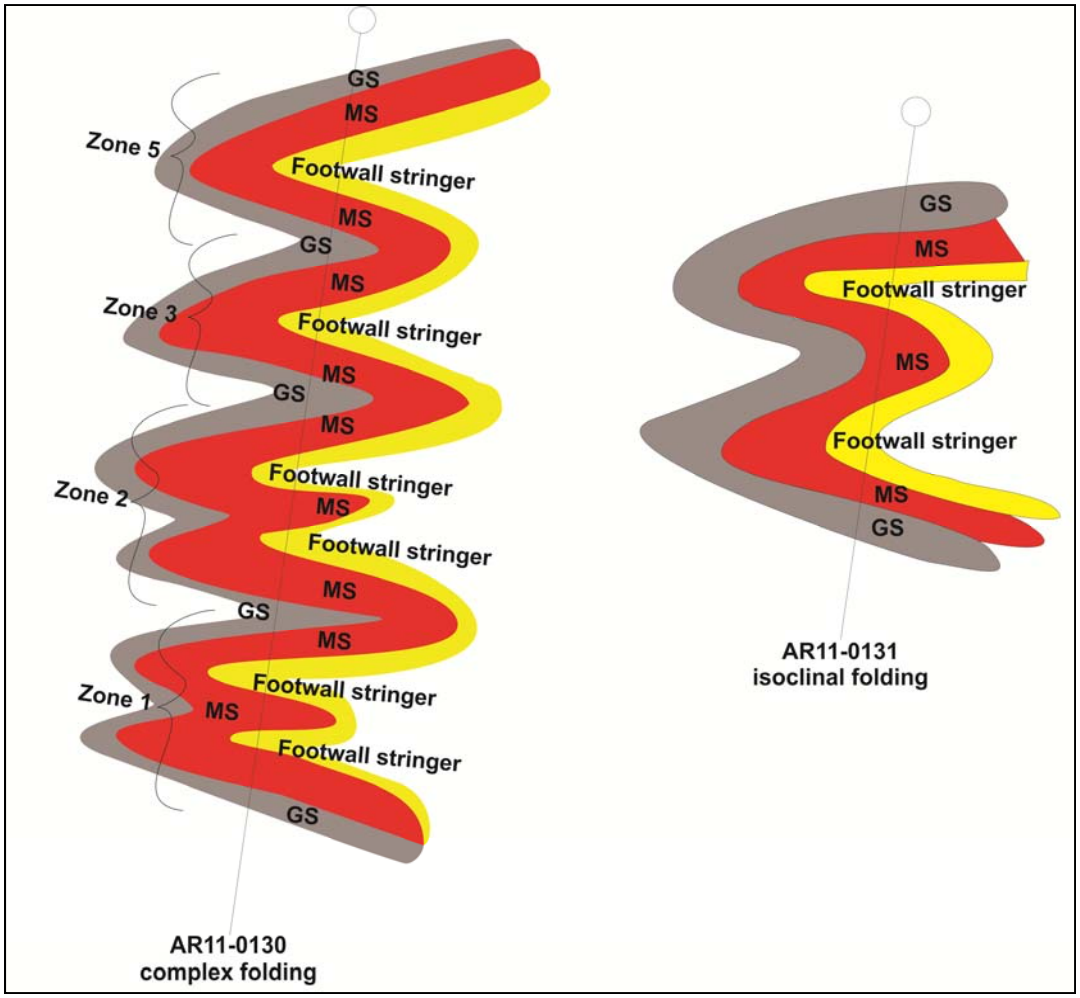

Figure 2.21: Interpretive fold geometries that account for the metal zoning patterns present in drill holes AR-0130 (A) and AR-0131 (B). GS = gray schist; MS = massive sulfide (Zn-rich horizons); Footwall stringer = high Cu/Zn ore. Figure not drawn to scale.

2.5 Conclusion

I have attempted to determine detailed scale metal zoning of complex sulfides by using a small-diameter, hand-held XRF. Although I have no way to check the results for accuracy, the precision indicated by replicate analyses indicates this should be a valid means for assessing compositional variation. Further, metal ratio data coupled with magnetic susceptibility (ms) data (to distinguish hangingwall and footwall rocks) show consistent patterns: high Cu/Zn footwall ores are consistently associated with low-ms footwall rocks and low Cu/Zn ores are association with high-ms hangingwall rocks.

At the Arctic Deposit, where multiple massive to semi-massive sulfide horizons have been identified by drilling, detailed metal zoning can be used to interpret relative juxtaposition and geometry of the different ore horizons. Asymmetric metal zoning appears to represent a single fold limb (e.g., Figure 2.20) whereas symmetric metal zoning indicates a fold nose (e.g., Figure 2.20). Regardless of the complexity, the patterns in metal zoning displayed are entirely different from that expected for a simple, multiply-layered stratigraphic succession of sulfide horizons. In the case of a simple multiply-layered succession of sulfide horizons, each one should be zoned from a Cu-rich bottom to a Zn-rich top. The data do not support this simplistic interpretation.

In summary, metal ratios combined with recognition of footwall and hangingwall rock types confirm that Arctic can be described as an isoclinal recumbent anticline. However, it appears that folding of the ore horizons is considerably more complicated than two sub-horizontal limbs. Instead, even the single horizon present at the NW edge of the deposit, closest to the fold hinge, represents a complex fold. Limbs far from the fold axis in the SE part of the deposit reflect extremely complex folding around the original core of the deposit.

Chapter 3 Sphalerite and Metamorphic Reactions

3.1 Metamorphism and the Importance of Sphalerite

Iron content of sphalerite is a function of metamorphic P-T-X conditions and can give important information about metamorphism. The iron content of sphalerite [(Zn,Fe)S] is expressed as mol% FeS and is a function of fS_2—effectively partial pressure of S_2 gas. The Fe-content of sphalerite rises with decreasing fS_2 as iron is partitioned from neighboring pyrite—a high-S mineral—into sphalerite (Vaughn and Craig, 1997). This reaction can be expressed as:

$$(1\text{-}n)\ ZnS + nFeS_2 = (Zn,Fe)S + n/2\ S_2.$$

Consequently, higher fS_2 drives the system to making low-Fe sphalerite + pyrite; while lower fS_2 drives the reaction to a higher-Fe sphalerite. In all cases the total iron content is fixed, the variable is simply how much of the iron is present as pyrite instead of higher-Fe sphalerite. The mol% FeS in sphalerite when present with pyrite + pyrrhotite (a buffered fS_2 assemblage; Hall, 1986) at low pressure is approximately 21% (Vaughn and Craig, 1997; Figure 3.1) and is generally independent of temperature. For other buffered assemblages (e.g., bornite + chalcopyrite + pyrite), the %FeS varies little with temperature (Vaughn and Craig, 1997; Figure 3.1).

Sphalerite in Kuroko deposits (Ono and Sato, 1995; Kitazono and Ueno, 2003) typically contains <0.1-1.9 mol% FeS (Figure 3.1). Kuroko sphalerite is commonly present with the assemblage bornite + pyrite; neither arsenopyrite nor pyrrhotite is present (Ono and Sato, 1995; Kitazono and Ueno, 2003; Glasby et al., 2008). In contrast, Schmandt (2009) reported data for twenty Arctic sphalerite samples from which I calculated 1.6-12.3 mole % FeS (Figure 3.1). Lower-Fe sphalerite is progressively paler (approaching white), whereas high-Fe sphalerite is red to brown; such is the range of sphalerite colors observed at Arctic (Schmidt, 1983; Schmandt, 2009). Schmidt (1983) reports assemblages including (1) bornite + pyrite, (2) arsenopyrite + pyrite, and (3)

pyrrhotite + pyrite at Arctic, but does not record the associated sphalerite composition. Sphalerite becomes progressively more Fe-rich (light gray lines, Figure 3.1) as it equilibrates with these different sulfide assemblages (1, 2, 3 above), respectively.

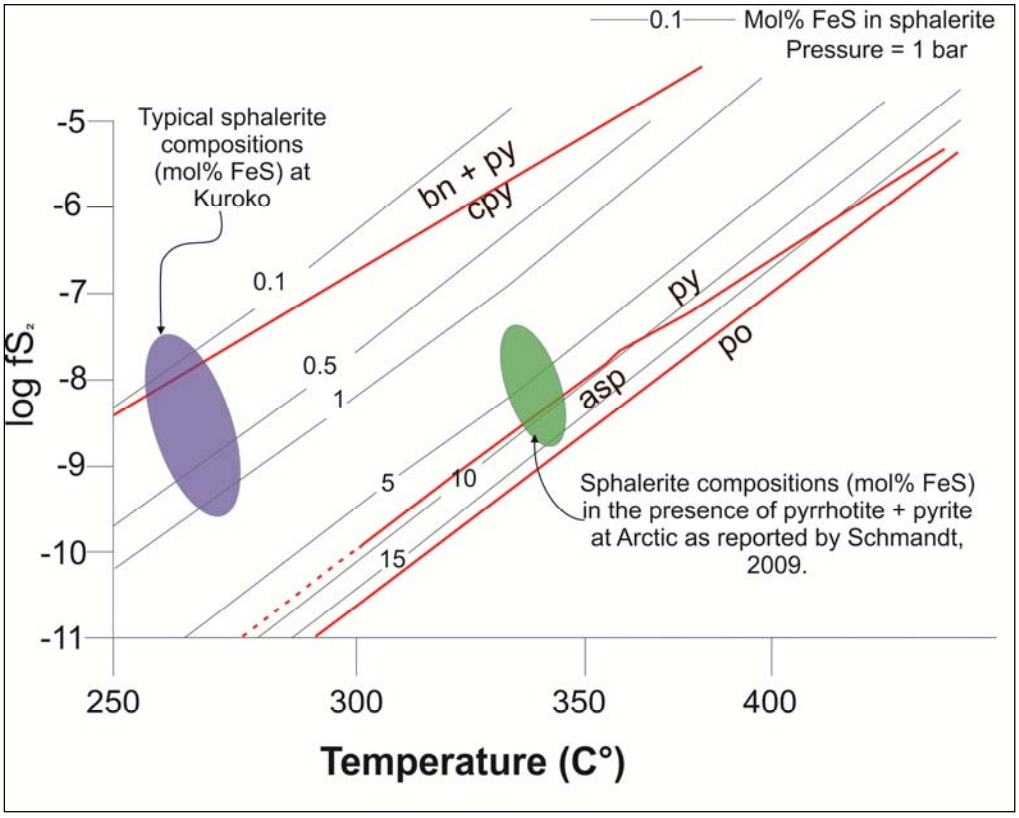

Figure 3.1: Temperature vs. log fS2 diagram. This chart displays mineral stabilities and mol% FeS content of sphalerite and their relationship at 1bar. Kuroko sphalerite contains low mol% FeS and is associated with bornite + pyrite. In contrast, Arctic sphalerite contains 1.6-12.3% mol% FeS and is associated with pyrrhotite + arsenopyrite as well as pyrite+bornite. Bn = bornite, py = pyrite, cpy = chalcopyrite, asp = arsenopyrite, and po = pyrrhotite. Kuroko data from Ono and Sato (1995); Arctic data calculated from Schmandt (2009). Diagram modified with data from Vaughn and Craig, 1997.

Previous workers agree that the Ambler mining district underwent blueschist metamorphic conditions, which is based on the presence of rare blue amphiboles, and later re-equilibrated under greenschist facies conditions (Hitzman 1980; 1982; Dusel-Bacon et al., 1989). However, the local presence of garnet in greenstone at Arctic implies a minimum temperature of approximately 400Cº (Gilbert et al., 1977). Using phengite-feldspar thermobarometry, Patrick (1995) indicated metamorphic conditions of approximately 375$\pm$25 C° and 10 $\pm$ 2 kbar.

Since a fundamental postulate among metamorphic petrologists is that equilibrium among the various spatially associated minerals occurs during metamorphism, sphalerite compositions should reflect the surrounding sulfide mineralogy as influenced by sulfur fugacity and temperature (e.g., light gray lines, Figure 3.1). Variations in fS_2 at constant fluid sulfur content in turn reflects a different oxidation state (fO_2): lower fO_2 generates lower fS_2 (Barnes, 1979). The relevant equilibrium is:

$$H_2S + ½\ O_2 = H_2O + ½\ S_2.$$

At constant temperature there is an equilibrium constant K, such that $\log fS_2 = \log K + \log fO_2 + \log[H_2S]$, where the last term is the activity of dissolved reduced sulfur in solution (Barnes, 1979). At constant temperature and fluid composition, $\log fS_2$ is simply proportional to $\log fO_2$. Thus, although Figure 3.1 shows sphalerite compositions as functions of fS_2, variations in fS_2 really reflect variations in fO_2 (oxidation state).

One final complication is that the iron content of sphalerite in equilibrium with pyrite + pyrrhotite is not only a function of fS_2 and temperature, but also drops with increasing pressure (Figure 3.2), a relationship detailed by Vaughn and Craig (1997). The relationships depicted by Figure 3.1 are for atmospheric pressure. Thus, it will be necessary to adjust fS_2 –sphalerite compositional contours for the appropriate pressure of metamorphism at Arctic.

In this chapter, I examine sphalerite compositions throughout the Arctic deposit and compare them to the associated sulfides at a detailed scale to better understand the fS_2-fO_2 conditions present—and their spatial distribution—during metamorphic re-equilibration. I also examine the spatial pattern of sphalerite compositions at Arctic and compare sphalerite compositions to those of associated silicate minerals. Finally, I attempt to relate variations in iron content of sphalerite through the deposit to geologic conditions likely to affect fO_2-fS_2.

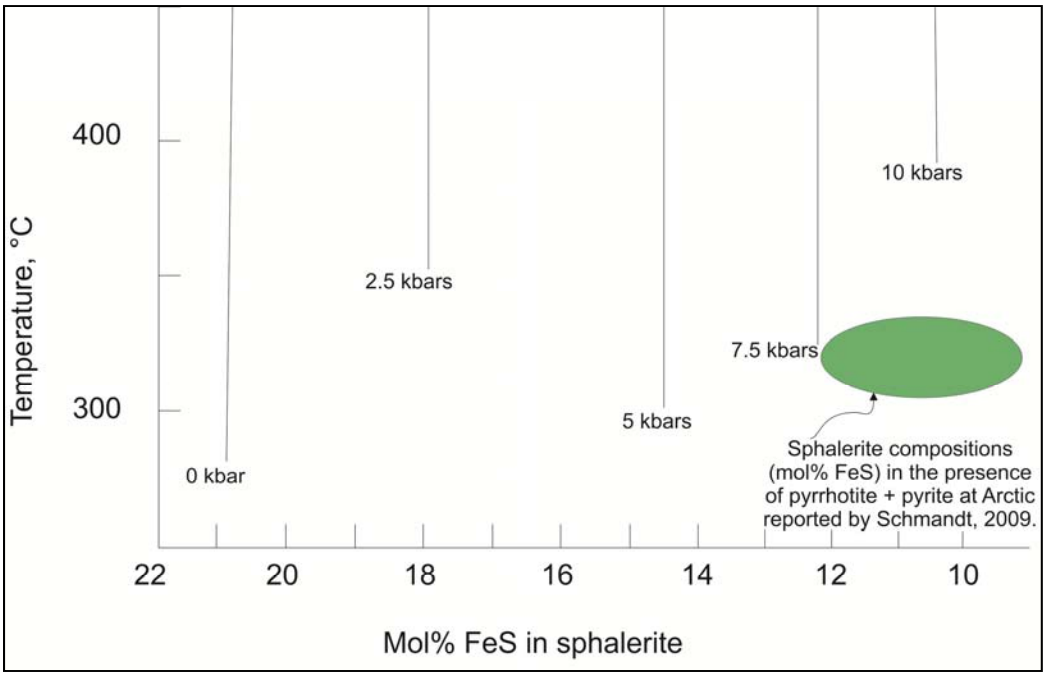

Figure 3.2: Temperature vs. mol% FeS diagram. Mol% FeS content of sphalerite is shown in conjunction with different pressures (kbars). Figure modified with data from Vaughn and Craig, 1997.

3.2 Sphalerite Composition at the Arctic Deposit

At Arctic, in the rare cases of sphalerite inclusions preserved in pyrite porphyroblasts (e.g., Figure 3.3), iron contents of sphalerite increase outward (with time) indicating changing conditions (or possibly degree of equilibration) during metamorphism. This evidence is consistent with original low-FeS sphalerite that changed during metamorphism.

In this study I determined sphalerite compositions for 156 samples by analyzing at least three spots in at least three different grains in a single sample, for a total of approximately 1,400 analyses. Sphalerite analyses were performed over a period of more than a year. Re-analyses of sphalerite analyzed yielded consistent compositions. I found %FeS contents that ranged from 0.6 to 12.8% (Table 3.1). The standard deviations for the minimum 9 analyses were less than one tenth of the absolute values.

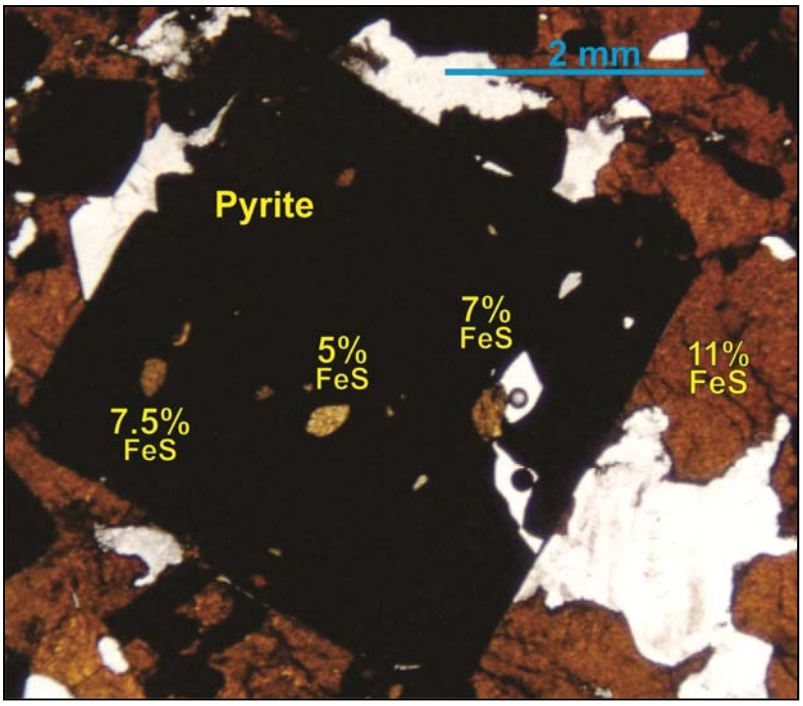

Figure 3.3: Sphalerite in and surrounding a pyrite porphyroblast from AR78A. FeS-content of sphalerite rises with decreasing fS2 as iron is partitioned from pyrite into sphalerite (Vaughn and Craig, 1997). The lighter sphalerite encased in the pyrite grain has less iron, expressed as mol% FeS than the surrounding sphalerite which is of uniform composition.

Table 3.1: Mol% FeS in Sphalerite by Electron Microprobe

Sample	Drill Hole	Depth_m	Avg mol%FeS	St Dev	Associated Mineralogy
197-1	128	90.69	7.2	0.3	py
197-2	128	90.86	5.4	0.3	py
197-3	128	90.98	4.8	0.1	py
197-4	128	91.28	4.2	0.1	po, py
197-5	128	91.35	3.7	0.1	py
197-6	128	91.47	3.8	0.3	py
197-7	128	91.62	3.3	0.1	py
197-8	128	92.01	2.0	0.2	asp, py
197-9	128	92.06	1.5	0.2	asp, py
198-1	128	92.15	1.5	0.1	py
198-2	128	92.59	1.6	0.2	py
198-3	128	92.72	1.4	0.2	py
198-4	128	93.02	2.4	0.2	asp, py
198-5	128	93.04	2.3	0.2	py
198-6	128	93.12	2.7	0.2	py
198-7	128	93.27	2.6	0.1	py

TABLE 3.1 CONT.: Mol% FeS in Sphalerite by Electron Microprobe

Sample	Drill Hole	Depth_m	Avg mol%FeS	St Dev	Associated Mineralogy
198-8	128	93.39	2.5	0.2	py
198-9	128	93.53	3.8	0.3	py
199-1	128	93.62	6.7	0.4	py
153-1	129	103.85	12.7	0.04	asp, py
155-6	129	151.31	3.9	0.4	py
157-1	129	152.42	3.7	0.4	py
157-2	129	152.53	4.4	0.1	py
157-3	129	152.57	4.7	0.1	py
158-1	129	152.91	4.5	0.03	py
158-2	129	152.94	4.8	0.1	py
158-3	129	153.04	4.2**	0.2	py
160-1	129	157.97	8.5**	0.4	py
161-1	129	158.43	11.0**	0.3	po, py
162-1	129	159.46	5.1	0.2	py
163-1	129	159.73	1.5	0.2	asp, py
163-2	129	159.75	2.1	0.2	py
164-1	129	159.78	2.2	0.1	py
164-2	129	159.89	2.2	0.4	asp, py
164-3	129	159.91	2.2	0.2	py
165-1	129	160.41	3.3	0.2	py
165-2	129	160.43	3.0	0.1	asp, py
166-1	129	160.58	3.7	0.2	py
166-2	129	160.61	3.7	0.3	py
167-1	129	161.66	3.9	0.1	py
167-2	129	161.75	4.3	0.2	asp, py
168-1	129	163.03	2.3	0.4	po, py
171-1	129	166.95	7.1	0.7	asp, py
172-1	129	185.63	6.7	1.6	asp, py
172-2	129	185.64	7.1	0.2	asp, py
173-1	129	185.96	5.6	0.1	asp, py
173-2	129	186.01	5.5	0.1	py
173-3	129	186.21	5.6	0.3	py
173-4	129	186.29	5.3	0.2	py
175-1	129	186.82	5.6	0.4	asp, py
175-2	129	186.83	6.4	0.4	asp, py
175-3	129	186.90	6.0	0.2	py
175-4	129	186.96	5.8	0.2	py

TABLE 3.1 CONT.: Mol% FeS in Sphalerite by Electron Microprobe

Sample	Drill Hole	Depth_m	Avg mol%FeS	St Dev	Associated Mineralogy
176-1	129	199.39	7.1	0.1	asp, py
177-1	129	199.52	6.7	0.2	py
178-2	129	200.13	4.0	0.2	py
180-1	129	201.20	2.3	0.1	asp, py
180-2	129	201.22	2.2	0.6	asp, py
180-3	129	201.32	2.9	0.3	asp, py
180-5	129	201.50	3.4	0.3	asp, py
182-1	129	202.88	2.3	0.3	asp, py
182-2	129	202.91	3.2	0.1	asp, py
182-3	129	202.99	4.2	0.8	asp, py
183-1	129	203.20	4.9	0.1	asp, py
183-2	129	203.45	2.3	0.1	py
184-1	129	204.25	3.9	0.8	asp, py
184-2	129	204.26	3.7	0.4	py
185-1	129	205.47	5.1	0.1	py
185-2	129	205.52	4.3	0.1	asp, py
186-1	129	205.77	7.5	0.6	asp, py
186-2	129	205.85	8.2	0.1	py
186-3	129	205.89	6.7	0.4	py
188-1	129	207.63	12.5	0.3	po, py
188-2	129	207.68	12.5	0.2	po, py
190-1	130	167.35	4.5*		py
190-3	130	168.03	3.7	0.5	asp, py
190-4	130	168.21	3.2	0.1	py
190-5	130	168.44	4.5	0.2	py
191-1	130	171.75	9.6	1.2	po, py
191-2	130	171.95	2.4	0.3	asp, py
191-3	130	172.04	5.1	0.2	asp, py
191-4	130	172.21	5.6	0.1	py
191-5	130	172.66	3.8	0.1	py
191-6	130	172.90	3.2	0.2	py
191-7	130	172.98	2.4	0.3	asp, py
192-2	130	173.44	2.3	0.2	asp, py
192-3	130	173.52	2.3	0.3	asp, py
192-5	130	174.03	2.7	0.2	asp, py
192-6	130	174.30	3.2	0.1	py
192-7	130	175.22	11.4	0.1	po, asp, py

TABLE 3.1 CONT.: Mol% FeS in Sphalerite by Electron Microprobe

Sample	Drill Hole	Depth_m	Avg mol%FeS	St Dev	Associated Mineralogy
192-8	130	175.29	11.2	0.4	po, py
192-9	130	175.35	11.4	0.1	po, py
193-1	130	175.89	9.2	0.1	asp, py
193-2	130	176.00	9.1	0.1	py
193-3	130	176.85	5.6	0.1	asp, py
193-4	130	176.96	6.0	0.1	asp, py
193-5	130	177.50	2.7	0.1	asp, py
193-6	130	177.57	3.0	0.0	py
193-7	130	177.64	3.4	0.1	po, py
193-8	130	177.70	3.0	0.1	py
193-9	130	177.98	3.4	0.1	asp, py
194-1 Tet	130	178.26	2.7	0.2	asp, py
194-1 Ten	130	178.26	NA	NA	asp, py
194-2	130	178.29	2.6	0.1	asp, py
194-3	130	178.51	2.4	0.2	asp, py
194-4	130	178.96	3.2	0.3	asp, py
194-5	130	179.14	6.5	0.2	py
194-6	130	179.28	6.3	0.2	asp, py
194-7	130	179.88	9.4	0.1	py
195-1	130	191.66	2.8	0.1	asp, py
195-2	130	191.76	8.1	0.8	py
195-3	130	191.96	7.2	0.2	asp, py
196-1	130	197.22	2.9	0.2	py
196-2	130	197.48	1.1	0.1	asp, py
196-3	130	197.53	2.2	0.1	asp, py
196-4	130	197.87	2.2	0.2	asp, py
196-5	130	198.11	2.5	0.1	asp, py
196-6	130	198.24	1.4	0.1	asp, py
200-1	131	125.40	11.5	1.7	po, po
200-2	131	127.24	11.8	0.4	po, asp, py
200-3	131	127.42	11.1	1.7	po, asp, py
200-4	131	127.59	10.0	0.1	asp, py
200-5	131	127.70	11.9	1.1	po, asp, py
200-6	131	166.89	12.3	0.3	po, py
200-7	131	166.96	12.9	0.3	po, asp, py
200-8	131	167.14	12.2	0.2	po, asp, py
200-9	131	167.45	11.4	0.4	po, asp, py

TABLE 3.1 CONT.: Mol% FeS in Sphalerite by Electron Microprobe

Sample	Drill Hole	Depth_m	Avg mol%FeS	St Dev	Associated Mineralogy
201-1	131	167.53	11.6	0.5	po, py
201-2	131	167.58	11.8	0.6	po, asp, py
201-3	131	167.73	12.7	0.2	asp, py
201-4	131	167.85	12.2	0.2	po, asp, py
201-5	131	168.00	11.7	0.4	po, asp, py
201-6	131	168.40	12.4	0.3	po, asp, py
BB-101	117	211.60	2.3**	0.2	py
BB-102	124	219.80	7.9**	0.4	asp, py
BB-107	118	158.16	1.6**	0.2	asp, py
BB-104	123	137.97	0.6**	0.0	bn, py
BB-106	126	208.80	12.5**	1.0	po, asp, py
BB-105	116	223.61	2.6**		py
BB-103	122	177.70	7.6**	0.0	asp, py
BB-108	117w	143.10	1.1**	0.1	bn, py
AR48B-Tet	AR48	38.40	4.4	0.90	py
AR48B-Ten	AR48	38.40	4.4	0.90	py
AR79	AR79	174.20	4.5	0.3	py
AR54	AR54	25.10	4.4	0.4	py
AR66	AR66	30.40	1.9	0.1	py
AR89	AR89	239.10	11.5	0.1	py
AR50	AR50	38.60	10.0	0.2	py
AR86	AR86	169.30	6.4	0.2	py
AR78B	AR78B	238.90	6.0	0.2	py
AR18	AR18	75.00	1.4	0.2	py
AR26A	AR26A	32.80	3.8	0.1	py
AR51	AR51	44.20	3.6	0.4	py
AR52	AR52	54.80	***12.2****		po, asp, py
AR58	AR58	154.70	12.8	0.4	po, asp, py
AR61	AR61	113.40	3.1	0.2	py
AR83	AR83	264.60	7.7*		py
AR92	AR92	143.90	***3.0****		py
AR93	AR93	144.40	3.7**	0.3	py

12.0 Underlined equals analytical data adapted from Schmandt, 2009.

* 1 analysis per sample.

** Energy-dispersive analyses are standard less analyses using EDAX Phoenix v.3.1 SEM Quant ZAF software; all others are wavelength dispersive analyses as described in Chapter 1.

Asp = arsenopyrite; bn = bornite; po = pyrrhotite; py = pyrite; NA = spl not analyzed.

Sphalerite compositions plotted with associated assemblages (Figure 3.4) show the bulk of sphalerite grains present in pyrrhotite-bearing samples have compositions of 10.5-12.8 mol%FeS. The three samples with low (<9%) FeS contents contain sphalerite encapsulated in pyrite or chalcopyrite and (or) located >0.5 cm from pyrrhotite. That is, in these samples sphalerite compositions only reflect equilibrium with pyrrhotite if they are in close spatial proximity to pyrrhotite. The average composition of Arctic sphalerite in textural equilibrium with pyrrhotite (11.9 $\pm$ 0.5 %FeS; Figure 3.4) indicates a pressure of approximately 7.5 kb (Figure 3.2).

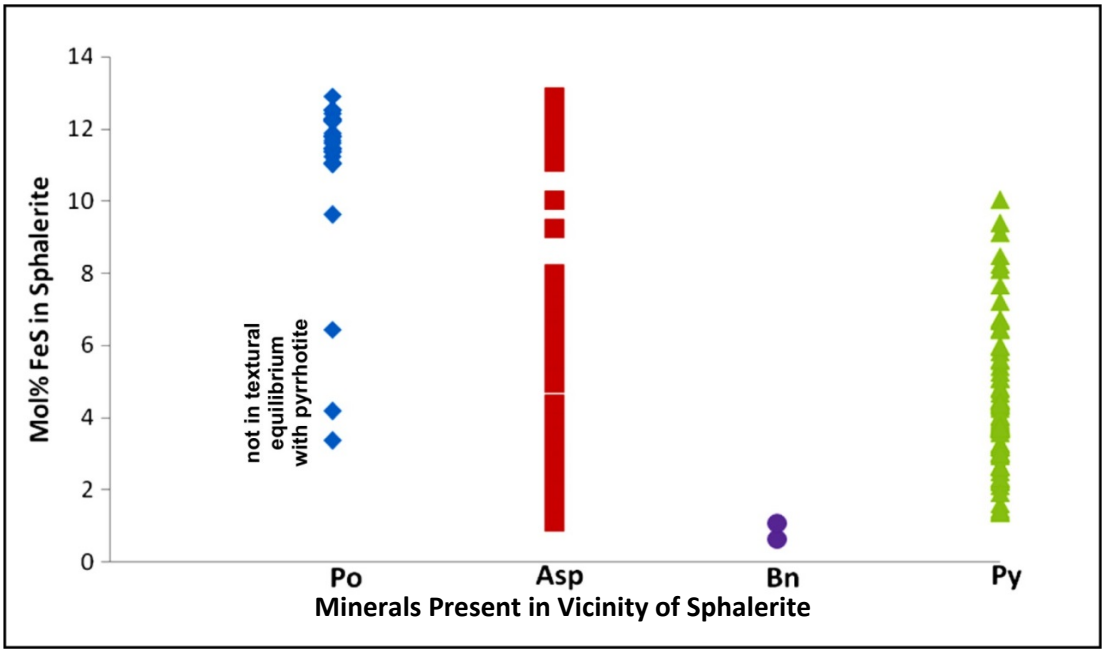

Figure 3.4: Sphalerite compositions plotted with key minerals seen within 0.5 cm of sphalerite. Pyrite is plotted where neither arsenopyrite (asp), pyrrhotite (po), nor bornite (bn) are present.

In contrast to the highest-Fe sphalerite occurring with pyrrhotite, sphalerite grains in the immediate vicinity of bornite display low mol% FeS (0.6-1.1%). This relationship is consistent with the high fS_2 required for both pyrite + bornite and low-Fe sphalerite (Figure 3.1). Similarly, sphalerite with only pyrite (no nearby arsenopyrite, pyrrhotite, or bornite; Figure 3.4) contains a wide variety of %FeS, which is consistent with the wide range of fS_2 conditions possible with pyrite (Figure 3.1). Finally, sphalerite in

arsenopyrite-bearing samples (Figure 3.4) displays variable FeS content. If in equilibrium with arsenopyrite at low pressure, they should be restricted to compositions of 7 mole % FeS or higher (Figure 3.1). Clearly, this is not the case (Figure 3.4). However, sphalerite in a given slide is not always in textural equilibrium with arsenopyrite.

Arsenopyrite at the Arctic deposit occurs in several mineralogical and textural forms and associations. The most common is disseminated, equigranular arsenopyrite occurring with pyrite ± pyrrhotite. Six samples contain an intergrown assemblage of arsenopyrite + fahlore + chalcopyrite representing a likely reaction relationship (Figure 3.5A). Three samples contain arsenopyrite with an unusual bladed habit suggesting re-crystallization during metamorphism (Figure 3.5B).

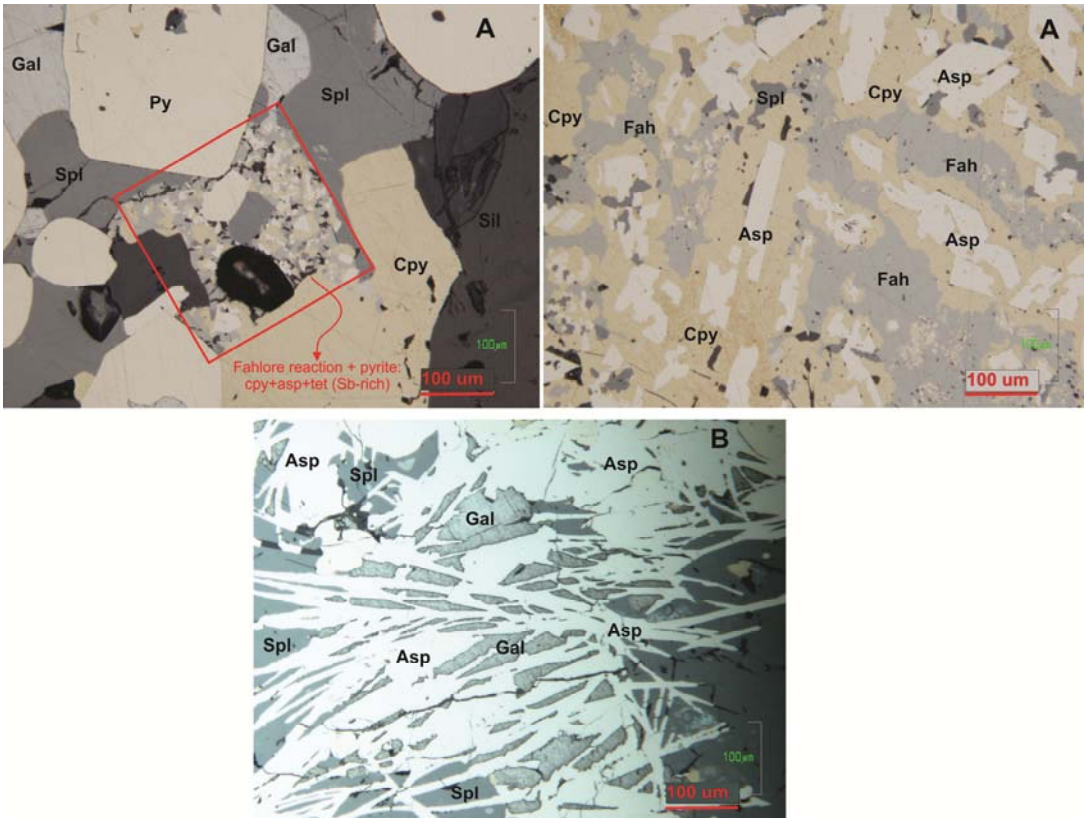

Figure 3.5: Two unusual arsenopyrite textures present at Arctic. 3.5A shows an intergrown assemblage of arsenopyrite + fahlore + chalcopyrite, representing a likely reaction relationship. 3.5B shows arsenopyrite displaying an unusual bladed habit. Gal = galena, Spl = sphalerite, Py = pyrite, Sil = silicates, Cpy = chalcopyrite, Fah = fahlore, Asp = arsenopyrite, Tet = tetrahedrite.

Compositions of sphalerite present with arsenopyrite have 3 modes at approximately 12% FeS, 7% FeS and 2% FeS (Figure 3.6). The highest iron group is present with pyrrhotite. The second highest group appears with the peculiar arsenopyrite-fahlore-chalcopyrite assemblage (Figure 3.5A), and the third group appears with bladed arsenopyrite only (Figure 3.5B).

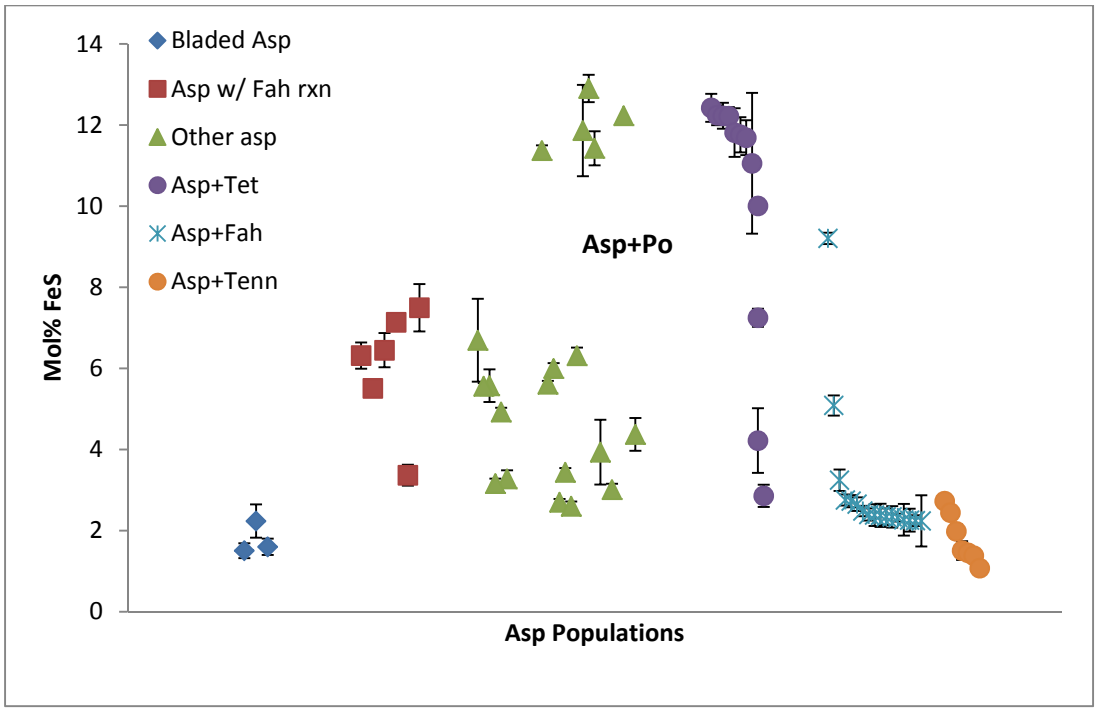

Figure 3.6: Mol% FeS in sphalerite for different arsenopyrite (Asp) textural-mineralogical associations. 'Fah rxn' refers to arsenopyrite intergrown with fahlore (Fah) + chalcopyrite.

Sphalerite compositions plotted on a plan view map (Figure 3.7) show that low FeS sphalerite (≤ 3mole% FeS) characterizes the southeast portion of the deposit but variably occurs in the central and northern portions of the mineralized footprint. In contrast, high FeS sphalerite (> 10mole % FeS) is restricted to the northern and western fringes of the mineralized footprint (Figure 3.7). These patterns are broadly consistent with Schmidt's (1983) boundary between bornite-bearing and pyrrhotite+ arsenopyrite-bearing assemblages (Figure 3.7).

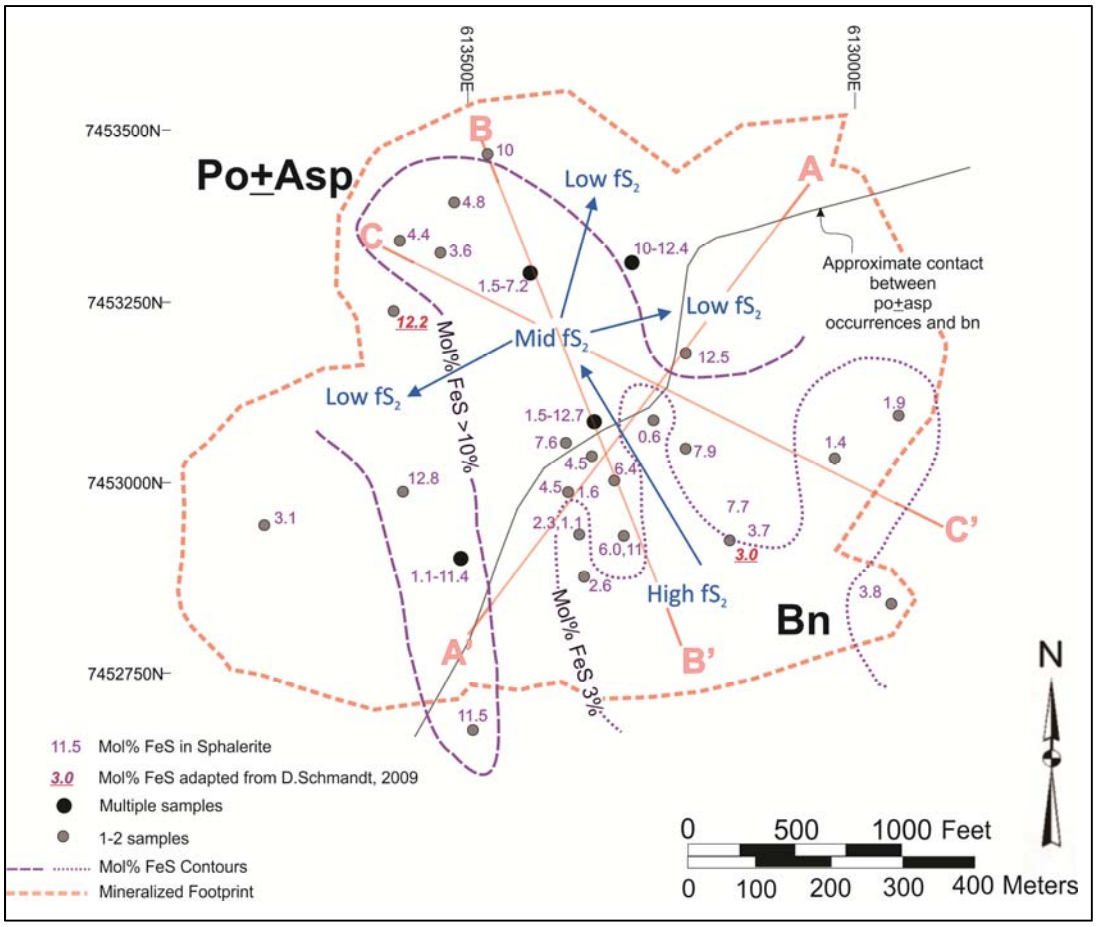

Figure 3.7: Distribution of mol% FeS in sphalerite through the deposit and pyrrhotite (po), arsenopyrite (asp), and bornite (bn) occurrences. Higher fS2 assemblage minerals including bn + low FeS sphalerite are abundant in the SE portion of the deposit with low FeS sphalerite also occurring in the central portions of the deposit. Low fS_2 assemblage minerals including po + asp + high FeS sphalerite are typically observed in the NW portion with high FeS sphalerite 'wrapping' around zones containing low FeS sphalerite. UTM grid is NAD 83, Zone 4.

Mol% FeS in sphalerite plotted vs. depth (m) show wide compositional variations for individual drill holes (Figure 3.8). Iron contents of sphalerite display sinusoidal patterns, especially noticeable in AR-0128 (Figure 3.8A), that reflect proximity to the gray schist (GS). Higher FeS sphalerite is spatially close to GS whereas low-FeS sphalerite is at least a meter from the closest GS. Similarly, sphalerite from drill hole AR-0131 contains uniformly high mol%FeS sphalerite presumably due to the close proximity of GS for all samples (Figure 3.8D). In the other drill holes, GS units are

present not just above and below sulfide intervals, but interfingered with massive sulfides (Figures 3.8 C,D and 3.9) resulting in sphalerite FeS patterns that are more complex.

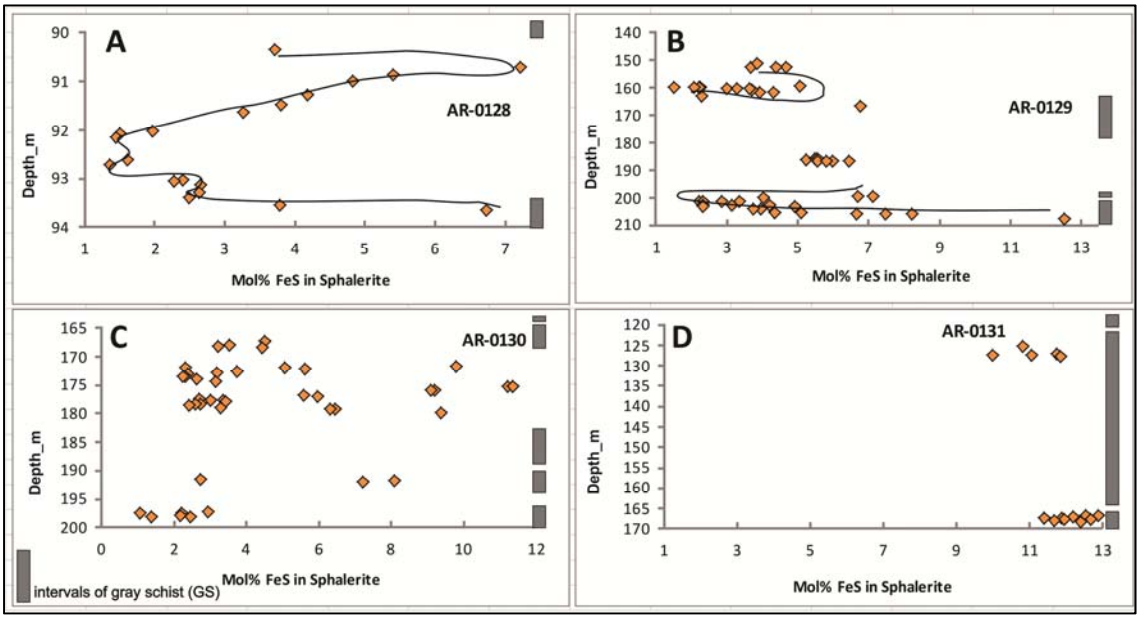

Figure 3.8: Depth distribution of mol% FeS in sphalerite through four drill holes. Gray schist (GS) intervals are plotted as gray boxes.

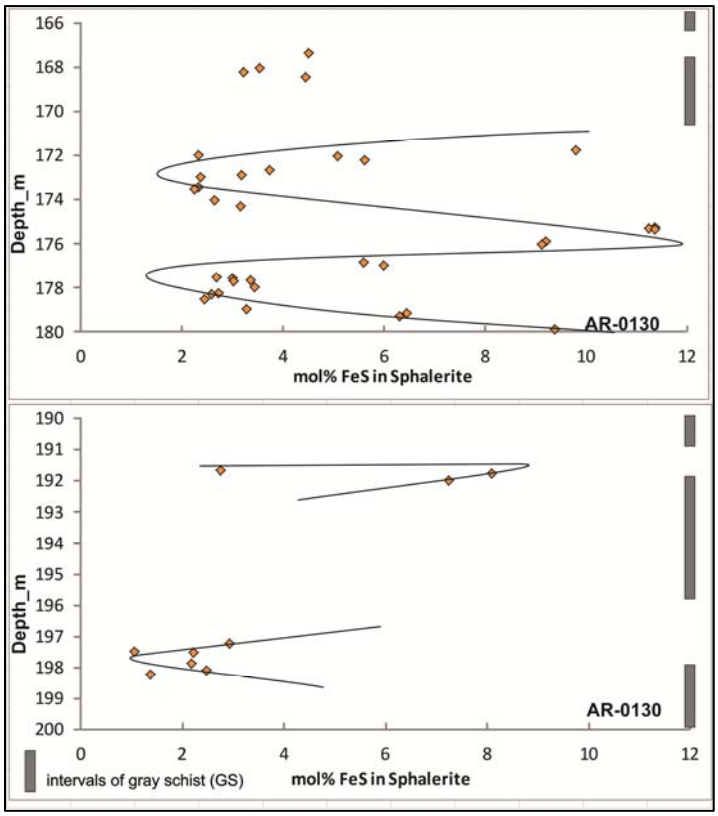

Figure 3.9: Depth distribution of mol% FeS in sphalerite in AR11-0130 shown at a detailed scale. Lines connect approximately sinusoidal compositional variations with depth, not visible at the scale of Figure 3.8. Gray schist (GS) intervals are indicated by gray boxes.

Figure 3.10 shows that mol% FeS in sphalerite generally increases with proximity to gray schist (GS). Sphalerite from AR-0128 clearly shows this relationship (Figure 3.10A); the highest value is at the contact between massive sulfide and GS, whereas the lowest values (1-2 mol% FeS) are found at the greatest distance from GS. Figure 3.10B (single values from multiple drill holes) shows a larger spread but generally follows the same relationship of AR-0128. The sphalerite from AR-089 (arrow, Figure 3.10B) is an outlier; however the unit less than half a meter away from this data point was logged as quartz mica schist—i.e., possibly bleached GS. If this unit really is GS, then the sphalerite from this sample would plot at 0.5 m, near the other high-FeS sphalerite data.

Sphalerite from AR-0129 and AR-0131 (grouped together, Figure 3.10C) generally exhibit a decrease in FeS with distance from GS. The point labeled with a question mark and an arrow represents where the geologist noted "possible graphitic

material" in the unit nearest this sphalerite analyses, but did not log the unit as GS. If the nearby unit really was GS, the point would be plotted only a few meters from GS. That is, all but a few data points exhibit the %FeS-distance relationship.

Sphalerite from AR-0130 (Figure 3.10D) starts to follow the decreasing FeS with increasing distance from GS relationship, but becomes more complex starting 4 meters away from GS. A missing interval, 2.5-3.8 meters from GS, for which data was not available might hold the key to this problem. I can only speculate on the structural and geologic complications that might be present in that missing interval. The spread of high to low %FeS from 4 to 8 meters could be explained by a faulted section of massive sulfide that originated closer to a GS unit.

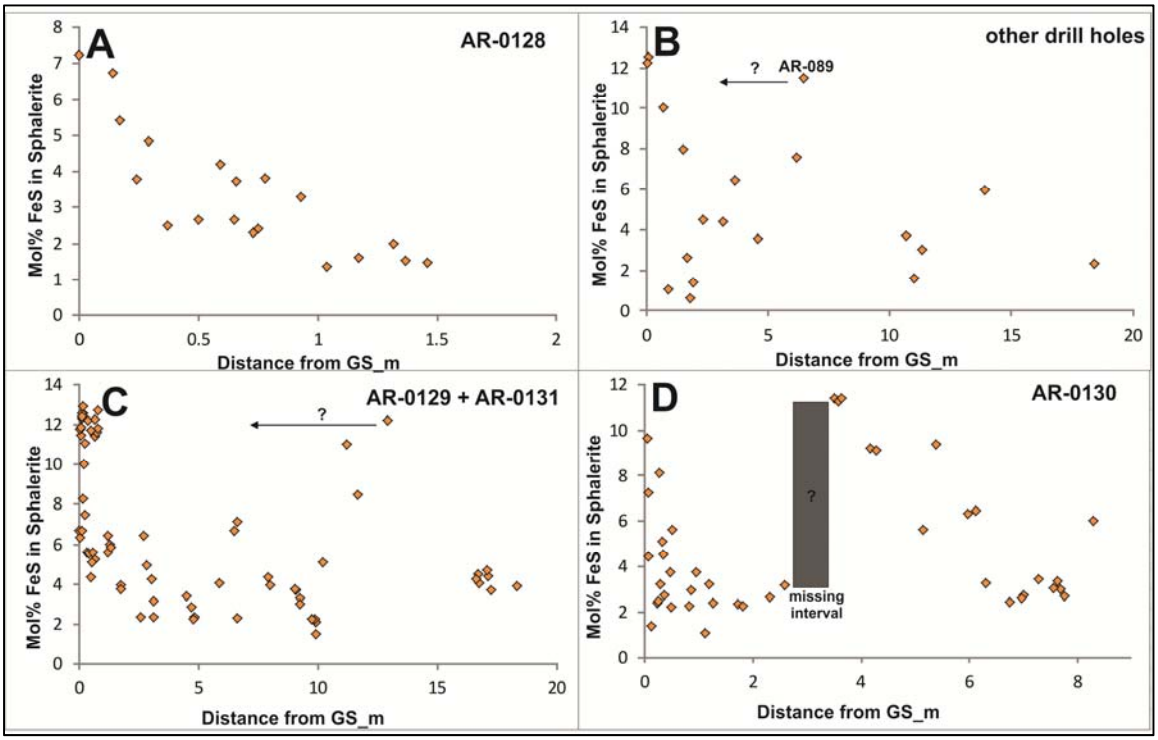

Figure 3.10: Distribution of mol% FeS in sphalerite vs. distance from gray schist (GS). For most samples from most drill holes high FeS sphalerite is restricted to the immediate vicinity of GS and falls with distance from GS. 3.10A, B, and D are from single (or two) drill holes; Figure 10C shows data for all other drill holes plotted together. The arrows with question marks indicate that these samples might be closer to GS or former GS.

Finally, mol% FeS in sphalerite also broadly correlates with compositions of associated phyllosilicate minerals (Figure 3.11). Silicates with high %Mg/(Mg+Fe) (Mg number), that is, low relative Fe contents, are present in samples with low-FeS sphalerite. Similarly, talc, which is characteristically low in Fe, occurs exclusively with low-FeS sphalerite, whereas stilpnomelane (characteristically high in Fe) only occurs with higher-FeS sphalerite.

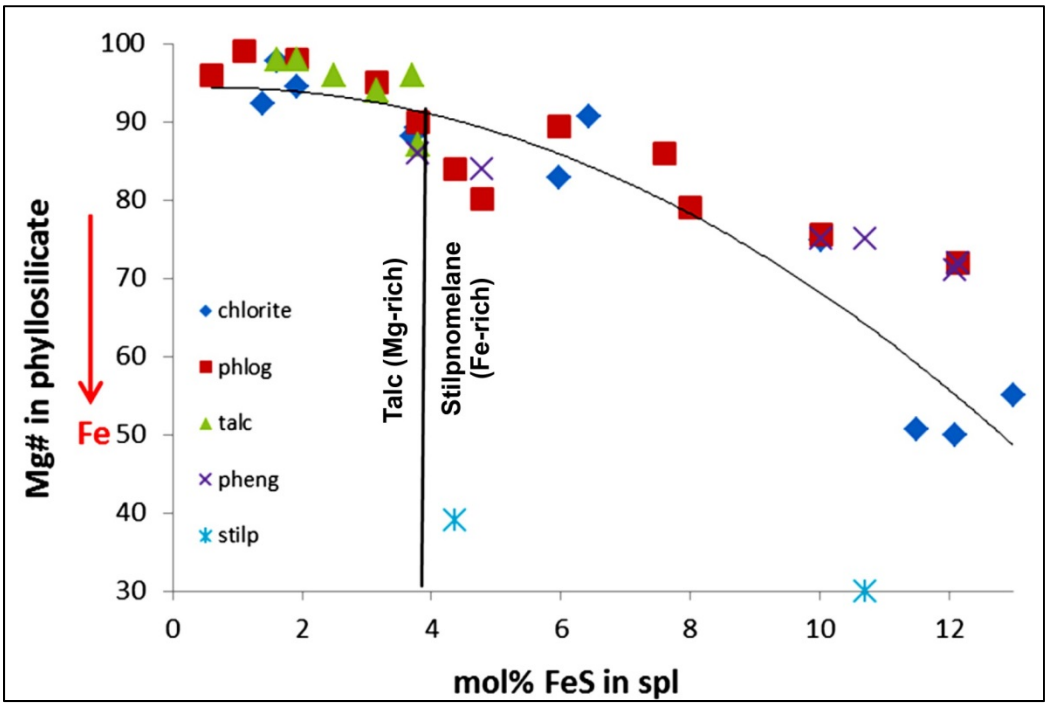

Figure 3.11: Mg# (% atomic Mg/Mg+Fe) in phyllosilicate minerals vs. mol% FeS in sphalerite. Increasingly Fe-rich (Mg-poor) sheet silicates are associated with increasingly FeS rich sphalerite. Additionally, talc (a Mg-rich mineral) is only associated with low-FeS sphalerite whereas stilpnomelane (an Fe-rich mineral) is exclusively associated with higher-FeS sphalerite. Most silicate mineral compositions are from Schmandt (2009). Stilpnomelane data and all but two sphalerite compositions are from this study. Phlogo = phlogopite; pheng = phengite; stilp = stilpnomelane.

3.3 Discussion

Based on compositions of sphalerite inclusions in pyrite grains (Figure 3.3), %FeS in sphalerite at Arctic increased progressively during metamorphism. That is, FeS content of sphalerite is not a measure of how much iron is in rock; it is a function of fS_2, fO_2, temperature (Figure 3.1), and pressure (e.g., Figure 3.2) during metamorphism. Further, the consistent relationship between sphalerite composition and associated

mineralogy (Figures 3.4, 3.6, and 3.11) indicates that equilibrium was attained among minerals in close proximity. Finally, significant differences in sphalerite composition through the deposit indicate the presence of significant variations in $fO_2 - fS_2$ during metamorphism.

The composition of sphalerite when present with pyrite + pyrrhotite is known to vary with pressure (e.g., Figure 3.2), but based on theoretical studies it should vary with temperature as well (Sack and Ebel, 2006). Unfortunately, there is no agreement in the literature about the best P-T compositional relationship. Figure 3.12 is a compilation of experimental and calculated data from various studies for 400Cº. Based on the best fit curve and the average composition of Arctic sphalerite with pyrite + pyrrhotite, I estimate a metamorphic pressure of 7$\pm$1 kb (Figure 3.12). This pressure is lower than Patrick's (1995) feldspar-phengite thermobarometry estimated value of 10$\pm$ 2 kb but overlaps within error. It is consistent with metamorphic conditions near the boundary between blueschist and greenschist inferred by Schmidt (1983). And there's no reason to think that the pressure derived from sphalerite compositions represents (or doesn't represent) the peak metamorphic conditions. In other words, the lack of complete agreement with the value given by Patrick (1995) is not cause for alarm.

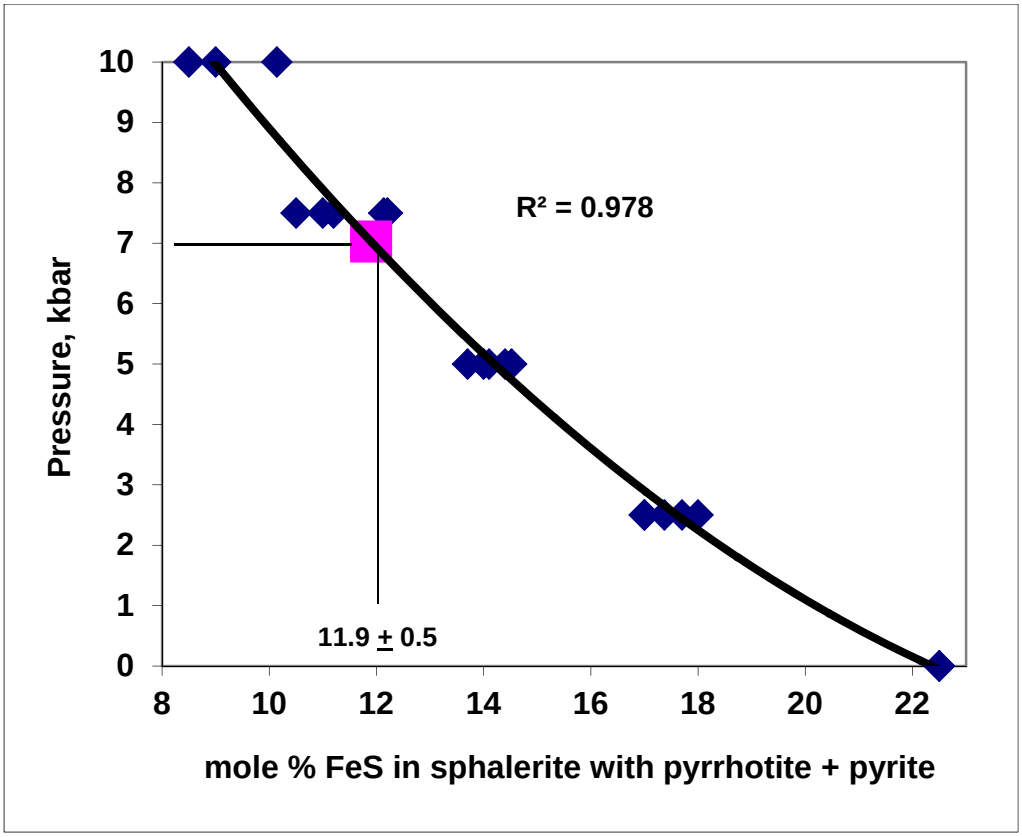

Figure 3.12: Compositions of sphalerite present with pyrite + pyrrhotite at 400C°. This graph is based on experimental and theoretical data (blue diamonds) compared to average Arctic sphalerite composition with pyrite + pyrrhotite (pink square). Best fit line gives metamorphic pressure of 7 ± 1 kb for Arctic metamorphism. Data from Scott (1976), Lusk & Ford (1978), Hutcheon (1978) and Toulmin et al. (1991).

The current state of knowledge is that most other sulfide equilibria are not as sensitive to pressure as iron content of sphalerite (Sack and Ebel, 2006). An exception is the upper stability of arsenopyrite, which moves to higher fS_2 with higher pressures (Lynch and Mengel, 1995). Figure 3.13 shows a first approximation for an appropriate fS_2-T diagram at 7 kb based on these considerations, together with compositional data for Arctic sphalerite.

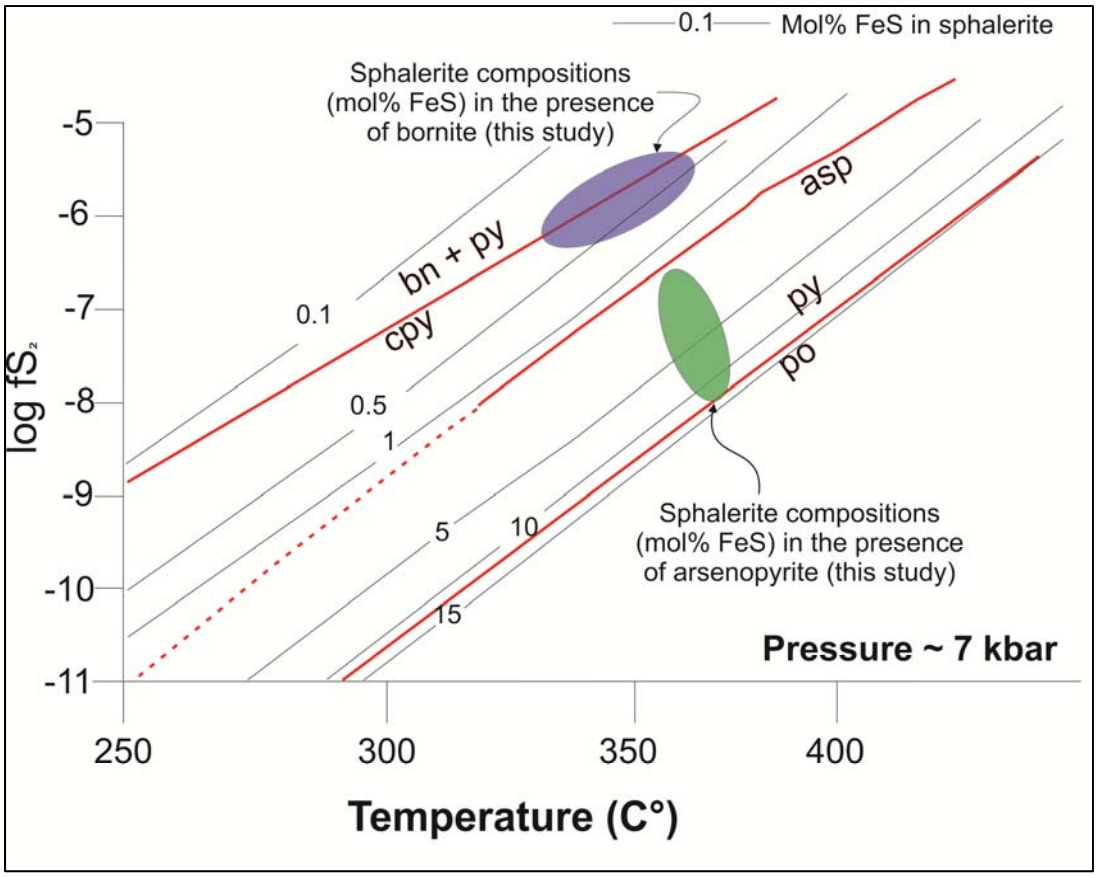

Figure 3.13: Estimated fS2-T diagram for 7 kbar with sphalerite compositional data, this study. Diagram is based on 1 bar equilibria (Vaughn and Craig, 1997) with adjustments in iron composition of sphalerite from Sack and Ebel (2006) and arsenopyrite stability from Lynch and Mengel (1995).

Arsenopyrite is stable with relatively Fe-poor sphalerite at 7 kb (Figure 3.13). At 1 bar (Figure 3.1) arsenopyrite should only occur with sphalerite containing $\geq$ 10 mole%FeS, but sphalerite coexisting with pyrite + pyrrhotite should also have extremely high (>20) % FeS (Figure 3.1). The 'anomalous' sphalerite compositions shown in Figure 3.4, in fact, make perfect sense for metamorphism at approximately 7 kb and a temperature in the vicinity of 400C°. That is, sphalerite with FeS as low as 2 mole% (Figure 3.13) should be stable with arsenopyrite—as is observed (Figure 3.4).

An additional complication to arsenopyrite stability in the presence of Cu and Sb is the reaction: $4FeAsS + 10CuFeS_2 + 13/2\ S_2 = Cu_{10}Fe_2As_4S_{13} + 12FeS_2$. In other words, in the presence of chalcopyrite at excess S_2, arsenopyrite forms tennantite (As-fahlore) + pyrite. The location of this equilibrium is not currently known, but is believed

to lie (Sack and Ebel, 2006) in the vicinity of the upper stability of arsenopyrite. I suspect that the arsenopyrite-fahlore-chalcopyrite intergrowths present in 6 samples at Arctic (Figure 3.5) represent such a reaction. That is, the upper fS_2 limit of arsenopyrite with chalcopyrite and fahlore is lower than without those minerals. Sphalerite in the presence of arsenopyrite + fahlore + chalcopyrite has compositions of about 7 mole% FeS (Figure 3.6). This composition is possible due to the change in the upper stability of arsenopyrite with increasing pressure (Figure 3.13).

Sphalerite compositions at Arctic represent wide variations in fS_2 at approximately constant pressure and temperature. Such variations happen through the reaction: $(1\text{-}n)\ ZnS + nFeS_2 = (Zn, Fe)S + n/2\ S_2$. The compositions also vary with proximity to the gray schist (GS), as illustrated in Figure 3.10, indicating that graphite presence affects fS_2. Graphite requires and stabilizes low fO_2 and low fS_2 conditions, expressed by the reaction $2FeS_2 + 2H_2O\ (g) + C \rightarrow 2FeS + 2H_2S(g) + CO_2$ (Hall, 1986). The conversion (de-sulfidation) of pyrite to pyrrhotite requires reduction of S_2^{2-} in pyrite (effectively S^-) to S^{2-} in pyrrhotite and H_2S. C (graphite) acts as the source of electrons for that reduction and CO_2 is the oxidized product of that reduction. The value of $\log fO_2$ for graphite stability **does** depend on fCO_2, but only changes appreciably for extremely small values. The presence of calcite (instead of anhydrite) at Arctic (Figure 3.14) indicates that fCO_2 was not extremely small.

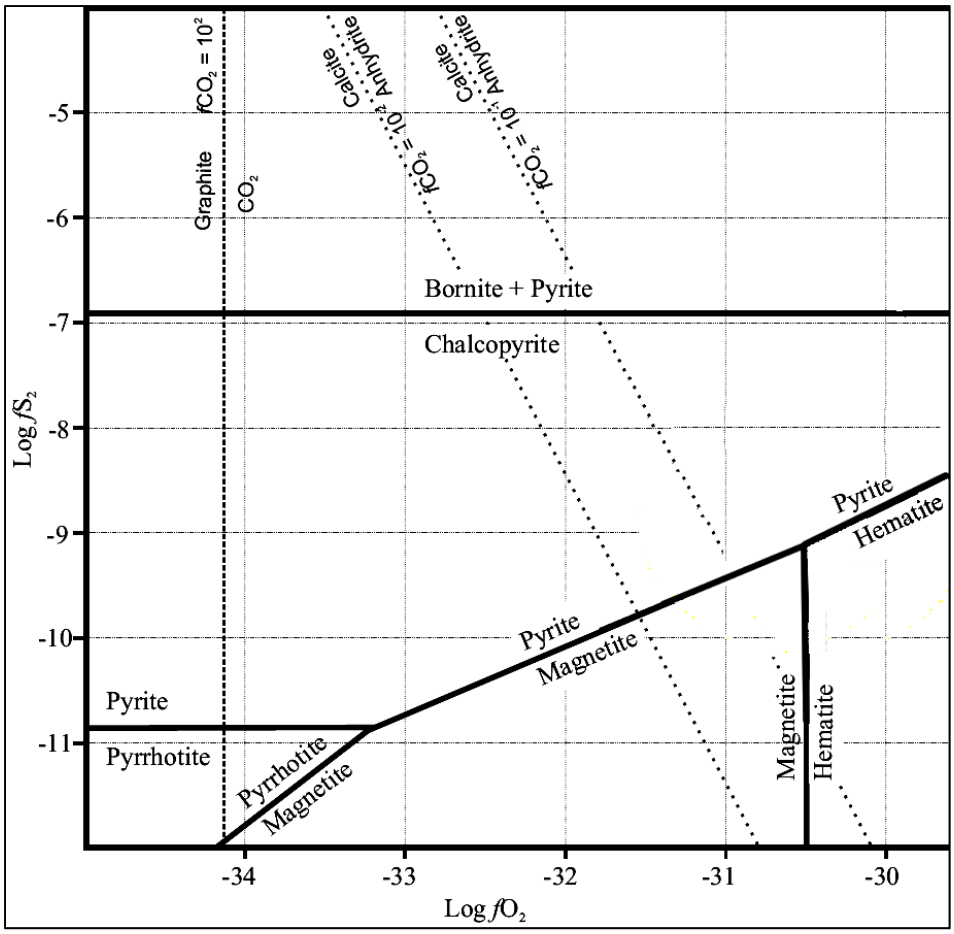

Figure 3.14: Log fO_2-log fS_2 diagram for Fe-Cu-S-O minerals at 300°C and 2.5 kb. Modified from Hunt (2005).

In sum, low fS_2 conditions are created by the low fO_2 conditions that graphite produces, and wherever massive sulfide is in the immediate vicinity of GS, sphalerite contains high FeS (Figure 3.10). Conversely, low-Fe sphalerite is invariably present with the high fS_2 assemblage of chalcopyrite-bornite-pyrite (Figure 3.14).

A semi schematic fO_2-fS_2 diagram built around a diagram for elevated pressures and 300C° illustrates the possible fO_2 gradients at Arctic and their influence on sulfide and silicate mineralogy (Figure 3.15). The assemblages range from condition 1 with bornite + pyrite + very low FeS sphalerite to condition 4 with graphite, pyrrhotite + pyrite + high FeS-sphalerite. Condition 1—high fS_2, high fO_2— represents conditions at which minerals including very low Fe sphalerite (~0.5 mol% FeS), bornite, chalcopyrite, pyrite,

tennantite, barite, high-Mg silicates, and calcite are stable, a condition representing that of typical Kuroko VMS deposits (Figure 3.1; Ono and Sato, 1995; Kitazono and Ueno, 2003). Condition 2 represents fS_2-fO_2 conditions for much of the deposit, characterized by low-Fe sphalerite (2-4 mol% FeS), chalcopyrite, pyrite, tennantite, moderate Mg-silicates ($phl_{90}An_{10}$), barite, calcite, and magnetite (Figure 3.15), which are stable together. Bornite is no longer stable and arsenopyrite might be locally present. As fS_2-fO_2 conditions reach 3, iron continues to be partitioned from pyrite into sphalerite and sheet silicates. Arsenopyrite is stable, along with intermediate-Fe sphalerite (5-7 mole% FeS) and Fe-silicates such as stilpnomelane and Fe-chlorite become abundant. Barite ($BaSO_4$) is no longer stable under these conditions and transforms into a silicate represented on Figure 3.15 by sanbornite ($BaSi_2O_5$). At Arctic, the barium silicate cymrite ($BaAl_2Si_2O_8 * nH_2O$) is observed as a significant phase, but unfortunately there is no thermodynamic data for this mineral. The conversion of sulfate in barite to sulfide is caused by a reduction from nearby graphite—that is: $SO_4^{2-} + 2C = 2CO_2 + S^{2-}$. Condition 3 also represents a common assemblage at Arctic—moderate FeS sphalerite, arsenopyrite, fahlore, chalcopyrite and pyrite. The lowest fS_2-fO_2 conditions experienced at Arctic (Condition 4) contains pyrrhotite, graphite (stabilizing low fO_2), high Fe-sphalerite (>10 mol% FeS), arsenopyrite + chalcopyrite, and Fe-rich silicates (Figure 3.15). Just as this assemblage is representative of the lowest fS_2-fO_2 conditions observed at Arctic, the assemblage bornite + pyrite (Condition 1) represent the highest fS_2-fO_2 conditions experienced. Variations of different mineralogic assemblages between these two extremes can be observed at Arctic—that is, at any given point within the deposit, fS_2-fO_2 conditions might be mapped by using mineral associations including sphalerite compositions.

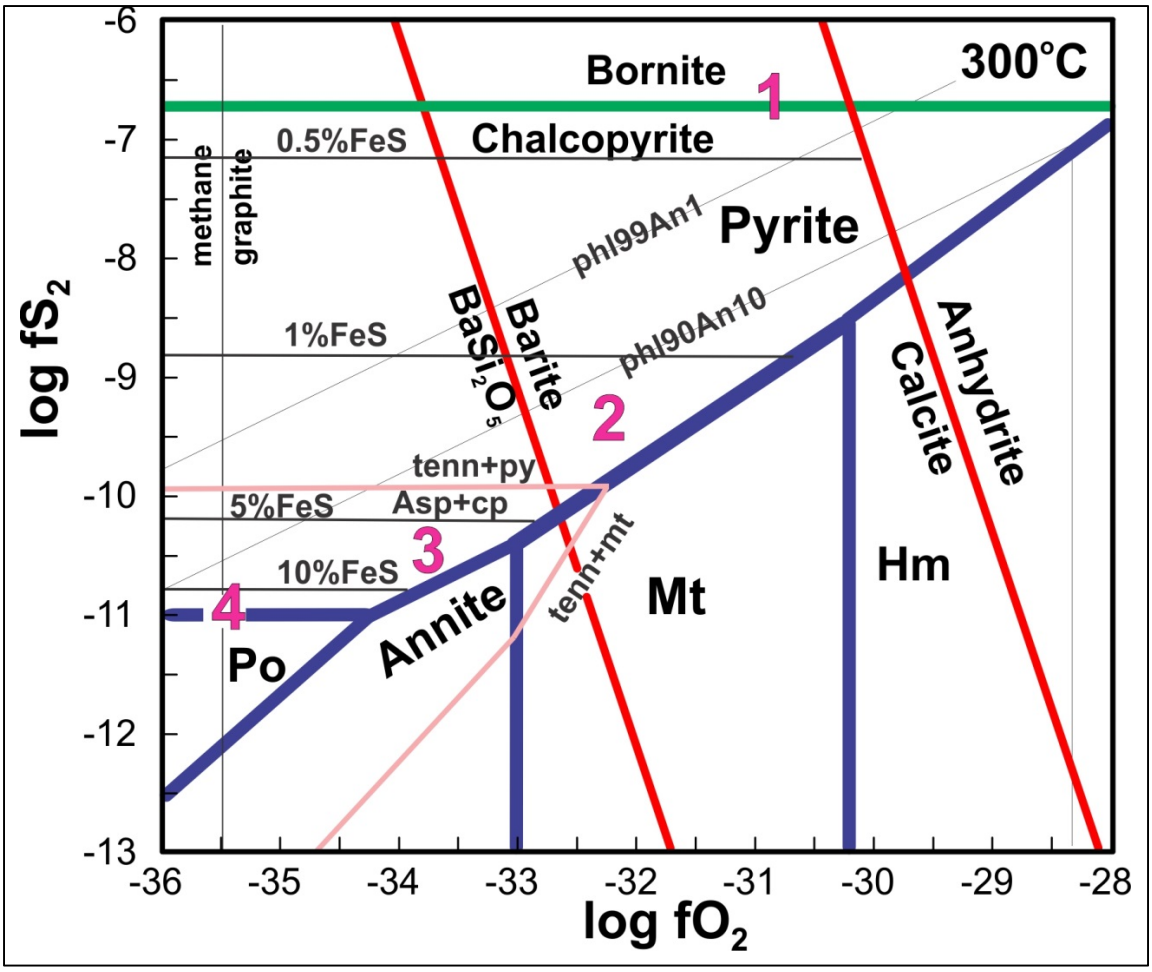

Figure 3.15: Semi-schematic log fO_2-fS_2 diagram for conditions broadly applicable to metamorphism at Arctic. Diagram is modified from Hunt (2005) with additional equilibria using the program "The Geochemists Workbench" release 4.0.2 (Bethe, 2000) and approximate shifts in mineral stability for elevated pressures (Figure 3.13). Light diagonal lines show approximate upper stability for biotite solid solution with 10% (Phl90An10) and 1% (phl99An1) of the Fe-end member. Conditions 1 through 4 represent the highest and lowest fS_2-fO_2 conditions seen, respectively, at Arctic. Po = pyrrhotite, Mt = magnetite, Hm = hematite, tenn = tennantite, Asp = arsenopyrite, cp = chalcopyrite, phl = phlogopite, An = annite.

The involvement of silicates in the various metamorphic reactions can be represented by ½ O_2 + $MgSiO_3$ + SiO_2 + FeS_2 ➔ $MgFeSi_2O_6$ + S_2, showing that lower fS_2 conditions allow for more Fe in silicates as well as in sphalerite. Pure Fe silicates (e.g., Fe-biotite) do not occur at Arctic, but stilpnomelane is an iron-rich mineral that can approximate Fe-rich biotite. The curves for biotite of differing Fe contents are thus compatible with the observed relation between higher-Fe sphalerite and silicates (Figures 3.11 and 3.15).

The net result is that at a given spot in the deposit, even though P and T are uniform, the competition between these reactions resulted in conditions during metamorphism which varied from strongly reducing to moderately oxidizing. Nevertheless, at any given spot, the fS_2-fO_2 conditions are apparently uniform, resulting in a consistent sulfide-silicate assemblage (e.g., Figure 3.11).

Metamorphism of an original Kuroko assemblage can also be demonstrated by considering the variable Ba mineralogy. Kuroko VMS deposits contain abundant barite and lack barium silicates. During metamorphism in the presence of SiO_2 and Al_2O_3, SO_4^{2-} in barite was reduced to S_2, releasing Ba^{2+} to form Ba-silicates, e.g., cymrite ($BaAl_2Si_2O_8 * nH_2O$). Ba is also present in other silicates such as Ba-stilpnomelane, Ba-micas (Schmandt, 2009), and even rare barium carbonate.

3.4 Conclusion

Sphalerite compositions vary in the Arctic deposit in a manner indicating equilibrium with other sulfide and silicate minerals with variable fS_2-fO_2 conditions. The spatial pattern of FeS contents of sphalerite is complex (Figure 3.7), reflecting an overall increase in the amount of graphitic rock on the margins of the deposit. This graphitic rock caused low fO_2-fS_2 conditions and associated high-Fe sphalerite. At the SE end of the deposit, however, the absence of graphitic rock allowed the deposit to retain its original Kuroko assemblage of low-Fe sphalerite + bornite + chalcopyrite + pyrite—that is, a moderate to high fO_2-fS_2 assemblage (Figure 3.7). Between these two extremes, sphalerite compositions vary considerably within a given drill hole (Figures 3.9 and 3.10), reflecting local proximity to the reducing graphitic schist. Variations in fS_2-fO_2 at Arctic are ultimately responsible for determining the stable mineral assemblages of both sulfides and silicates, as well as the amount of Fe partitioned into sphalerite. These relationships also suggest that other elements—for example, silver—would have been re-partitioned into new minerals during metamorphism.

Chapter 4 Silver Deportment

4.1 Introduction

Silver in Kuroko deposits is typically found in the black ore as minerals including stromeyerite (AgCuS), pearceite ($Cu(Ag,Cu)_6Ag_9As_2S_{11}$), mckinstryite ($Ag_{5-x}Cu_{3+x}S$), fahlore (tennenatite-tetrahedrite) and electrum (Au-Ag) (Ono and Sato, 1995; Glasby et al., 2008). In contrast, from limited sample investigations, Stephens and Cameron (1970) reported most of the silver at Arctic is in argentiferous galena (PbS) and argentiferous tetrahedrite ($Cu_{10}(Fe,Zn)_2Sb_4S_{13}$) with minor amounts in stromeyerite and electrum.

The question of 'where is the silver at Arctic?' is illustrated by the poor correlation between Ag and other elements in drill core assays (Figure 4.1). Ag correlates as well with Zn as with Pb, despite the presence of Ag in galena and its absence in sphalerite. Ag shows no correlation with Sb, despite Ag in tetrahedrite. Whereas the Ag-Zn correlation simply implies that Ag increases with total sulfide, the Ag-Bi correlation (despite the low concentrations of each) implies at least a weak Ag-Bi relationship.

Silver substitutes into sulfide minerals via two routes: direct substitution for Cu^+ and coupled substitution for other ions, chiefly Pb^{2+}. Ag^+ is larger than Cu^+ (Table 4.1); therefore, it substitutes with difficulty. However Ag^+ substitutes much better for Cu^+ than it does for the much smaller Cu^{2+} ion. Consequently, Ag^+ substitutes for Cu in bornite (the bulk of Cu is Cu^+) and rarely in chalcopyrite (all of the Cu is Cu^{2+}). Further, Ag^+ substitutes much better for Cu^+ in tetrahedrite ($Cu_{10}Fe_2Sb_4S_{13}$) than in tennantite ($Cu_{10}Fe_2As_4S_{13}$) because the inclusion of the larger Sb ion in tetrahedrite makes the entire lattice larger than that of tennantite (As-rich). This unit cell expansion allows for more Ag^+ incorporation into tetrahedrite, as shown by world-wide data. (Figure 4.2; Sack and Ebel, 2006).

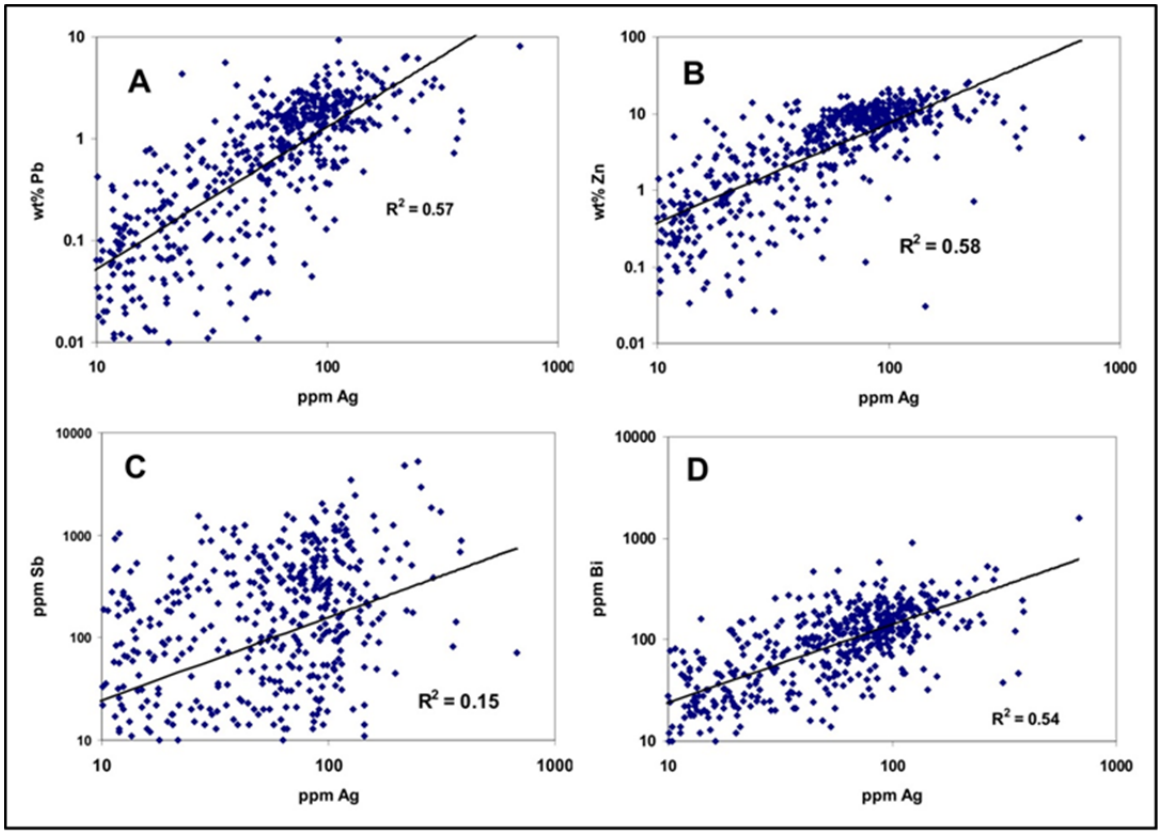

Figure 4.1: Correlations of Pb (A), Zn (B), Sb (C) and Bi (D) with Ag from Arctic deposit drill core assays.

Table 4.1: Size Table for Ions in 4- and 6-fold Coordination Sites

Ion	Charge	Coordination	Ionic Radius
Cu	+1	6-fold	0.77
	+2	6-fold	0.73
Ag	+1	6-fold	1.15
Bi	+3	6-fold	1.03
Pb	+2	6-fold	1.19
Sb	+3	6-fold	0.76
As	+3	6-fold	0.58
S	-2	4-fold	1.84
Se	-2	6-fold	1.98

Modified from Shannon (1976).

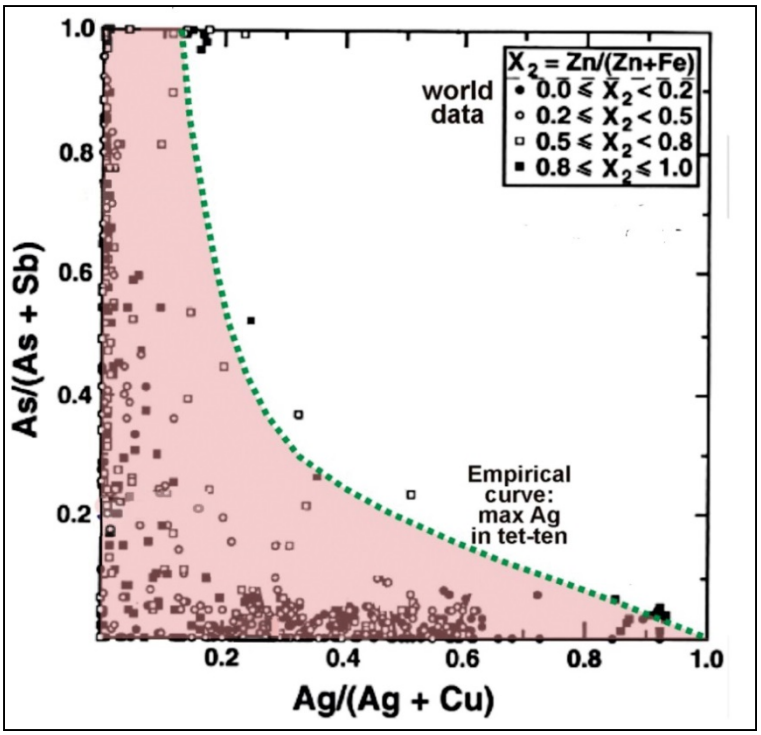

Figure 4.2: Correlation of atomic Ag/(Ag+Cu) with Sb/(As+Sb) in fahlore. As Sb/(As+Sb) increases, Ag/(Ag+Cu) also increases (modified from Sack and Ebel, 2006).

Although Ag^{+} and Pb^{2+} are approximately the same size, they cannot directly substitute for each other due to the differences in charge. Instead, a coupled substitution of Ag^{+} + either Sb^{3+} or Bi^{3+} for $2Pb^{2+}$ occurs. Experimental data show that $AgBiS_2$ displays complete solid solution with Pb_2S_2 to at least temperatures of 375C°, whereas the Sb substitution is much more limited at 375C° (Chutas et al., 2008). Since both Sb and Bi are present in Arctic ore (Figure 4.1) either or both might be coupled with Ag in galena. Both Sb and Bi could also occur in other sulfide minerals.

In this chapter, I examine the mineralogical distribution of silver in the Arctic deposit using a combination of optical petrography, electron microprobe, and X-Ray fluorescence (XRF) analyses. Based on microprobe examination of approximately 150 samples representing multiple mineral assemblages throughout the deposit combined with XRF analyses of 28 samples, appreciable (>0.5%) Ag is present in galena, fahlore, and bornite. The concentration of Ag in each mineral varies with the abundance of the

host mineral and location in the deposit. I interpret these variations as due to elemental redistribution during metamorphism.

4.2 Distribution of Silver in Galena

Microprobe analysis of individual grains shows that galena (PbS) contains 0.02–0.9 wt% Ag and 0.07 - 1.8% Bi (Table 4.2). I was unable to detect Sb or As above the microprobe detection limit of approximately 0.03 % and 0.1%, respectively (Appendix 1). The analyses display a strong Bi-Ag correlation, with an atomic ratio of approximately 1:1 (Figure 4.3; Table 4.2). Atomic Bi:Ag ratios vary from 2 ± 2 to 0.3 ± 0.3 (Table 4.2) reflecting the high degree of analytical uncertainty for samples containing Ag and Bi near the microprobe detection limit. For the 114 samples with > 0.2% Ag and Bi, however, the average atomic Bi:Ag ratio is 1.0 ± 0.1. These relations indicate that the bulk of Ag in Arctic galena is through the coupled substitution of $Bi^{3+}$and Ag^{+} for 2 Pb^{2+}.

Because Se^{2-} is significantly larger than S^{2-} whereas Bi^{3+} is smaller than Pb^{2+} (Table 4.1), I investigated the possibility that the Se content is related to the Ag-Bi content of galena. Analyses for Se in eight samples (Figure 4.4) indicate that Se does not correlate with Bi (or Ag). However, with the exception of a bornite-rich sample, low-Bi (Ag) galena contains little Se (Figure 4.4). Although the variably high Se content of galena explains the high Se (500-1000 ppm) observed at Arctic, the Se apparently has no bearing on Bi in galena.

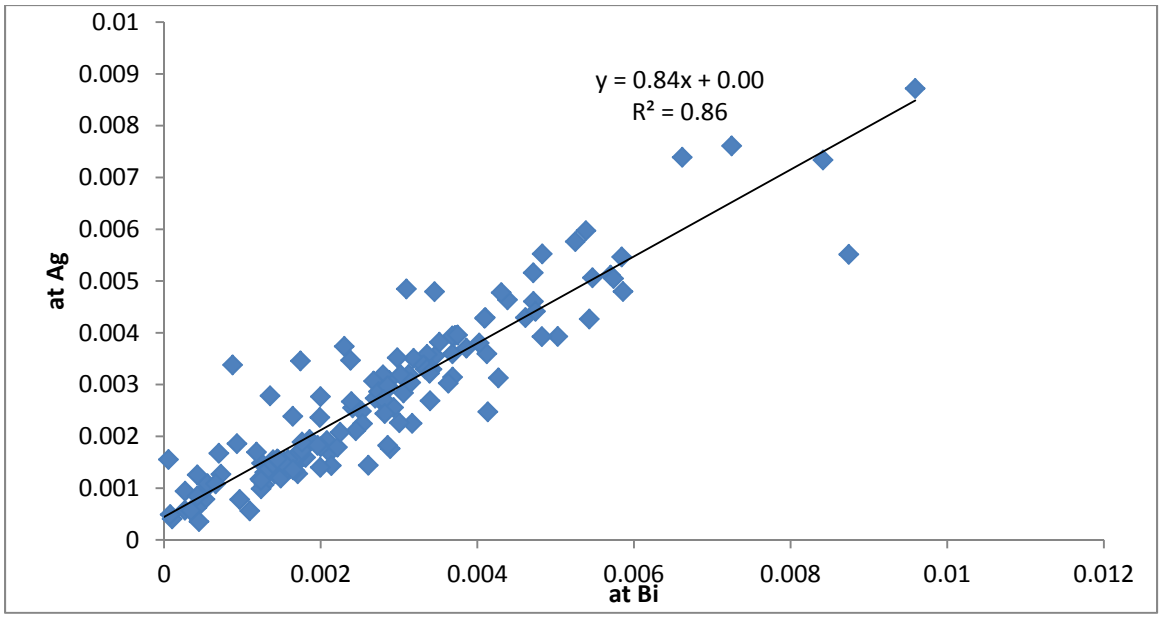

Figure 4.3: Atomic Bi vs. atomic Ag in galena from the Arctic Deposit. Most points represent the average of at least 3 analyses from 3 different grains. In most cases the compositions in a single sample vary by less than 10%.

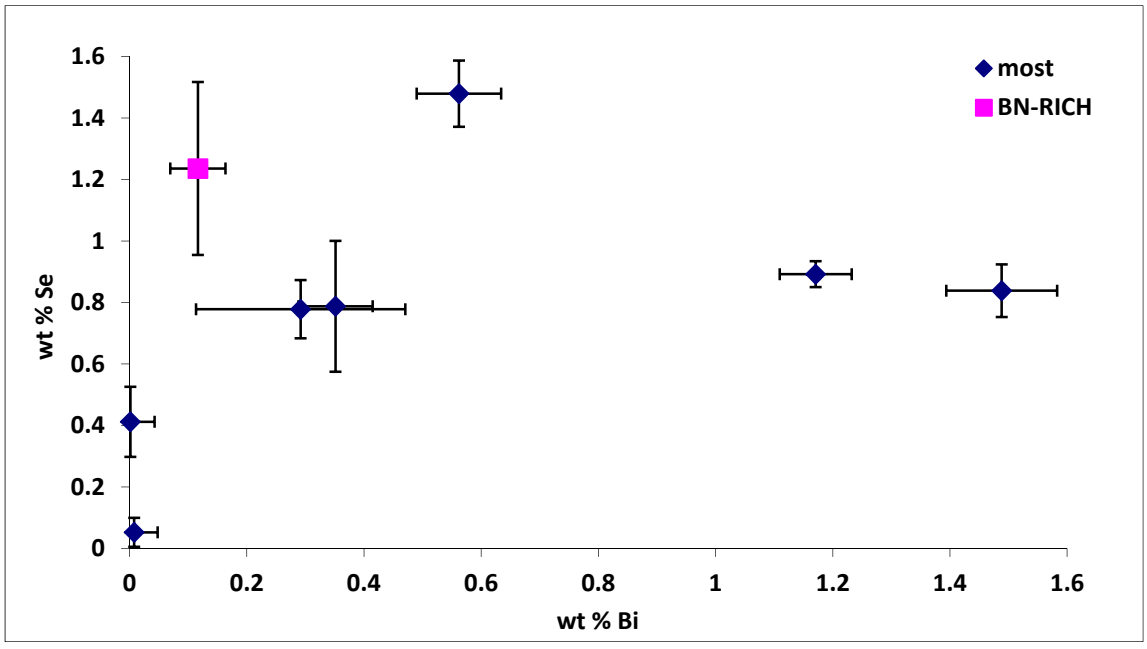

Figure 4.4: Average Bi vs. Se concentrations in galena from 8 Arctic samples. Although low Bi (low Ag) galena contains low Se, most of the galena samples contain similar Se abundances, independent of Bi.

Table 4.2: Silver Contents of Galena by Electron Microprobe

Sample	Drill hole	Depth	Wt% Ag	St Dev	W% Bi	St Dev	At Bi/Ag	St Dev	Wt [1] % Se	St Dev
197-1	128	90.69	0.29	0.04	0.71	0.08	1.2	0.3		
197-2	128	90.86	0.33	0.06	0.60	0.10	0.9	0.3		
197-3	128	90.98	0.52	0.12	1.22	0.23	1.2	0.5		
197-5	128	91.345	0.55	0.04	1.19	0.08	1.1	0.2		
197-6	128	91.47	0.39	0.03	0.77	0.05	1.0	0.1		
197-7	128	91.62	0.39	0.04	0.86	0.07	1.2	0.2		
197-8	128	92.01	0.38	0.04	0.72	0.07	1.0	0.2		
197-9	128	92.06	0.46	0.05	0.96	0.17	1.1	0.3		
198-1	128	92.15	0.34	0.04	0.65	0.08	1.0	0.2		
198-6	128	93.115	0.40	0.03	0.81	0.07	1.0	0.2		
198-7	128	93.265	0.31	0.03	0.59	0.06	1.0	0.2		
198-8	128	93.39	0.34	0.04	0.89	0.05	1.4	0.2		
198-9	128	93.525	0.50	0.03	0.92	0.07	1.0	0.1		
199-1	128	93.62	0.12	0.02	0.07	0.04	0.3	0.2		
178-1	129	200.06	0.18	0.04	0.44	0.12	1.3	0.6		
178-2	129	103.85	0.46	0.05	0.86	0.14	1.0	0.3		
177-1	129	151.31	0.39	0.02	0.70	0.05	1.0	0.1		
176-1	129	152.42	0.36	0.04	0.71	0.06	1.0	0.2		
180-5	129	152.53	0.19	0.01	0.61	0.09	1.7	0.3		
180-4	129	201.42	0.18*		0.38 *		1.1*			
180-3	129	152.57	0.17	0.05	0.38	0.14	1.1	0.8		
180-2	129	152.905	0.41	0.03	0.84	0.10	1.1	0.2		
180-1	129	152.94	0.34	0.03	0.77	0.08	1.2	0.2		
179-1	129	200.86	0.29	0.02	0.55	0.05	1.0	0.2		
184-1	129	153.04	0.37	0.02	0.71	0.06	1.0	0.1		
182-3	129	157.97	0.31	0.02	0.64	0.08	1.1	0.2		
182-2	129	158.43	0.27	0.02	0.52	0.06	1.0	0.2		
182-1	129	159.456	0.13	0.15	0.21	0.45	1.0	1.0		
183-2	129	159.73	0.53	0.19	1.08	0.46	1.1	1.0		
183-1	129	159.75	0.29	0.08	0.61	0.10	1.1	0.5		
186-1	129	159.78	0.79	0.11	1.76	0.13	1.2	0.3		
185-2	129	159.89	0.46	0.02	0.86	0.12	1.0	0.2		
185-1	129	159.905	0.43	0.16	0.78	0.35	1.0	0.9		
184-2	129	160.41	0.36	0.03	0.70	0.07	1.0	0.2		
188-2	129	160.425	0.38	0.25	0.67	0.60	1.0	2.5		
188-1	129	160.58	0.43	0.13	0.76	0.29	1.0	0.7		
186-3	129	160.605	0.59	0.09	1.22	0.13	1.0	0.3		

TABLE 4.2 CONT.: Silver Contents of Galena by Electron Microprobe

Sample	Drill hole	Depth	Wt% Ag	St Dev	Wt % Bi	St Dev	At Bi/Ag	St Dev	Wt [1] % Se	St Dev
186-2	129	161.66	0.48	0.07	0.99	0.11	1.1	0.3		
168-1	129	161.75	0.33	0.03	0.56	0.07	0.9	0.2		
167-2	129	163.03	0.67	0.03	1.17	0.19	1.0	0.2		
167-1	129	166.95	0.64	0.02	1.13	0.06	1.0	0.1		
166-2	129	185.63	0.80	0.11	1.38	0.14	1.0	0.2		
166-1	129	185.64	0.50	0.15	0.79	0.28	0.8	0.6		
164-3	129	185.96	0.36	0.04	0.69	0.09	1.0	0.2		
164-2	129	186.01	0.33	0.05	0.57	0.07	0.9	0.3		
164-1	129	186.21	0.31	0.03	0.57	0.09	1.0	0.2		
165-2	129	186.29	0.56	0.04	0.99	0.10	1.0	0.2		
165-1	129	186.82	0.53	0.07	0.94	0.16	1.0	0.3		
163-2	129	186.83	0.36	0.03	0.70	0.17	1.0	0.4		
163-1	129	186.895	0.42	0.02	0.77	0.09	1.0	0.2		
162-1	129	186.955	0.62	0.04	1.10	0.09	1.0	0.1		
157-3	129	199.39	0.39	0.03	0.65	0.07	0.9	0.2		
157-2	129	199.515	0.38	0.04	0.72	0.13	1.0	0.3		
157-1	129	200.13	0.45	0.05	0.80	0.11	1.0	0.2		
155-6	129	201.2	0.44	0.04	0.81	0.08	1.0	0.2		
174-4	129	201.215	0.14	0.02	0.30	0.09	1.1	0.5		
173-3	129	201.32	0.15	0.02	0.31	0.06	1.1	0.4		
173-2	129	201.5	0.15	0.02	0.35	0.08	1.2	0.4		
173-1	129	202.875	0.11	0.02	0.27	0.08	1.2	0.6		
175-3	129	202.91	0.21	0.03	0.39	0.06	1.0	0.3		
175-2	129	202.99	0.06	0.01	0.08	0.06	0.6	0.6		
175-1	129	203.2	0.21	0.02	0.43	0.07	1.1	0.3		
158-3	129	203.45	0.46	0.14	1.13	0.29	1.3	0.8		
158-2	129	204.25	0.33	0.12	0.76	0.27	1.2	1.0		
158-1	129	204.26	0.32	0.10	0.60	0.44	1.0	1.1		
153-1	129	205.47	0.17	0.06	0.32	0.30	1.0	1.3		
172-2	129	205.77	0.10	0.07	0.26	0.09	1.3	2.9		
190-5	130	168.44	0.08	0.02	0.11	0.12	0.7	1.0		
191-1	130	171.75	0.15	0.01	0.21	0.05	0.8	0.2		
191-2	130	171.95	0.21	0.01	0.53	0.06	1.3	0.2		
191-3	130	172.04	0.10	0.02	0.27	0.06	1.3	0.5		
191-4	130	172.21	0.14	0.02	0.27	0.05	1.0	0.3		
191-5	130	172.66	0.18	0.02	0.35	0.07	1.0	0.3		
191-6	130	172.9	0.33	0.02	0.66	0.06	1.0	0.2		

TABLE 4.2 CONT.: Silver Contents of Galena by Electron Microprobe

Sample	Drill hole	Depth	Wt% Ag	St Dev	Wt % Bi	St Dev	At Bi/Ag	St Dev	Wt [1] % Se	St Dev
192-2	130	173.44	0.13	0.02	0.26	0.05	1.0	0.4		
192-3	130	173.52	0.18	0.04	0.36	0.15	1.1	0.7		
192-4	130	173.55	0.14	0.01	0.35	0.08	1.3	0.4		
192-5	130	174.025	0.19	0.02	0.42	0.05	1.1	0.3		
192-6	130	174.3	0.94	0.05	2.00	0.08	1.1	0.1		
192-7	130	175.22	0.29	0.03	0.59	0.12	1.0	0.3		
192-8	130	175.29	0.28	0.03	0.50	0.14	1.0	0.4		
192-9	130	175.35	0.29	0.09	0.50	0.16	0.9	0.6		
193-1	130	175.89	0.15	0.03	0.45	0.08	1.5	0.6		
193-2	130	176	0.15	0.02	0.42	0.08	1.4	0.5		
193-3	130	176.85	0.24	0.02	0.53	0.13	1.1	0.4		
193-4	130	176.96	0.23	0.03	0.51	0.06	1.2	0.3		
193-5	130	177.5	0.20	0.03	0.41	0.04	1.1	0.3		
193-6	130	177.57	0.24	0.03	0.66	0.06	1.4	0.3		
193-7	130	177.635	0.26	0.01	0.59	0.08	1.2	0.2		
193-9	130	177.98	0.42	0.04	1.05	0.09	1.3	0.2		
194-1 Tet	130	178.26	0.42	0.05	1.01	0.16	1.2	0.4		
194-3	130	178.51	0.54	0.17	1.20	0.37	1.1	0.8		
194-4	130	178.96	0.59	0.11	1.83	0.28	1.6	0.6		
194-5	130	179.14	0.27	0.02	0.86	0.15	1.7	0.4		
194-6	130	179.28	0.35	0.03	0.71	0.05	1.1	0.2		
194-7	130	179.88	0.11	0.01	0.11	0.05	0.5	0.3		
195-1	130	191.66	0.20	0.04	0.60	0.10	1.6	0.6		
195-2	130	191.76	0.24	0.05	0.63	0.10	1.3	0.5		
195-3	130	191.96	0.16	0.03	0.54	0.08	1.8	0.6		
196-1	130	197.22	0.16	0.01	0.29	0.05	1.0	0.2		
196-3	130	197.53	0.07	0.02	0.09	0.07	0.7	0.8		
196-4	130	197.87	0.05*		0.08*		1.2*			
196-5	130	198.11	0.05	0.02	0.02	0.06	0.2	0.8		
200-1	131	125.4	0.19	0.07	0.46	0.23	1.2	1.2		
200-2	131	127.24	0.08	0.03	0.20	0.09	1.2	1.1		
200-4	131	127.59	0.06	0.03	0.23	0.22	2.0	4.0		
200-5	131	127.7	0.09	0.03	0.09	0.04	0.5	0.4		
200-6	131	166.89	0.18	0.04	0.35	0.09	1.0	0.5		
200-7	131	166.96	0.22	0.02	0.47	0.08	1.1	0.3		
200-8	131	167.14	0.16	0.02	0.32	0.05	1.0	0.3		
200-9	131	167.45	0.13	0.02	0.31	0.06	1.3	0.4		

TABLE 4.2 CONT.: Silver Contents of Galena by Electron Microprobe

Sample	Drill hole	Depth	Wt% Ag	St Dev	Wt % Bi	St Dev	At Bi/Ag	St Dev	Wt [1] % Se	St Dev
201-1	131	167.53	0.17	0.01	0.30	0.09	1.0	0.3		
201-2	131	167.58	0.19	0.02	0.37	0.09	1.0	0.4		
201-3	131	167.73	0.20	0.02	0.37	0.09	1.0	0.3		
201-4	131	167.85	0.15	0.03	0.33	0.07	1.2	0.6		
201-5	131	168	0.17	0.02	0.33	0.10	1.0	0.4		
201-6	131	168.4	0.12	0.03	0.26	0.07	1.1	0.6		
BB-101	117	211.6	0.56	0.04	1.18	0.11	1.1	0.2	0.9	0.04
BB-102	124	219.8	0.16	0.06	0.36	0.17	1.1	1.1	0.8	0.09
BB-107	118	158.16	0.82	0.10	1.51	0.23	1.0	0.3	0.8	0.08
BB-104	123	137.97	0.16	0.05	0.19	0.10	0.6	0.5	1.2	0.28
BB-106	126	208.8	0.17	0.04	0.09	0.07	0.3	0.3	0.4	0.11
BB-105	116	223.61	0.02	0.05	0.06	0.05	2.0	2.0	0.1	0.05
BB-103	122	177.7	0.18	0.05	0.31	0.11	1.0	0.7	0.8	0.04
AR48B	AR48B	38.4	0.18	0.04	0.25	0.11	0.7	0.5		
AR79	AR79	174.19	0.12	0.04	0.12	0.08	0.5	0.6		
AR54	AR54	25.1	0.26	0.06	0.34	0.14	0.7	0.5		
AR66	AR66	30.4	0.06	0.03	0.07	0.10	0.6	1.4		
AR89	AR89	239.1	0.12	0.04	0.14	0.09	0.6	0.7		
AR50	AR50	38.63	0.15	0.04	0.34	0.13	1.2	0.9		
AR86	AR86	169.28	0.38	0.05	0.44	0.13	0.6	0.3		
AR78B	AR78B	238.89	0.23	0.10	0.07	0.11	0.2	0.4		
AR18	AR18	75.01	0.40	0.04	0.48	0.08	0.6	0.2		
AR26A	AR26A	32.82	0.18	0.03	0.15	0.06	0.4	0.3		
AR51	AR51	44.2	0.20	0.03	0.19	0.07	0.5	0.3		
AR83	AR83	264.6	0.37	0.04	0.36	0.05	0.5	0.1		
AR92	AR92	143.9	0.37	0.05	0.50	0.07	0.7	0.2		
AR93	AR93	144.36	0.52	0.06	0.72	0.11	0.7	0.2		

Notes: * 1 analysis per sample; *1* Se analyses for BB-samples only.

Ag contents of galena compared to depth for the four drill holes extensively sampled (Figure 4.5) show variability that corresponds to their geologic variability (Chapter 2). AR-0128 from the NW edge of the deposit (Figure 1.6) contains a single (albeit folded) massive sulfide horizon and most galena contains 0.3-0.6 wt% Ag, independent of depth (Figure 4.5A). Drill hole AR-0131 contains two thin horizons and

consistently low Ag (0.1-0.25%) galena (Figure 4.5B). AR-0129 and AR-0130 (Figure 4.5 C,D) contain multiple horizons reflecting varying distances from hangingwall GS contacts (Chapter 2) and possess galena with widely varying silver contents of ~0.1-0.8 and 0.1-0.9 wt%, respectively.

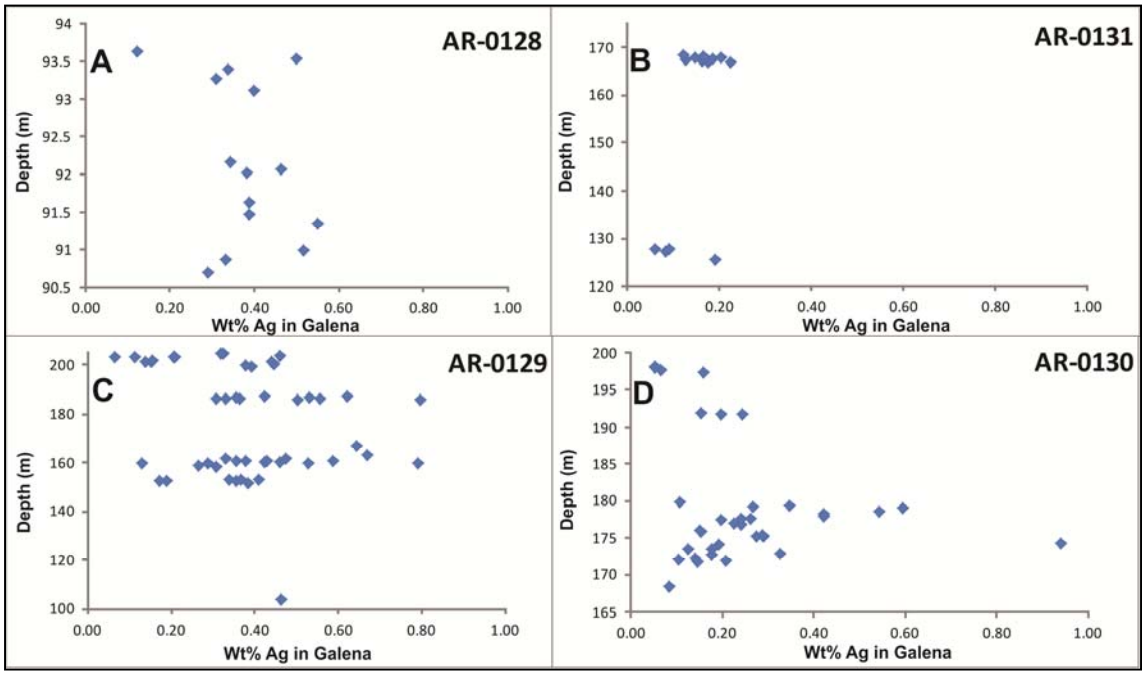

Figure 4.5: Wt% Ag compared to depth (m) in AR-0128, AR-0129, AR-0130, and AR-0131.

Silver contents of galena plotted against mole% FeS in sphalerite for individual samples from the simpler drill holes AR-0128 and AR-0131 (Figure 4.6A) display a generally inverse relationship. That is, galena with higher wt% Ag is present with low-FeS sphalerite, and galena with low wt% Ag is present with high-FeS sphalerite (Figure 4.6A). In contrast, no such relationship is apparent for the more complicated drill holes AR-0129 and AR-0130 (Figure 4.6B).

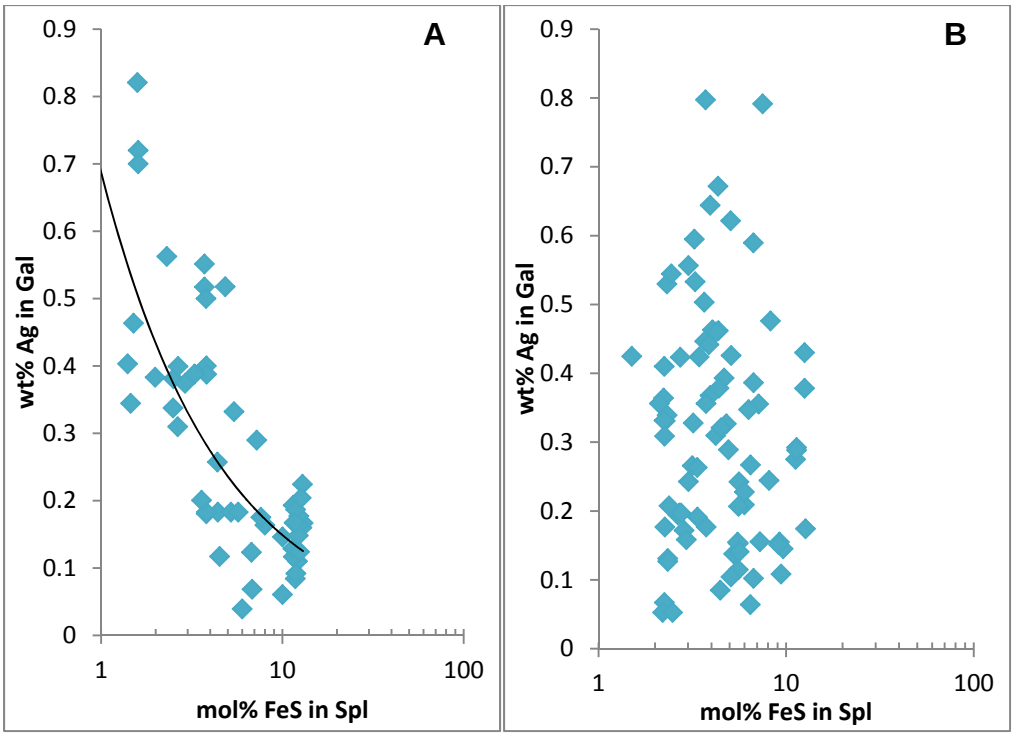

Figure 4.6: Wt% silver in galena vs. mol % Fes in nearby sphalerite. 4.6A = all samples except those from AR-129 and AR-130. 4.6B = samples from AR-129 and AR-130. The former displays an inverse relationship between Ag in galena and FeS in sphalerite; the latter shows no relationship.

4.3 Distribution of Silver in Fahlore

Previous workers have described both tetrahedrite and tennantite [$Cu_{10}(Fe,Zn)_2,As_4S_{13}$] at Arctic (Stevens and Cameron, 1970; Schmidt, 1983). In fact, compositions representing the complete solid solution are present (Table 4.3). No official definitions of the compositional distinctions between the end-members and compositional intermediates are given in the literature. For simplicity, I define:

- 'tennanite' as containing $\geq$ 75% of the tennantite end-member, (i.e., Sb/As+Sb $\leq$ 0.75);
- 'tetradhedrite' as containing > 75% of the tetrahedrite end-member; and
- 'fahlore' as containing Sb/(As+Sb) of 0.25 -0.75% (Figure 4.7).

Based on ~75 samples from Arctic for which I determined Ag contents, the silver contents of Arctic fahlore are much less than the maximum values seen world-wide

(Figure 4.2). However, they display the same Sb-Ag relationship seen elsewhere (Figure 4.7, Figure 4.2). Tennantite contains 0.1-0.6% Ag; 'fahlore' contains 0.1-1.2% Ag, and tetrahedrite contains 0.4-16% Ag (Figure 4.7, Table 4.3).

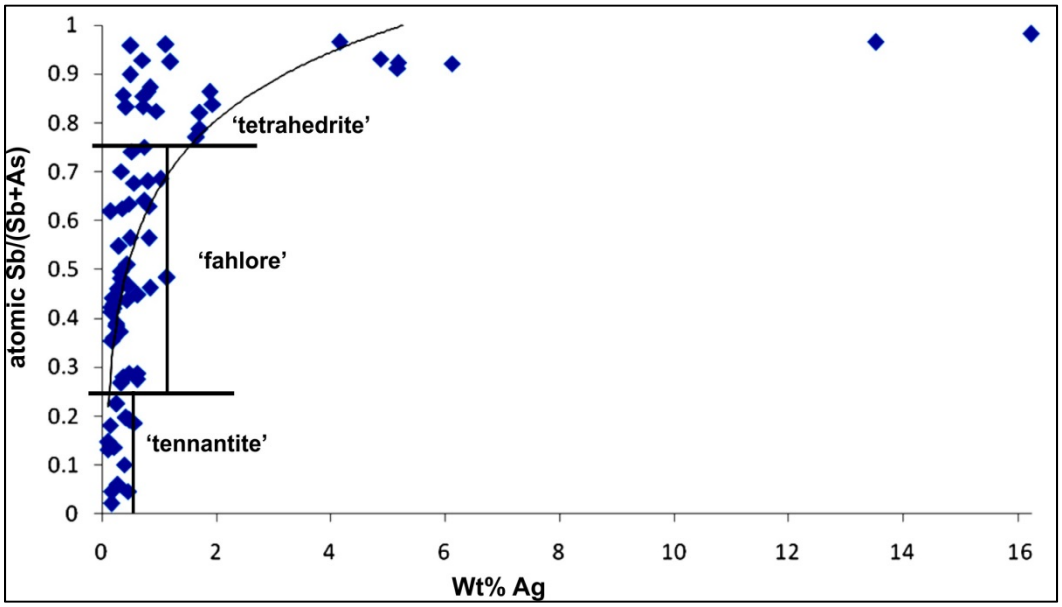

Figure 4.7: Silver contents of Arctic fahlore group minerals shown with their relative Sb contents. Both maximum and minimum wt% Ag increases with increasing relative Sb, i.e., tetrahedrite component.

Table 4.3: Compositions of Fahlore by Electron Microprobe

Sample	Drill hole	Depth	Wt% Ag	St Dev	Wt% As	St Dev	Wt% Sb	St Dev	At Sb/ (As+Sb)	St Dev
197-1	128	90.69	0.8	0.2	2.4	1.0	27.0	1.7	0.9	0.1
197-8	128	92.01	0.1	0.02	15.8	0.5	4.5	0.5	0.2	0.01
197-9	128	92.06	0.1	0.02	16.2	0.3	4.0	0.5	0.1	0.02
198-1	128	92.15	0.1	0.02	15.7	0.2	5.7	0.2	0.2	0.01
198-2	128	92.59	0.3	0.1	11.8	1.1	11.5	1.6	0.4	0.1
198-4	128	93.015	0.2	0.03	11.3	0.5	11.7	0.8	0.4	0.03
198-5	128	93.035	0.4	0.2	8.9	1.5	15.0	2.5	0.5	0.1
198-6	128	93.115	0.8	0.1	6.8	1.0	19.7	1.5	0.6	0.1
198-8	128	93.39	0.3	0.04	9.5	0.5	15.2	0.9	0.5	0.03
198-9	128	93.525	0.2	0.02	7.2	0.04	19.0	0.3	0.6	0.004
178-1	129	200.06	0.2	0.1	11.8	1.6	10.9	2.5	0.4	0.1
176-1	129	152.42	0.8	0.2	8.2	0.8	17.3	1.3	0.6	0.04
180-5	129	152.53	0.3	0.1	5.5	0.6	20.9	1.1	0.7	0.03
180-3	129	152.57	1.9	0.2	2.6	0.0	26.3	0.2	0.9	0.002
180-2	129	152.905	0.3	0.1	13.7	1.1	8.1	1.5	0.3	0.1
180-1	129	152.94	0.4	0.2	13.3	3.0	8.3	3.8	0.3	0.1
182-3	129	157.97	4.2	0.4	0.6	0.0	28.9	0.1	1.0	0.002

TABLE 4.3 CONT.: Compositions of Fahlore by Electron Microprobe

Sample	Drill hole	Depth	Wt% Ag	St Dev	Wt% As	St Dev	Wt% Sb	St Dev	At Sb/ (As+Sb)	St Dev
182-1	129	159.456	0.4	0.1	10.5	1.4	13.3	2.2	0.4	0.1
186-1	129	159.78	1.7	0.3	3.3	0.8	24.7	1.3	0.8	0.04
168-1	129	161.75	0.5	0.1	12.2	2.7	7.9	2.5	0.3	0.1
171-1	129	166.95	0.4	0.1	14.7	1.8	5.8	2.2	0.2	0.1
164-2	129	186.01	0.8	0.5	9.9	4.0	13.9	6.7	0.5	0.2
163-1	129	186.895	0.4	0.1	15.9	2.1	2.9	2.3	0.1	0.1
173-2	129	201.5	0.7	0.1	3.1	2.1	25.7	3.5	0.8	0.1
173-1	129	202.875	0.8	0.2	2.5	2.2	26.4	4.2	0.9	0.1
175-3	129	202.91	1.0	0.4	5.9	0.8	20.8	1.1	0.7	0.04
175-2	129	202.99	0.7	0.2	4.7	2.1	23.0	3.3	0.8	0.1
175-1	129	203.2	0.7	0.1	2.7	1.7	25.8	3.4	0.9	0.1
153-1	129	205.47	13.5	0.6	0.5	0.3	23.0	0.6	1.0	0.02
172-1	129	205.515	0.7	0.3	1.1	0.6	24.1	1.0	0.9	0.04
172-2	129	205.77	0.8	0.2	5.7	2.1	15.8	3.4	0.6	0.1
174-1	129	186.62	0.5	0.0	0.7	0.2	24.6	0.5	1.0	0.01
191-2	130	171.95	0.4	0.0	7.1	0.3	19.2	0.5	0.6	0.01
191-3	130	172.04	0.5	0.1	7.0	1.8	19.6	2.8	0.6	0.1
191-7	130	172.98	0.2	0.1	11.1	3.3	12.7	5.3	0.4	0.2
191-8	130	173.22	0.2	0.0	10.7	3.0	13.7	4.8	0.4	0.2
191-9	130	173.34	0.2	0.1	12.4	3.5	11.0	5.5	0.4	0.2
192-1	130	173.38	0.3	0.0	8.6	0.4	16.8	0.6	0.5	0.02
192-2	130	173.44	0.2	0.1	11.0	2.1	13.0	3.3	0.4	0.1
192-3	130	173.52	0.2	0.1	10.6	2.3	13.1	3.7	0.4	0.1
192-4	130	173.55	0.2	0.0	11.0	1.6	13.1	2.4	0.4	0.1
192-5	130	174.025	0.3	0.0	11.6	0.6	11.8	1.1	0.4	0.03
192-6	130	174.3	0.3	0.0	9.5	0.6	13.2	1.4	0.5	0.01
193-1	130	175.89	0.8	0.1	6.1	2.4	21.0	3.6	0.7	0.1
193-2	130	176	0.9	0.1	3.3	0.9	25.5	1.4	0.8	0.1
193-6	130	177.57	0.6	0.1	6.1	1.1	20.6	1.7	0.7	0.1
193-8	130	177.695	0.4	0.1	3.1	0.3	25.6	0.5	0.8	0.02
194-1 Tet	130	178.26	1.1	0.2	9.6	0.3	14.6	0.4	0.5	0.01
194-1 Tenn	130	178.26	0.6	0.2	15.2	0.9	5.7	1.7	0.2	0.1
194-3	130	178.51	0.2	0.0	16.2	1.7	4.2	2.7	0.1	0.1
194-4	130	178.96	0.6	0.1	13.3	0.5	8.3	0.6	0.3	0.02
194-5	130	179.14	0.5	0.1	4.9	1.0	22.8	1.6	0.7	0.1
195-1	130	191.66	0.5	0.1	8.3	1.1	17.5	1.8	0.6	0.1

TABLE 4.3 CONT.: Compositions of Fahlore by Electron Microprobe

Sample	Drill hole	Depth	Wt% Ag	St Dev	Wt% As	St Dev	Wt% Sb	St Dev	At Sb/ (As+Sb)	St Dev
195-3	130	191.96	0.5	0.2	1.9	0.5	27.6	0.8	0.9	0.03
196-2	130	197.48	0.2	0.0	18.4	0.3	0.7	0.0	0.0	0.002
196-3	130	197.53	0.3	0.1	9.6	2.7	14.2	2.6	0.5	0.1
196-5	130	198.11	0.5	0.1	10.0	2.0	14.2	2.9	0.5	0.1
196-6	130	198.24	0.2	0.0	18.4	0.4	1.4	0.4	0.0	0.01
200-2	131	127.24	1.9	0.0	3.1	0.4	25.9	0.6	0.8	0.02
200-3	131	127.42	1.1	0.2	0.7	0.1	29.2	1.3	1.0	0.003
200-4	131	127.59	0.4	0.1	2.7	1.0	26.3	1.4	0.9	0.1
200-8	131	167.14	4.9	0.7	1.3	0.2	28.1	0.4	0.9	0.01
201-2	131	167.58	5.2	0.4	1.6	0.4	27.6	0.9	0.9	0.02
201-4	131	167.85	5.2	0.1	1.4	0.1	27.7	0.0	0.9	0.01
201-5	131	168	1.2	0.0	1.4	0.3	28.6	0.3	0.9	0.01
201-6	131	168.4	6.1	0.8	1.4	0.2	27.0	2.0	0.9	0.01
BB-101*	117	211.6	0.6	0.07	13.6	0.8	8.9	1.2	0.3	0.04
BB-102*	124	219.8	1.7	0.3	4.3	1.4	22.9	2.6	0.8	0.1
BB-107*	118	158.16	0.5	0.1	19.3	0.3	1.6	0.1	0.1	0.003
BB-106	126	208.8	16.0	0.7	NA	NA	NA	NA		
AR48 B-Tet*	AR48	38.4	1.7	0.2	3.8	1.7	22.8	2.2	0.8	0.1
AR48 B-Tenn*	AR48	38.4	0.5	0.1	14.8	0.9	5.8	1.4	0.2	0.03
AR79*	AR79	174.19	0.6	0.1	9.81	1.4	13.0	2.0	0.5	0.02
AR54*	AR54	25.1	0.3	0.2	14.1	0.4	6.7	0.5	0.2	0.02
AR51*	AR51	44.2	0.3	0.1	13.4	2.3	1.4	0.4	0.06	0.05

Notes:*As and Sb contents are semi quantitative based on multiple EDS analyses. Uncertainties ~$\pm$ 5%. NA = not analyzed.

Ag-contents of fahlore compared to depth for the four extensively-studied drill holes (Figure 4.8) show a simple pattern for AR-0131 and more complex patterns for the others. AR-0131 simply contains tetrahedrite; the others contain a mixture of tennantite, tetrahedrite, and fahlore.

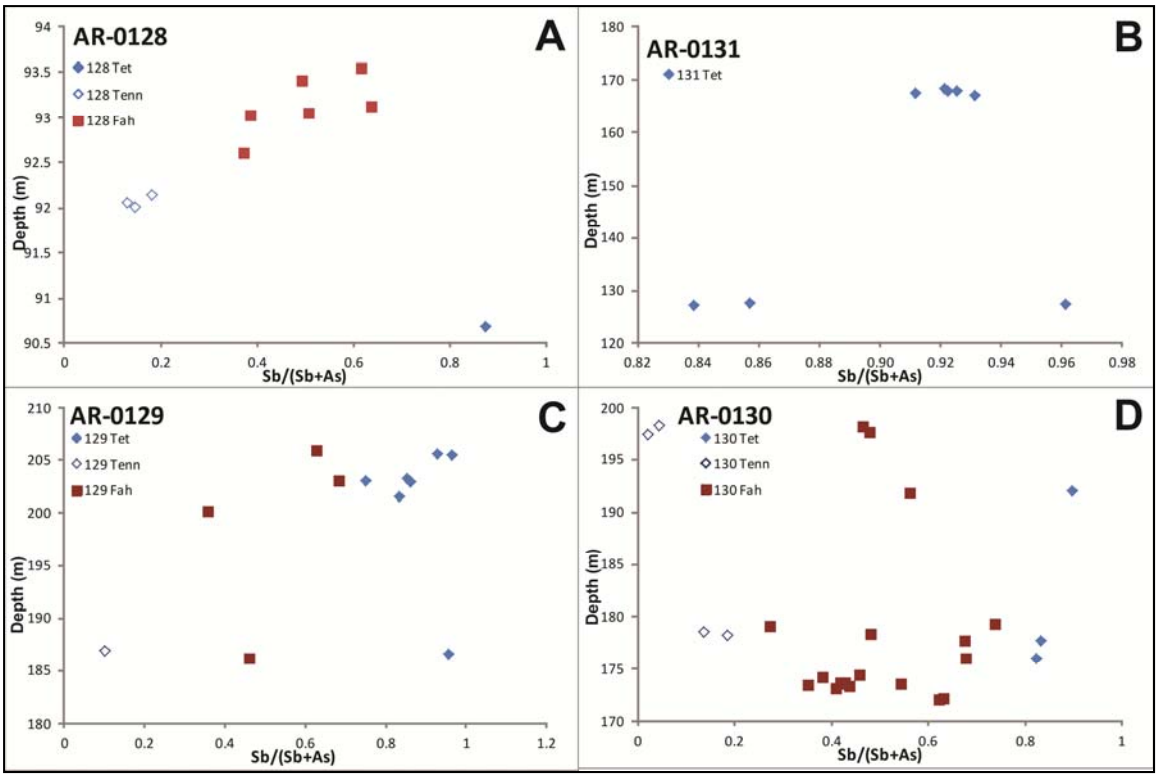

Figure 4.8: Atomic Sb/(Sb+As) vs. depth in AR-0128, AR-0129, AR-0130, and AR-0131.

Fahlore composition—expressed as atomic Sb/(Sb+As)—is strongly correlated ($R^2 = 0.80$, Figure 4.9) with mol % FeS in the associated sphalerite at Arctic. That is, low-Sb-fahlore (Sb/(Sb+As < 0.5) and tennantite are exclusively associated with sphalerite containing < 4 mole % FeS (Figure 4.9). Conversely, sphalerite with > 6 mol% FeS is exclusively associated with high-Sb fahlore and tetrahedrite (Figure 4.9). The mineral association in most cases (Chapter 3) is tetrahedrite+arsenopyrite+high-Fe sphalerite vs. tennantite+pyrite+low-Fe sphalerite. Given that elevated Ag is restricted to tetrahedrite (Figure 4.7), it's not surprising that high-Ag tetrahedrite only occurs with high-Fe sphalerite (Figure 4.10).

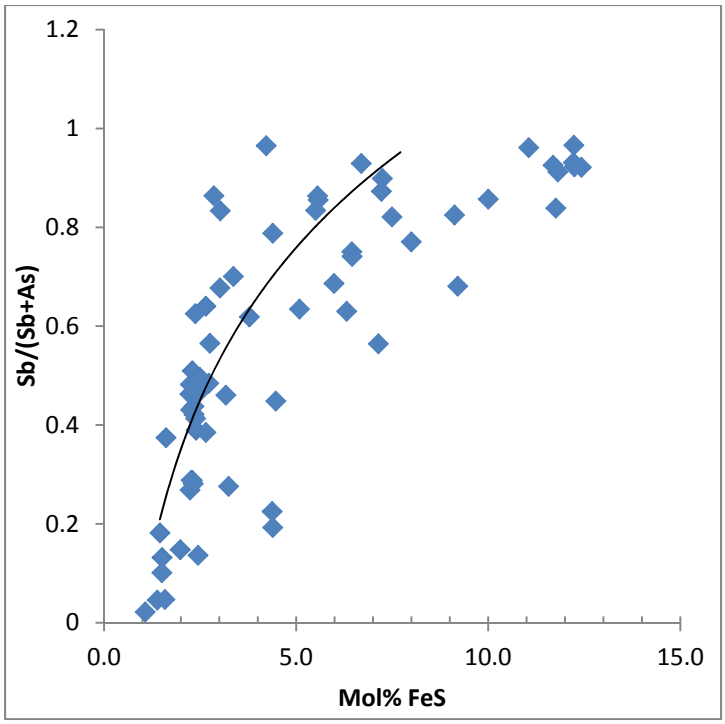

Figure 4.9: Atomic Sb/(Sb+As) in fahlore vs. mol% Fes in nearby sphalerite, showing strong correlation.

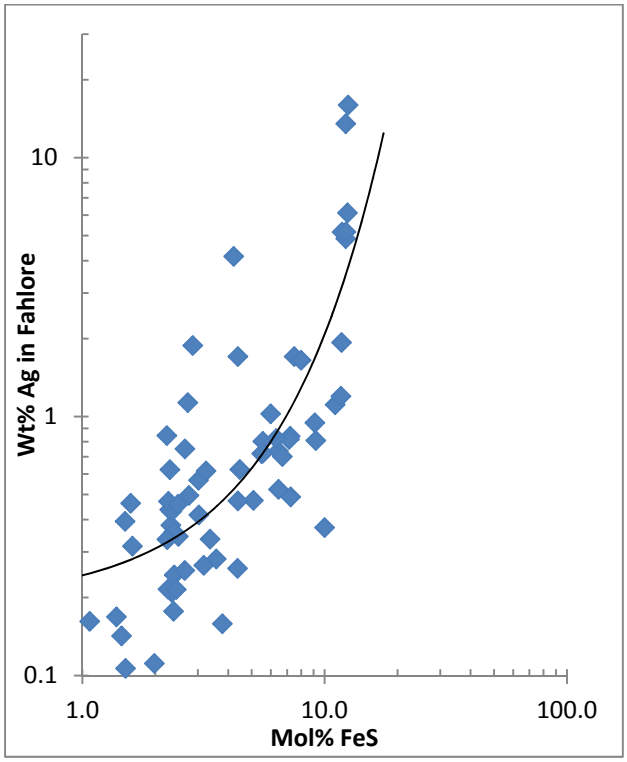

Figure 4.10: Wt% Ag in fahlore vs. mol % Fes in nearby sphalerite, showing a strong correlation between the two.

4.4 Distribution of Silver in Bornite

Limited analyses of bornite (Table 4.4) indicate 0.3-0.44 wt% Ag but show considerable within-grain variation, particularly for those hosted by porphyroblastic pyrite (BB102, 108). Bornite was not identified in the other samples examined, although it is a moderately common mineral in the SE part of the deposit. Bi and Se were below detection (Table 4.4) in all analyses. Of the samples examined, only BB104 contains sufficient bornite for that mineral to contribute appreciably towards the measured silver budget.

Table 4.4: Trace Element Contents of Bornite at Arctic

Sample	Drill hole	Wt% Ag	St Dev	Wt% Bi	St Dev	Wt% Se	St Dev
BB102	124	0.3	0.2	0.02	0.08	0.01	0.03
BB108	117w	0.4	0.1	0.09	0.05	0.03	0.03
BB104	123	0.4	0.1	0.05	0.06	0.02	0.02

4.5 Other Minerals

Table 4.5 gives Ag, Bi, and Se concentrations for various Arctic ore minerals. None of them contain concentrations of these elements above the detection limits. In contrast, I found electrum, with a composition of 72% Au, 28% Ag in one sample, and a tiny amount of Ag-bearing wittichenite (Cu_3BiS_3) in another. I found bismuthenite (Bi_2S_3) in three samples. All bismuthenite analyses gave 1-4% Sb and Ag below detection.

Table 4.5: Silver, Bismuth and Selenium Contents of Arctic Deposit Minerals

Mineral	Sample	Wt%Ag	St Dev	Wt%Bi	St Dev	Wt%Se	St Dev
pyrrhotite	BB106	0.00	0.02	0.0	0.08	-0.01	0.04
chalcopyrite	BB104	0.00	0.02	0.0	0.06	0.01	0.02
sphalerite	BB106	0.00	0.02	0.0	0.08	0.01	0.05
sphalerite	BB108	0.00	0.02	0.0	0.07	0.01	0.05
arsenopyrite	BB106	0.00	0.02	0.0	0.08	0.02	0.04
magnetite	BB105	0.00	0.01	0.0	0.07	0.00	0.03

4.6 Distribution of Ag Between Co-Existing Phases

Figure 4.11 shows the silver content of fahlore plotted against the silver content of the nearby galena, showing a generally inverse relationship. That is, the most Ag-rich galena is associated with Ag-poor fahlore and Ag-rich tetrahedrite is associated with Ag-poor galena. Rather than seeing Ag enrichment in both, a sample typically shows Ag enrichment in one or the other. Similarly, sample BB104 contains bornite with 0.44% Ag and coexisting galena with 0.13% Ag (Tables 4.2, 4.4).

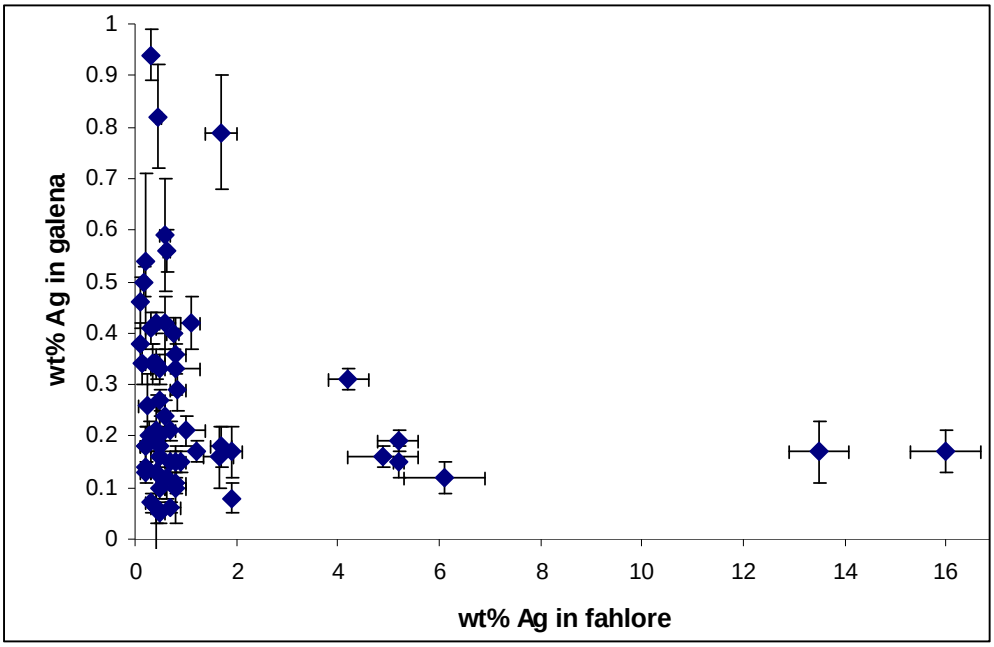

Figure 4.11: Wt% Ag in fahlore vs. wt% Ag in galena from the same sample, showing an inverse relationship between the two.

4.7 Bulk Distribution of Silver

I made XRF pressed pellets for 28 samples from which polished thin sections had been prepared, using techniques described in Chapter 1. In all cases, the sample that was pulverized was no more than 11g and represented the same material from which mineral analyses were determined by microprobe. Table 4.6 gives the results of these analyses and shows a wide variation in whole rock Ag, Pb, Bi, Sb, and As concentrations, consistent with wide variations in galena and fahlore abundances as seen in polished

sections. The samples ranged from > 10% to < 0.5% galena, from >3% to <0.01% fahlore, and from none to >4% arsenopyrite. That is, these concentrations illustrate the extreme heterogeneity of ore mineral abundances in small (10 cm^3) massive sulfide samples. Silver contents range from > 800 to < 100 ppm. These concentrations are not representative of 0.5- 1 meter ore intervals, but do represent the wide variations in metal concentrations present within the massive sulfide mineralization in general.

Table 4.6: Wt% Elemental Concentrations in XRF Pressed Pellets at Arctic

Sample	S	Pb	Zn	Fe	As	Ag	Bi	Sb	Cu
153-1	39.3	14.0	28.1	28.0	3.27	0.08	0.04	0.11	6.6
165-2	43.3	7.3	25.4	27.1	0.05	0.04	0.07	0.01	5.3
166-2	50.8	3.7	8.2	43.0	0.06	0.03	0.07	0.01	14.7
167-1	46.6	6.6	27.1	29.6	0.00	0.04	0.08	0.02	9.4
173-1	14.8	1.8	5.5	12.1	0.07	0.02	0.01	0.06	5.3
175-3	43.6	7.3	20.9	30.4	0.10	0.03	0.04	0.25	9.3
180-3	29.6	2.5	8.4	20.7	0.15	0.02	0.01	0.01	1.01
191-3	14.8	4.3	7.7	15.2	0.19	0.02	0.02	0.43	1.5
193-9	24.6	2.4	16.8	17.1	1.57	0.01	0.03	0.10	2.2
194-1	44.8	2.4	11.3	38.4	0.52	0.02	0.03	0.06	8.5
195-1	37.2	6.4	10.5	25.9	0.19	0.03	0.05	0.05	0.7
197-6	48.1	5.8	27.5	32.1	0.05	0.03	0.05	0.00	1.5
198-5	24.5	0.2	8.5	18.3	0.02	0.01	0.02	0.01	4.2
198-6	46.9	7.5	24.5	34.0	0.08	0.03	0.06	0.14	0.6
198-9	36.5	3.3	12.7	25.5	0.04	0.02	0.04	0.01	1.0
200-2	36.2	10.4	21.1	26.7	2.48	0.02	0.03	0.05	3.6
200-7	40.6	10.4	40.0	19.4	0.97	0.03	0.05	0.02	3.9
200-8	43.1	11.7	35.9	25.2	2.19	0.04	0.06	0.13	5.4
201-2	45.7	16.5	36.2	25.6	0.41	0.05	0.08	0.10	2.1
201-4	35.1	9.3	30.5	21.3	0.58	0.04	0.04	0.11	4.8
BB-101	17.0	1.58	7.04	10.6	2.25	0.06	0.08	0.77	12.0
BB-102	26.4	6.05	26.3	19.3	0.79	0.09	0.05	1.00	6.6
BB-103	22.9	4.10	20.3	14.6	0.12	0.02	0.03	0.01	11.6
BB-104	20.7	0.40	11.7	18.9	0.02	0.02	0.01	0.01	8.7
BB-105	13.8	1.78	2.6	10.1	2.59	0.02	0.01	0.18	1.4
BB-106	12.8	7.98	19.8	5.0	0.08	0.02	0.03	0.03	1.8
BB-107	25.9	2.13	10.5	23.9	3.19	0.06	0.10	0.20	14.6
BB-108	20.1	3.34	15.6	14.6	0.01	0.02	0.04	0.00	10.8

I calculated the Ag contributions of galena, fahlore, and bornite (if present) for the total Ag content of each sample by combining microprobe and XRF data (Table 4.7,

Appendix 5). My basic assumption was that essentially all of the Pb and Sb in the rock were present in galena and fahlore, respectively, and that these elements could be used as proxies for abundances of the ore minerals. I used the microprobe Ag content of galena (assuming constant Pb content of galena) combined with the % Pb in the rock to determine the amount of Ag contributed by galena. I used the microprobe Ag and Sb contents of fahlore combined with the % Sb in the rock to determine the amount of Ag in the sample contributed by fahlore. For the one sample (BB104) with appreciable bornite, I combined the microprobe Ag content of bornite with the estimated % bornite in thin section (visual inspection) to determine the amount of Ag contributed by bornite.

The match between calculated and measured Ag in the 28 samples (Table 4.7) is generally good to very good; all samples agree within 10%. Sample BB104 is the only one with appreciable bornite and the bulk of Ag in that sample must be contained in that mineral.

Table 4.7: Calculated Ag Budget for Samples by Combination of XRF and Microprobe

Sample	Drill hole	Wt% Ag in Gal	XRF %Pb	ppm Ag calc'd from gal	Wt% Ag in Tet	Wt% Sb in Tet	XRF %Sb	ppm Ag calc'd from fahl	calc'd Total Ag	XRF Total Ag	%Ag due to gal	%Ag due to fah	XRF Bi/Ag
153-1	129	0.17	14.0	243	12.5	23.0	0.11	625	867	788	28	72	0.3
165-2	129	0.56	7.3	440			**0.01**	**3***	443	431	100	0	0.9
166-2	129	0.80	3.7	339			**0.01**	**3***	343	331	99	1	1.0
167-1	129	0.69	6.6	451			**0.02**	**5***	456	412	99	1	1.0
173-1	129	0.13	1.84	28	1.5	27.5	0.19	104	131	135	21.0	79.0	0.3
175-3	129	0.21	7.3	176	1.0	20.9	0.25	124	300	320	59	41	0.6
180-3	129	0.22	2.47	63	2.2	26.0	0.02	20	83	100	75.8	24.2	0.7
191-3	130	0.11	4.3	55	0.6	17.0	*0.43*	155	210	227	26	74	0.5
193-9	130	0.39	2.4	110			**0.10**	**39***	149	149	74	26	1.1
194-1	130	0.42	2.4	116	0.6	5.7	0.06	59	175	177	66	34	0.9
195-1	130	0.24	6.81	189	0.6	19.0	0.07	22	210	233	89.7	10.3	1.1
197-6	128	0.39	5.8	263			**0.00**	**1***	264	263	100	0	0.9
198-5	128	1.1	0.30	38	0.8	15.0	0.02	12	50	52	76.5	23.5	3.1
198-6	128	0.34	7.5	293	0.8	19.5	0.14	55	348	319	84	16	1.0
198-9	128	0.50	3.3	190	0.2	19.0	0.01	1	191	222	100	0	0.8
200-2	131	0.09	10.4	108	1.9	25.9	0.05	39	147	152	73	27	1.1
200-7	131	0.24	10.4	288			**0.02**	**24***	312	307	92	8	0.9
200-8	131	0.18	11.7	242	3.9	27.4	0.13	185	427	363	44	56	0.9
201-2	131	0.16	16.5	305	5.0	27.5	0.10	187	492	459	62	38	0.9
201-4	131	0.16	9.3	172	5.2	27.7	0.11	211	383	401	45	55	0.5
BB-101	117	0.56	1.6	106	0.6	8.9	0.77	414	520	572	20	80	0.7
BB-102	124	0.16	6.1	104	1.65	22.9	1.00	494	597	673	17	83	0.3
BB-103	122	0.18	4.1	93			0.01	0	93	140	67	0	1.2
BB-104	**123**	**0.16**	**0.4**	**8**	**Bn➔ 220 ppm**		**0.01**	**0**	**228**	**208**	**3**	0	**0.2**
BB-105	116	0.02	1.8	6			0.18	164	170	182	4	96	0.2
BB-106	126	0.17	7.8	135	16	27	0.02	114	249	236	54	46	0.6
BB-107	118	0.82	2.1	198	0.46	1.56	0.20	415	613	570	32	68	0.9
BB-108	117w	0.34	3.4	139			0.001		154	180	91	0	1.1

Notes:*Fahlore or Galena not analyzed by microprobe. 'Stand in' minerals were created for this study.

Figure 4.12 shows the measured Ag compared to Ag calculated from mineral compositions as described previously. If all of the silver is present in some combination of galena, fahlore, or bornite, a 1:1 correlation would be expected between measured Ag and calculated Ag. This relationship is true (within analytical error) indicating the bulk of the Ag at Arctic is hosted by a combination galena, fahlore, and bornite. (Dotted lines on the chart indicate ± 10% error.)

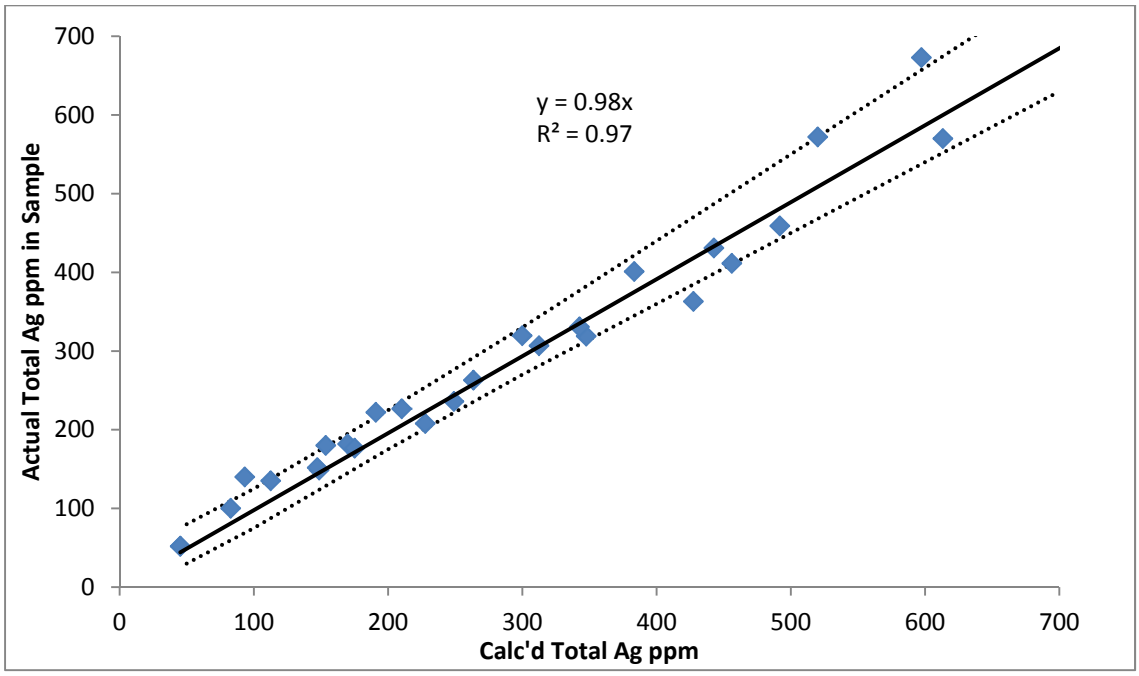

Figure 4.12: Calculated Ag due to galena, fahlore, and (or) bornite vs. measured Ag for Arctic Deposit samples. Calculated values are from Table 4.7. Dotted lines on the chart indicate estimated combined analytical errors of + 10%.

The calculated proportion of Ag in a sample due to galena varies tremendously—both between and within drill holes (Table 4.7). However, in the majority of cases, galena appears to be the dominant Ag-carrier. The spatial pattern (Figure 4.13) is even more unclear, largely due to limited samples and extreme irregularity. Taken at face value, however, galena appears to account for a larger proportion (2/3-3/4) of the silver in the central and NW parts of the deposit, whereas galena is less important in the SE part of the deposit.

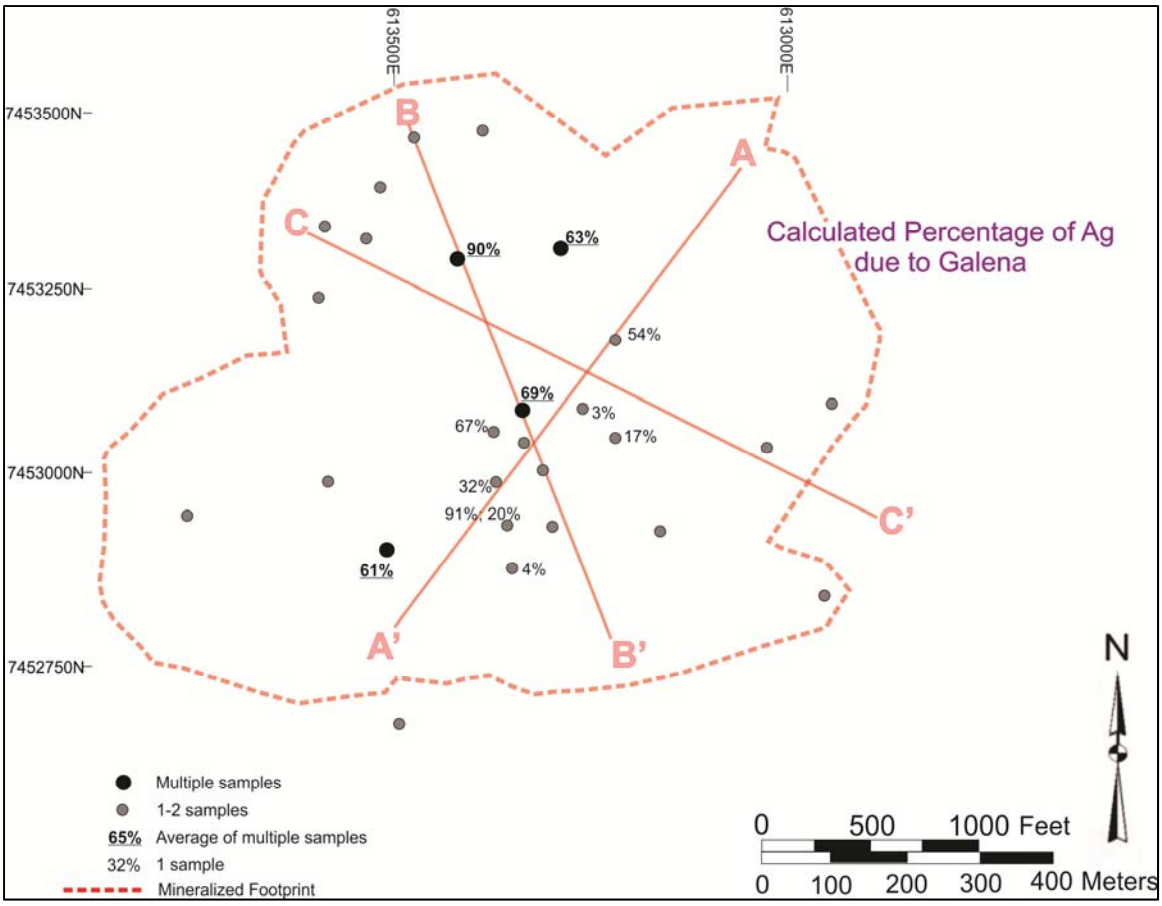

Figure 4.13: Calculated percentage of Ag due to galena for samples analyzed by XRF. At least 4 samples are averaged from the drill holes shown in black; for the others only 1 sample was measured.

4.8 Relations Between Bulk Ag and Mineralogic Ag

Figure 4.14 shows the calculated proportion of Ag hosted in galena compared to total measured Ag. The proportion of Ag due to galena in a sample varies tremendously—from nearly zero to nearly 100%—and shows no simple relationship to the total Ag content of the sample. However, for samples with unusually high (> 450 ppm) Ag, the bulk of the Ag is not contained in galena. That is, in the unusual samples with very high silver grades, the bulk of the Ag is likely present in tetrahedrite or bornite.

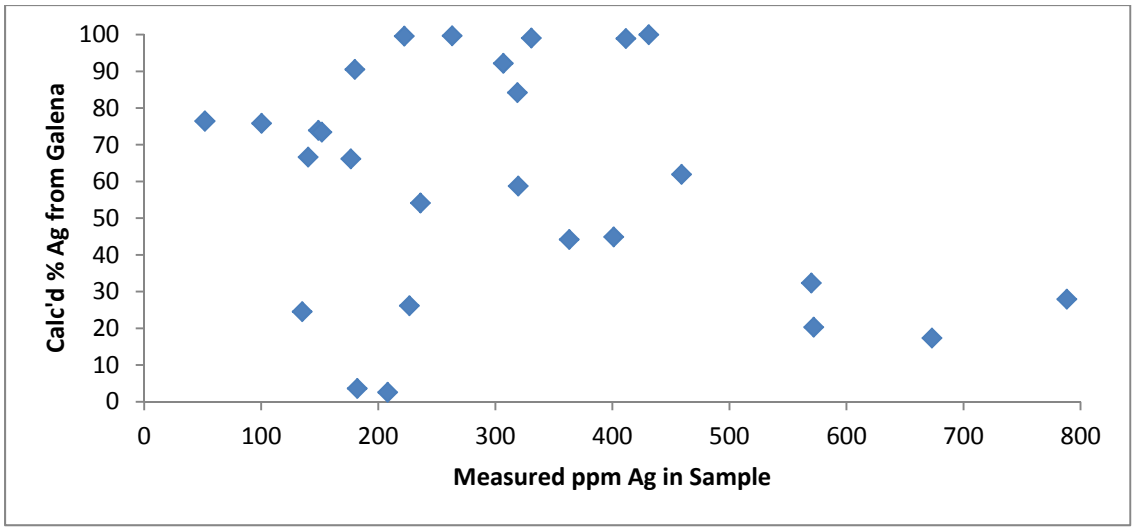

Figure 4.14: Measured total Ag vs. calculated % Ag derived from galena for Arctic samples.

Because Ag requires Bi to substitute into galena, an atomic Bi/Ag ratio of 1 is expected if all of the Ag is hosted in galena. Figure 4.15 shows that all but one of the samples exhibit (within analytical uncertainty) atomic Bi/Ag of 1 or less. The anomalous sample contains bismuthenite, confirmed by microprobe. For the other samples, % of the Ag in the rock due to galena is broadly proportional to the atomic Bi/Ag ratio, as indicated by the black line on the graph.

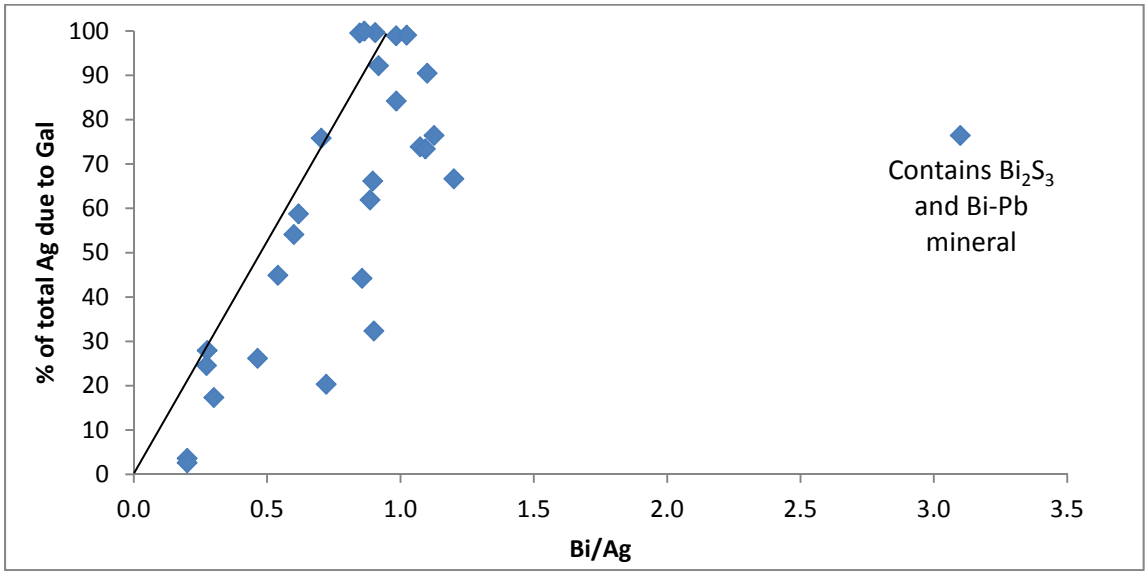

Figure 4.15: Atomic Bi/Ag from bulk XRF vs. calculated % of total Ag due to galena. If all Ag was due to galena and no extra Bi was present, a Bi/Ag of 1.0 would be expected.

Comparison between the Ag content of galena and the total Ag content of the sample (Figure 4.16) shows a broadly consistent ratio between the two. That is, for many of the samples, higher Ag grades are due to higher-Ag galena. However, several samples contain elevated Ag despite possessing low-Ag galena, indicating that a different mineral (tetrahedrite) is causing the anomalously high Ag grades (Figure 4.16). In any event, the relation between Ag concentration in galena and Ag concentration in rock is not straightforward.

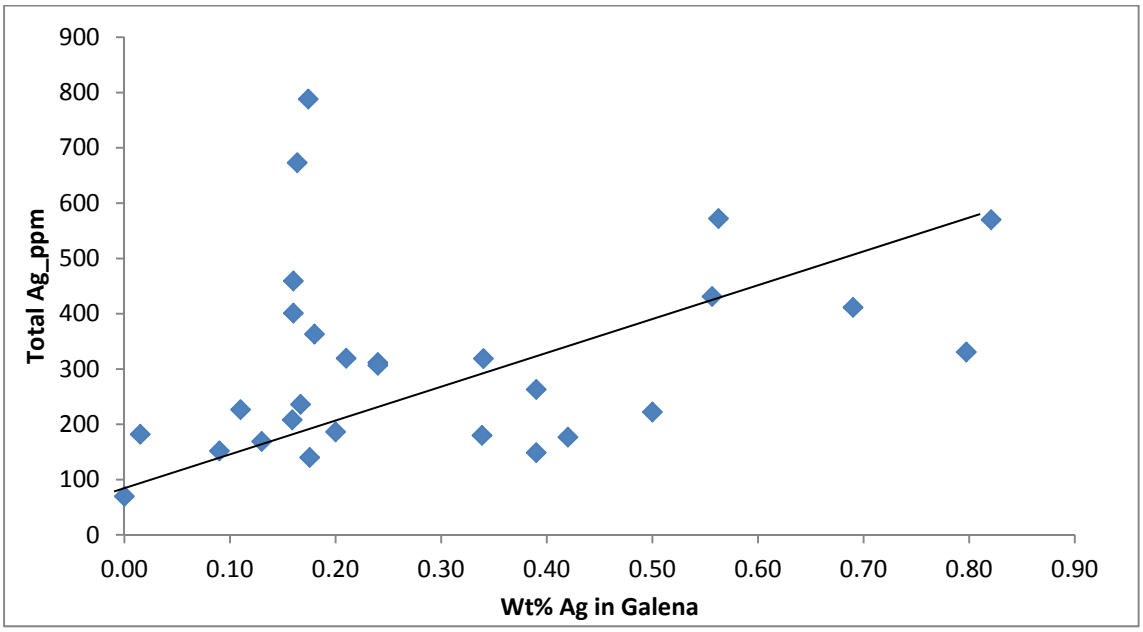

Figure 4.16: Microprobe wt% Ag in galena vs. XRF total Ag in the sample, showing a broad proportionality.

The lack of direct correlation between Ag in galena and bulk Ag in the rock is due, in part, to the variable Pb contents of the samples, as illustrated in Figure 4.17. Oddly, Ag concentration in galena shows a weak negative correlation with %Pb in the rock: the less galena present, the greater the Ag content of the galena. This is especially true for the highest-Ag galena samples and samples with the highest Pb concentrations.

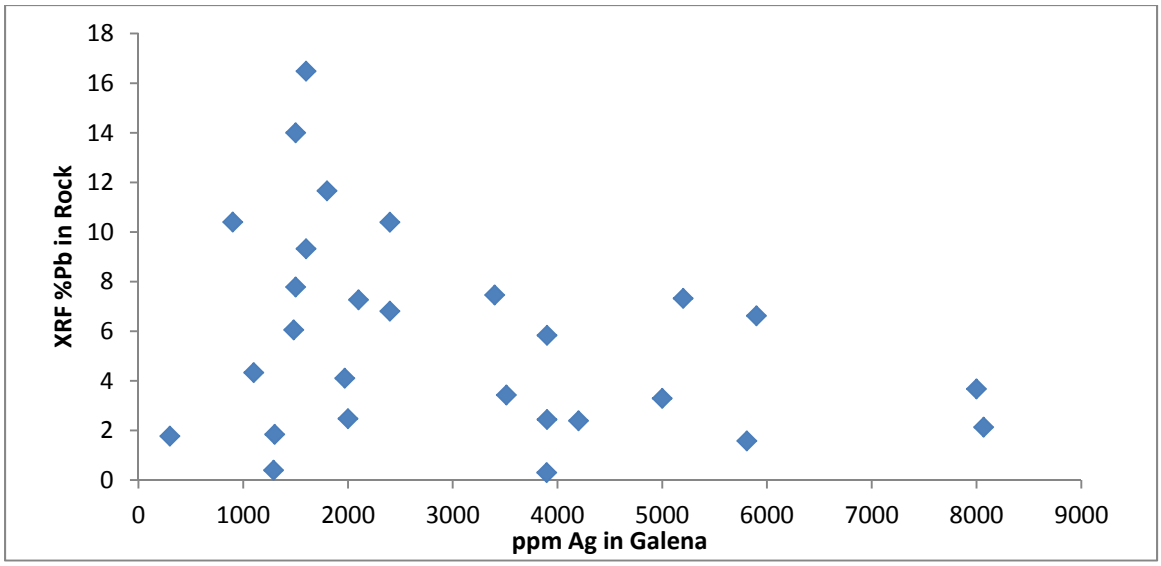

Figure 4.17: Ag concentration in galena vs. bulk Pb content of the sample, showing inverse correlation.

Similarly, the Ag content of tetrahedrite drops with increasing Sb in the rock (Figure 4.18). This is particularly demonstrated by the extremes; the two samples with the highest Ag-tetrahedrite are from samples with < 0.1% Sb, and the three samples with > 0.4% Sb contain < 2% Ag in the tetrahedrite (Figure 4.18).

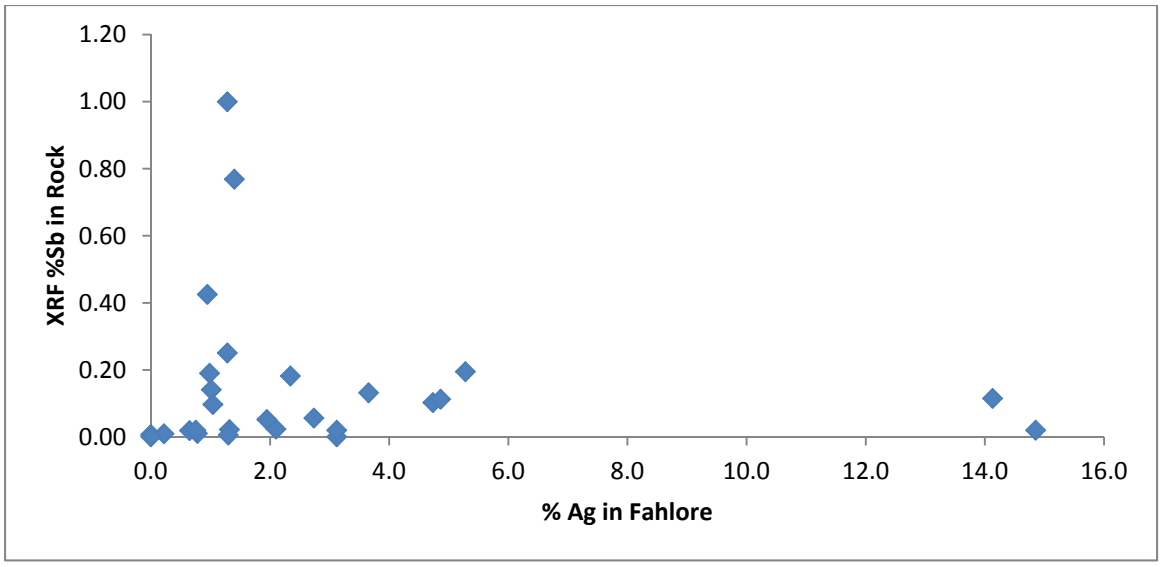

Figure 4.18: Ag concentration in fahlore vs. bulk Sb content of the rock, showing an inverse relationship.

4.9 Discussion

Based on the several thousand microprobe analyses and 28 accompanying XRF analyses, it is clear that the bulk of Ag at Arctic is carried in galena, fahlore and locally in bornite. No significant Ag was detected in the other ore minerals (sphalerite, pyrite, chalcopyrite, magnetite, and arsenopyrite) and their Ag contribution is negligible (Table 4.5). The degree to which galena or fahlore carries the Ag depends both on the mineral abundance and mineral composition. Bornite is restricted to the SE part of the deposit (Chapters 1, 3) and—based on one bornite-rich sample—is a preferred Ag host in that region.

Ag^{+} requires a coupled substitution with either Bi^{3+} or Sb^{3+} to enter galena; the absence of Sb in Arctic galena (Appendix 1) and the 1:1 atomic ratio of Bi:Ag in galena (Figure 4.3) indicates that Bi is the limiting factor. I noted Bi phases including bismuthenite and wittechenite present in trace amounts in 4 samples. That no one has previously reported such phases indicates that these minerals are rare. In all but one case (Figure 4.15), my analyses show atomic Bi:Ag (within analytical error) is ≤ 1. That is, usually there is just barely enough or insufficient Bi present to allow for all the Ag to substitute into galena. Where the Bi:Ag ratio in the bulk sample is low, the proportion of Ag due to galena is also low (Figure 4.15). Exactly what controls the Bi:Ag ratio in a given specimen of massive sulfide is unknown and presumably reflects both the original Bi:Ag ratio and migration of both Ag and Bi during metamorphism. However, since Ag-bearing galena does not occur at the Kuroko deposits in Japan, a redistribution of Bi and Ag during galena recrystallization must have taken place.

Fahlore is also a major Ag carrier at Arctic, but only the Sb-rich variety (tetrahedrite) contains appreciable Ag (Figure 4.7), a phenomena seen world-wide. Based on my XRF analyses (Table 4.7) and data compiled from Arctic multi-element analyses (Table 4.8), the As:Sb ratio for Arctic massive sulfide is about 5:1. Given that Sb weighs nearly twice as much as As, the atomic ratio is about 8:1. Since Sb is essentially restricted to fahlore at Arctic (whereas As occurs both in tennantite/As-rich fahlore and arsenopyrite)

the Sb content of fahlore depends on the amount of As present as arsenopyrite. The expected reaction is:

$$Cu_{9.5}Ag_{0.5}Fe_2As_3SbS_{13} + 9FeS_2 \rightarrow (1/4)Cu_8Ag_2Fe_2Sb_4S_{13} + 7.5CuFeS_2 + 3FeAsS + (\sim 5)S_2$$

As-rich Fahlore + Pyrite ➔ Ag-rich Tetrahedrite + Chalcopyrite + Arsenopyrite + excess S

That is, Ag in the As-rich tennantite is concentrated into tetrahedrite by removing the excess As which concentrates both Sb and Ag in the new mineral. At the same time, this Sb-mineral can potentially react with surrounding galena and extract Ag which should cause precipitation of excess Bi as bismuthenite (Bi_2S_3).

Table 4.8: Estimated Average Metal Contents of the Arctic Deposit

Element	%Pb	Ag ppm	Bi ppm	As ppm	Sb ppm
Units	0.94	60	100	1650	340

In Chapter 3, I showed that arsenopyrite is only stable at low fS_2, associated with moderate-to high Fe sphalerite (Figures 3.4, 3.6, 3.14). Consequently, high-Fe sphalerite is present with fahlore that contains both high Sb (Figure 4.9) and high Ag (Figure 4.10). The bulk of the fahlore at Arctic, however, is both low in Sb (As>Sb), and low in Ag (Table 4.4). In other words, the degree to which Ag is partitioned into fahlore depends on the fahlore composition, which in turn depends on the degree to which As is partitioned into arsenopyrite (or partitioned between fahlore/tennantite and arsenopyrite). As demonstrated in Chapter 3, the presence of arsenopyrite depends on the fS_2. The data demonstrate that high Ag-Sb-tetrahedrite is preferentially associated with pyrrhotite, high-Fe sphalerite, which is generally proximal to carbonaceous grey schist (Chapter 3).

The Ag contents of galena are generally antithetic to those of fahlore; higher Ag-galena is present with lower-Ag fahlore. Because the fahlore composition is related to fS_2 (and reflected in sphalerite FeS content), in a broad way, so is the Ag content of galena. This pattern—higher Ag in galena associated with low-Fe sphalerite—is true for about half the samples (Figure 4.6A). However, it is not true for samples from drill holes

AR-0129 and -0130 (Figure 4.6B), presumably due to the high degree of folding and interfingering of hangingwall (GS) and footwall lithologies (Chapter 2).

A final complication is that the silver carriers galena and tetrahedrite vary tremendously in abundance as suggested by the XRF abundances of Pb and Sb (Table 4.6). An interesting, but odd observation is that in many cases the more abundant the silver-carrying mineral, the lower its silver content. This is true for both galena (Figure 4.17) and tetrahedrite (Figure 4.18). That is, if the Ag content in galena is largely dictated by the amount of available Bi, then the greater the abundance of Pb in that sample, the more that the Ag is diluted in the host mineral—and vice versa. Consequently, a massive sulfide interval rich in galena and (or) tetrahedrite is not necessarily rich in silver. That is, Ag will be more greatly distributed (diluted) within the host mineral when a greater abundance of either galena or tetrahedrite is present.

Based on the drill holes with multiple XRF samples (Table 4.7, Figure 4.13) on average approximately 2/3 of the Ag at Arctic is contained in galena. A grand average of my galena data (Table 4.2) contains about 0.35% Ag. With an average grade of 0.94% Pb (Table 4.8, Chapter 1) such average galena (86.6% Pb) would cause the average ore to contain approximately 40 ppm Ag (3500 x 0.94/86.6). This is 2/3 of the observed average Ag grade (Chapter 1) of 59.6 ppm. Such a value is also suggested by the average Bi:Ag ratio of 1.7 (Table 4.8), which gives an atomic ratio of 0.86. There simply isn't enough Bi at Arctic to allow all the Ag to enter galena. Although the average Sb content of the Arctic deposit is low (Table 4.8), because tetrahedrite can contain abundant Ag, it is capable of carrying the bulk of the other 1/3 of the silver. The main reason why more Ag isn't contained in the fahlore is because of the difficulty in substituting Ag into the As-end member (tennantite), and—in the absence of arsenopyrite—the abundance of such.

4.10 Conclusions

Unmetamorphosed Kuroko deposits contain Ag largely as Ag-Cu sulfides and lack Ag-bearing galena. In contrast, approximately 2/3 of the silver at Arctic is present in galena that contains 0.02-0.94 wt% Ag. Substitution of Ag into galena requires simultaneous Bi introduction, and one of the constraints on this substitution is the availability of Bi in the ore. The other 1/3 of the Ag is mostly present in Sb-rich fahlore (tetrahedrite) with some in bornite. Because the Sb content of fahlore rises as As is partitioned into arsenopyrite, the Ag content of Arctic fahlore varies with the local fS_2-fO_2 conditions during metamorphism. As bornite+pyrite requires high fS_2 and arsenopyrite requires low fS_2, the distribution of Ag between bornite, galena, and fahlore varies in the deposit. This is complicated by the intense folding (Chapter 2) that has caused fS_2 to vary both laterally and vertically.

In sum, I suggest that redistribution of Ag took place during the metamorphism, complicated by a SE to NW decrease in fO_2 and fS_2. The latter caused bornite to be abundant in the SE and absent in the central and northwest zones of the deposit, where arsenopyrite is ubiquitous. Because the Ag contents of galena and fahlore are apparently related to the fS_2 in the system, a spatial pattern of the Ag contents of the major Ag-carriers at Arctic is variably observed.

Chapter 5 Summary and Conclusions

In this study, I have presented metal content and distribution, mineral associations and mineral compositional data for the Arctic volcanogenic massive sulfide (VMS). Arctic formed in a geologic setting that most workers agree represents Kuroko-style VMS deposition. Over time, this deposit has experienced significant temperature, pressure and strain due to depth of burial to blueschist/greenschist metamorphic conditions in a compressional environment followed by tectonic uplift (Chapter 1). It is only natural that during these geologic processes, any original textures or metal zoning that Kuroko-VMS deposits typical display will have been significantly modified. This section is meant to bring all the pieces of the puzzle together to better understand and characterize ore mineralogy and bulk metal distribution through the deposit as it occurs today.

It is generally agreed that the Arctic deposit has been folded, but the degree to which the area has been refolded and/or sheared remains a topic of discussion among workers. Detailed examination of metal ratios through all ore horizons at Arctic shows that the distribution of lithologies (including massive sulfide layers) is consistent with a recumbent isoclinal fold interpretation; however, it appears that each ore horizon represents a series of complex isoclinal folds within itself. Asymmetric metal ratios are observed to represent ore horizons on a limb of a fold. Symmetric metal ratios represent M-style folds indicative of approaching fold closure (Chapter 2). Not only has this degree of folding altered original metal zoning, but mineral distribution and lithologic proximities to various mineral associations have also been affected.

Sphalerite compositions have changed through time as a result of changing fS_2-fO_2 conditions during metamorphism. The degree to which these compositions have changed are dependent on several factors (Chapter 3): fS_2-fO_2, temperature, pressure and lithologic associations. I've presented data supporting that the Fe-content of sphalerite changes depending on proximity to the Graphitic Schist (GS). This ultimately affects

what fS_2-fO_2 conditions will likely be present at any given location within the deposit. Graphite causes low fS_2-fO_2 conditions and results in high-Fe sphalerite. In the absence of graphitic rock, high fS_2 assemblages—bornite+chalcopyrite+low-Fe sphalerite—are present (Chapter 3). These variations in fS_2-fO_2 at Arctic are not only responsible for determining the stable mineral assemblages (sulfides and silicates) and the amount of Fe partitioned into sphalerite, but also play a role in re-partitioning other elements, such as Ag and Ba, into new minerals during metamorphism.

Silver within unmetamorphosed Kuroko deposits is typically contained within Ag-Cu sulfides and these deposits characteristically lack Ag-bearing galena (Chapter 1). I've presented data indicating that ~2/3 of Arctic galena carries the bulk of Ag. This is possible only with the introduction of Bi by way of a coupled substitution. The degree to which Ag partitions into galena is a function of the availability of Bi in the ore. The remaining proportion of Ag is mostly present in Sb-rich fahlore (tetrahedrite) and locally within bornite (Chapter 4). Ag is better able to fit into the crystal lattice of the Sb-rich fahlore end member—mostly due to the size of Sb relative to As—and when the As-rich end member is present, the Ag content is often very low. The composition of fahlore at Arctic is controlled locally by the fS_2-fO_2 conditions present during metamorphism (largely controlled by the absence or presence of graphitic rock; Chapters 3, 4). As arsenopyrite is only stable at low fS_2—and associated with moderate to high Fe sphalerite (Chapter 3), Sb-rich fahlore is preferential for these fS_2 conditions, which in turn allows for more Ag-substitution into tetrahedrite. High Ag-Sb tetrahedrite is preferentially associated with pyrrhotite, high-Fe sphalerite, and generally proximal to carbonaceous gray schist (Chapters 3, 4).

The net result is, at any given location within the Arctic deposit, many variables should be taken into account when characterizing ore mineralogy and metal distribution. A complicated SE to NW decrease in fS_2 and fO_2 is responsible for mineral and associated metal distribution. The copper mineralogy seems to be greatly affected by fS_2-fO_2 conditions at any given location within the deposit but generally appears to be

greatest in the SE portion of the deposit where bornite is more prevalent. Sphalerite, although present in most areas throughout the deposit, has varying amounts of mol% FeS depending on location within the deposit. The closer to graphitic rock, the greater the mol% FeS in sphalerite. Ag deportation and which mineral phases are the preferential hosts also depend on varying fS_2-fO_2 conditions experienced at Arctic. Ag redistribution is not only a function of fS_2-fO_2 —determining the arsenic mineralogy thus allowing for more or less Ag substitution into fahlore—but also dependent on the amount of Bi (Ag in galena) present at a given location. A spatial pattern of FeS contents of sphalerite, metal zonation, and Ag contents of the major Ag-carriers at Arctic is a function of mineral and lithologic associations, and fS_2-fO_2 conditions present during metamorphism that vary throughout the deposit.

References

Abbott, R.N., Jr., and Bandy, B.R. (2008) Amphibolite and Blueschist-Greenschist Facies Metamorphism, Blue Mountain Inlier, Eastern Jamaica. In: Geological Crustal and Biotic Evolution of the Caribbean Plate: A tribute to T.A. Jackson. Donovan, S.K. (ed.) Geological Journal, 43, 525-541, DOI: 10.1002/gj.1126.

Barnes, H.L. (1979) Solubilities of Ore Minerals. In: Geochemistry of Hydrothermal Ore Deposits Second Edition. Barnes HL (ed.) Wiley, 404-460.

Bethe, C. (2000) The Geochemist's Workbench software package. University of Illinois, Urnama-Champaign.

Craig, J.R., and Vokes, F.M. (1993) The metamorphism of pyrite and pyritic ores: an overview. Mineralogical Magazine, 57, 3-18.

Chutas, N., Kress, V.C., Ghiorso, M.S., and Sack, R.O. (2008) A solution model for high-temperature PbS-$AgSbS_2$-$AgBiS_2$ galena. American Mineralogist, 93, 1630-1640.

Chutas, N. (2008) Annual Exploration Report on the Arctic Property: NovaGold Resources Inc., Unpublished Report, 35 p.

Dusel-Bacon, C., Brosgbe, W.P., Till, A.B., Doyle, E.O., Mayfield, C.F., Reiser, H.N., and Miller, T.P. (1989) Distribution, Facies, Ages, and Proposed Tectonic Associations of Regionally Metamorphosed Rocks in Northern Alaska. Regional Metamorphosed Rocks of Alaska USGS Professional Paper 1497-A, A1-A44.

Gilbert, W.G., Wiltse, M.A., Carden, J.R., Forbes, R.B., and Hackett, S.W. (1977) Geology of Ruby Ridge, southwestern Brooks Range, Alaska: Alaska Division of Geological and Geophysical Surveys Geologic Report, 58, 16 p.

Glasby, G.P., Iizasa, K., Hannington, M., Kubota, H., and Notsu, K. (2008) Mineralogy and composition of Kuroko deposits from northeastern Honshu and their possible modern analogues from the Izu-Ogasawara (Bonin) Arc south of Japan: Implications for mode of formation. Ore Geology Reviews, 34, 547-560.

Hall. A.J. (1986) Pyrite-pyrrhotine redox reactions in nature. Mineralogical Magazine, 50, 223-229.

Hitzman, M.W. (1980) Devonian to recent tectonics of the southwestern Brooks Range, Alaska [abs.]: Geological Society of America Abstracts with Programs, 17, p. 447.

Hitzman, M.W. (1982) The metamorphic petrology of the southwestern Brooks Range, Alaska [abs.]: Geological Society of America Abstracts with Programs, 14, p. 173.

Hsu, L.C. (1994) Cymrite: new occurrence and stability. Contributions to Mineral Petrology, 118, 314-320.

Hunt, J. (2005) The geology and genesis of iron oxide-copper-gold mineralisation associated with Wernecke Breccia, Yukon, Canada. PhD Thesis, James Cook University, Australia, 238 p.

Hutcheon, I. (1978) Calculation of metamorphic pressure using sphalerite-pyrrhotite-pyrite equilibrium. American Mineralogist, 63, 87-95.

Kitazono, S., and Ueno, H. (2003) Mineralogical and Genetical Aspects of the Doyashiki Kuroko Deposits, Hokuroku Basin, Japan. Resource Geology, 53, no.2, 143-153.

Lambert, I.B., and Sato, T. (1974) The Kuroko and Associated Ore Deposits of Japan: A Review of Their Features and Metallogenesis. Economic Geology, 69, 1215-1236.

Large, R.R. (1992) Australian volcanic-hosted massive sulfide deposits—Features, styles, and genetic models: Economic Geology, v. 87, p. 471–510

Lindberg, P.A. (2004) Structural Geology of the Arctic Cu-Zn-Pb-Ag Sulfide Deposit. Alaska Gold Company internal report, 1-17.

Lusk, J., and Ford, C.E. (1978) Experimental extension of the sphalerite geobarometer to 10 kbars. American Mineralogist, 63, 516-519.

Lynch, G. and Mengel, F. (1995) Metamorphism of arsenopyrite-pyrite-sphalerite-pyrrhotite lenses, western Cape Breton Island, Canada. The Canadian Mineralogist, 33, no. 1, 105-114.

Newberry, R.J., Crafford, T.C., Newkirk, S.R., Young, L.E., Nelson, S.W., and Duke, N.A. (1997) Volcanogenic massive sulfide deposits of Alaska. In: Mineral deposits of Alaska: Economic Geology Monograph, 9. Goldfarb, R.J. and Miller, L. D., (eds), 120-150.

Ono S., Sato, J. (1995) Gold and silver ores from the Ezuri Kuroko ore deposits, Akita Prefecture, Japan. Journal of Mineralogy, Petrology, and Economic Geology, 90, 268-279.

Patrick, B. (1995) High-pressure-low-temperature metamorphism of granitic orthogneiss in theBrooks Range, northern Alaska. Journal of Metamorphic Geology, 13, no. 1, 111-124.

Proffett, J.M. (1999) Structural re-interpretation and additional resource potential of the Arctic deposit: Reno, Kennecott Minerals Company, Unpublished Report, 32 p.

Rigby N., White, R., Bair, D.K., Beck, J., Kuestermeyer, A., and Michael N. (2008) NI 43-101 SRK Consulting Technical Report on Resources, Ambler Project, Arctic Deposit Alaska.

Russell, R. H. (1977). Annual Report, Arctic Deposit. Bear Creek Mining Company Unpublished Report.

Russell, R.H. (1995) Arctic Project 1995 Evaluation Geologic Report: Kennecott Corporation, Unpublished Report, 69 p.

Sack, R.O., and Ebel, D.S. (2006) Thermochemistry of Sulfide Mineral Solutions. Reviews in Mineralogy and Geochemistry, 61, 265-364.

Schmandt, D. (2009) Mineralogy and origin of Zn-rich horizons within the Arctic Volcanogenic Massive Sulfide deposit, Ambler District, Alaska. Undergraduate Thesis, Smith College, 59 p.

Schmidt, J.M. (1983) Geology and geochemistry of the Arctic prospect, Ambler district, Alaska: Ph.D. dissertation, Stanford University, 253 p.

------ (1986) Stratigraphic setting and mineralogy of the Arctic Volcanogenic Massive sulfide prospect, Ambler district, Alaska. Economic Geology, 81, 1619-1643.

------ (1988) Mineral and whole-rock compositions of seawater-dominated hydrothermal alteration at the Arctic volcanogenic massive sulfide prospect, Alaska. Economic Geology, 83, 822-842.

Shannon, R.D. (1976) Revised effective ionic radii and systematic studies of interatomic distances in halides and chalcogenides. Acta Crystallographica, A32: 751-767.

Scott, S.D. (1976) Application of the sphalerite geobarometer to regionally metamorphosed terrains. American Mineralogist, 61, 661-670.

Stephens, J.D., and Cameron, J.W. (1970) Arctic Alaska Project – Mineralogic Study of Diamond Drill Core Samples: Technical Report 70-01. Kennecott Research Center – Metal Mining Division, 21 p.

Till, A.B., Dumoulin J.A., Harris, A.G., Moore, T.E., Bleick, H.A., and Siwiec, B.R. (2008) Bedrock Geologic Map of the southern Brooks Range, Alaska, and accompanying Conodont Data. USGS Open File Report 2008-1149, 88 p.

Toulmin III, P., Barton Jr., P.B., Wiggins, L.B. (1991) Commentary on the sphalerite geobarometer. American Mineralogist, 76, 1038-1051.

Twelker, E. (2008) Immobile element lithogeochemistry work at Arctic, A Progress Report: NovaGold Resources Inc, Unpublished Report, 11 p.

Urabe, T., and Marumo, K. (1991) A new model for Kuroko-type deposits of Japan. Episodes 14, 246–251.

van Zyl, C. (1982) Rapid Preparation of Robust Pressed Powder Briquettes Containing a Styrene and Wax Mixture as Binder. X-Ray Spectrometry, 11, 29-31.

Vaughn, D.J., Craig, J.R. (1997) Sulfide ore mineral stabilities, morphologies, and intergrowth textures. In: Geochemistry of Hydrothermal Ore Deposits Third Edition. Barnes HL (ed) Wiley, 367-434.

Wilkins, G., Stoyko, H.W., Ghaffari, H., DiMarchi, J., Huang, J., Silva, M., O'Brien, M.F., Chin, M., Hafez, S.A. (2013) NI 43-101 Tetra Tech Preliminary Economic Assessment Report on the Arctic Project, Ambler Mining District, Northwest Alaska.

Appendix 1

Table 1-1	As and Sb Contents in Arctic Galena					
	WDS Quantitative Analysis					
Sample	**Drill hole**	**Depth**	**Wt% As**	**St Dev**	**Wt% Sb**	**St Dev**
197-1	128	90.69	0.01	0.02	0.02	0.01
197-2	128	90.86	-0.01	0.04	0.00	0.02
197-3	128	90.98	0.02	0.02	0.01	0.02
197-5	128	91.345	0.02	0.02	0.02	0.02
197-6	128	91.47	-0.01	0.02	0.02	0.01
197-7	128	91.62	0.02	0.02	0.03	0.01
197-8	128	92.01	0.00	0.04	0.01	0.02
197-9	128	92.06	0.04	0.1	0.02	0.03
198-1	128	92.15	0.01	0.01	0.01	0.01
198-6	128	93.115	0.01	0.01	0.01	0.02
198-7	128	93.265	0.00	0.02	0.01	0.02
198-8	128	93.39	-0.01	0.02	0.00	0.02
198-9	128	93.525	-0.01	0.02	0.01	0.02
199-1	128	93.62	0.00	0.03	0.02	0.01
178-1	129	200.06	0.05	0.04	0.01	0.01
178-2	129	103.85	0.02	0.1	0.01	0.02
177-1	129	151.31	0.01	0.02	0.02	0.02
176-1	129	152.42	0.00	0.01	0.02	0.02
180-3	129	152.57	0.04	0.1	-0.01	0.02
180-2	129	152.905	-0.01	0.02	0.02	0.02
180-1	129	152.94	0.01	0.02	0.02	0.01
179-1	129	200.86	0.00	0.01	0.02	0.01
184-1	129	153.04	0.00	0.02	0.01	0.02
182-3	129	157.97	0.01	0.01	0.00	0.1
182-2	129	158.43	0.02	0.02	0.00	0.02
167-2	129	163.03	0.01	0.02	0.01	0.02
167-1	129	166.95	0.00	0.02	0.02	0.02
166-2	129	185.63	0.01	0.02	0.00	0.02
166-1	129	185.64	0.01	0.03	-0.01	0.02
164-3	129	185.96	0.01	0.02	0.00	0.02
164-2	129	186.01	0.01	0.01	0.01	0.01
164-1	129	186.21	0.01	0.02	0.00	0.02
165-2	129	186.29	0.01	0.03	0.01	0.02

Table 1-1 cont.	As and Sb Contents in Arctic Galena					
	WDS Quantitative Analysis					
Sample	**Drill hole**	**Depth**	**Wt% As**	**St Dev**	**Wt% Sb**	**St Dev**
165-1	129	186.82	0.02	0.04	0.02	0.04
163-2	129	186.83	0.00	0.02	0.01	0.01
163-1	129	186.895	0.00	0.02	0.01	0.02
157-3	129	199.39	-0.01	0.02	0.01	0.02
157-2	129	199.515	-0.01	0.03	-0.00	0.03
157-1	129	200.13	-0.01	0.03	0.00	0.02
155-6	129	201.2	-0.01	0.02	0.01	0.02
173-3	129	201.32	0.01	0.03	0.01	0.02
173-1	129	202.875	0.00	0.02	0.02	0.02
175-3	129	202.91	0.01	0.02	0.1	0.03
175-1	129	203.2	0.00	0.01	0.01	0.02
158-3	129	203.45	0.01	0.1	0.02	0.1
158-2	129	204.25	0.04	0.1	-0.02	0.1
158-1	129	204.26	0.03	0.1	-0.02	0.1
153-1	129	205.47	0.05	0.1	0.1	0.1
172-2	129	205.77	0.04	0.2	0.1	0.1
190-5	130	168.44	0.01	0.02	0.03	0.03
191-1	130	171.75	-0.03	0.03	0.01	0.01
191-2	130	171.95	0.02	0.03	-0.00	0.02
191-3	130	172.04	-0.02	0.02	0.02	0.02
191-4	130	172.21	-0.02	0.02	0.02	0.02
191-5	130	172.66	0.00	0.02	-0.01	0.02
191-6	130	172.9	0.00	0.02	0.01	0.02
192-2	130	173.44	0.00	0.02	0.01	0.01
192-3	130	173.52	0.13	0.4	0.56	1.6
192-4	130	173.55	-0.02	0.04	0.01	0.02
192-5	130	174.025	-0.01	0.02	0.01	0.02
192-6	130	174.3	0.00	0.02	0.01	0.01
192-7	130	175.22	-0.00	0.02	-0.00	0.02
192-8	130	175.29	-0.01	0.02	-0.00	0.02
192-9	130	175.35	0.00	0.03	0.01	0.02
193-1	130	175.89	0.01	0.02	0.02	0.01
193-2	130	176	0.01	0.02	0.02	0.02
193-3	130	176.85	0.01	0.02	0.00	0.02
193-4	130	176.96	0.01	0.01	0.02	0.02

Table 1-1 cont.	As and Sb Contents in Arctic Galena					
	WDS Quantitative Analysis					
Sample	**Drill hole**	**Depth**	**Wt% As**	**St Dev**	**Wt% Sb**	**St Dev**
193-5	130	177.5	0.01	0.02	0.00	0.01
193-6	130	177.57	-0.01	0.01	0.00	0.02
193-7	130	177.635	0.01	0.02	-0.01	0.01
193-9	130	177.98	-0.01	0.02	0.01	0.01
194-1 Tet	130	178.26	0.01	0.03	-0.01	0.01
194-3	130	178.51	0.00	0.03	-0.01	0.01
194-4	130	178.96	-0.02	0.02	0.00	0.01
194-5	130	179.14	-0.04	0.03	-0.01	0.1
194-6	130	179.28	-0.02	0.02	0.00	0.02
194-7	130	179.88	0.00	0.02	0.03	0.03
195-1	130	191.66	-0.00	0.02	-0.01	0.02
195-2	130	191.76	-0.01	0.02	-0.00	0.02
195-3	130	191.96	-0.01	0.02	0.00	0.01
196-1	130	197.22	-0.01	0.01	0.00	0.01
196-3	130	197.53	0.01	0.03	0.01	0.03
196-5	130	198.11	0.01	0.02	0.02	0.01
200-1	131	125.4	0.04	0.04	0.00	0.01
200-2	131	127.24	0.1	0.1	-0.6	1.5
200-4	131	127.59	0.1	0.1	0.2	0.3
200-5	131	127.7	0.03	0.02	0.1	0.02
200-6	131	166.89	0.01	0.01	0.01	0.03
200-7	131	166.96	0.02	0.01	0.01	0.01
200-8	131	167.14	0.03	0.04	0.00	0.02
200-9	131	167.45	0.1	0.02	0.01	0.02
201-1	131	167.53	0.03	0.01	-0.01	0.01
201-2	131	167.58	0.01	0.01	0.01	0.02
201-3	131	167.73	0.02	0.02	0.01	0.02
201-4	131	167.85	0.03	0.03	0.01	0.02
201-5	131	168	0.02	0.02	0.01	0.02
201-6	131	168.4	0.02	0.03	0.01	0.03
AR48B	AR48B	38.4	0.01	0.03	0.04	0.02
AR79	AR79	174.19	0.02	0.02	0.1	0.03
AR54	AR54	25.1	-0.00	0.03	0.03	0.03
AR66	AR66	30.4	0.02	0.03	0.1	0.03
AR89	AR89	239.1	0.01	0.03	0.04	0.02

Table 1-1 cont.	As and Sb Contents in Arctic Galena					
	WDS Quantitative Analysis					
Sample	**Drill hole**	**Depth**	**Wt% As**	**St Dev**	**Wt% Sb**	**St Dev**
AR50	AR50	38.63	0.01	0.03	0.1	0.02
AR86	AR86	169.28	-0.02	0.02	0.1	0.01
AR78B	AR78B	238.89	-0.01	0.03	0.1	0.01
AR18	AR18	75.01	-0.01	0.02	0.04	0.02
AR26A	AR26A	32.82	-0.00	0.01	0.1	0.01
AR51	AR51	44.2	-0.01	0.02	0.04	0.01
AR83	AR83	264.6	-0.02	0.01	0.1	0.01
AR92	AR92	143.9	-0.01	0.02	0.04	0.01
AR93	AR93	144.36	-0.01	0.02	0.1	0.01

Appendix 2

Table 2-1	Partial 'Fahlore' Analysis			
	EDS Semi-quantitative Analysis			
Wt %	BB101-Avg Tet	BB102-Avg Tet	BB107-Avg Tet	BB106-Avg Tet
S	27.4	27.0	27.5	
Ag	0.8	1.5	0.4	16.0
Sb	8.9	22.9	1.6	
Fe	3.8	5.0	4.3	
Cu	41.7	36.6	43.1	
Zn	4.3	2.4	3.9	
As	13.6	4.8	19.3	
At %				
S	44.9	45.6	44.7	
Ag	0.4	0.7	0.2	
Sb	3.9	10.1	0.6	
Fe	3.6	4.8	3.9	
Cu	34.5	31.1	34.4	
Zn	3.4	2.0	3.0	
As	9.5	3.5	13.2	
As/(As+Sb)	0.71	0.26	0.90	
Zn(Zn+Fe)	0.49	0.29	0.40	
Ag/(Ag+Cu)	0.01	0.02	0.01	
Sb/(Sb+As)	0.29	0.77	0.05	
Formula				
S	13.0	13.0	13.0	
Ag	0.0	0.2	0.1	
Sb	1.1	2.9	0.2	
Fe	1.0	1.4	1.1	
Cu	10.0	8.9	10.0	
Zn	1.0	0.6	0.9	
As	2.8	1.0	3.8	
As+Sb	3.88	3.88	4.01	
Zn+Fe	2.05	1.93	2.01	

Table 2-2	Partial 'Fahlore' Analysis							
	WDS Quantitative Analysis							
Sample	Avg Wt% Ag	Stdev Ag	Avg Wt% As	Stdev As	Avg Wt% Sb	Stdev Sb	Avg atm (Sb/(As+Sb))	St Dev
AR48B-Tet	1.7	0.2	3.8	1.6	22.8	2.1	0.8	0.1
AR48B-Tenn	0.5	0.1	14.8	0.9	5.8	1.4	0.2	0.0
AR79	0.6	0.1	9.8	1.4	13.0	2.0	0.45	0.03
AR54	0.3	0.2	14.1	0.4	6.7	0.5	0.22	0.02
AR51	0.3	0.0	13.4	2.3	1.4	0.4	0.06	0.02
197-1	0.8	0.2	2.4	1.0	27.0	1.7	0.9	0.1
197-8	0.11	0.02	15.8	0.5	4.5	0.5	0.15	0.01
197-9	0.11	0.02	16.2	0.3	4.0	0.5	0.13	0.02
198-1	0.14	0.02	15.7	0.2	5.7	0.2	0.18	0.00
198-2	0.3	0.1	11.8	1.1	11.5	1.6	0.4	0.1
198-4	0.24	0.03	11.3	0.5	11.7	0.8	0.39	0.03
198-5	0.4	0.2	8.9	1.5	15.0	2.5	0.5	0.1
198-6	0.8	0.1	6.8	1.0	19.7	1.4	0.6	0.1
198-8	0.34	0.04	9.5	0.5	15.2	0.9	0.50	0.03
198-9	0.16	0.02	7.21	0.04	19.0	0.3	0.62	0.00
178-1	0.2	0.1	11.8	1.6	10.9	2.5	0.4	0.1
176-1	0.8	0.2	8.2	0.8	17.3	1.3	0.6	0.04
180-5	0.3	0.05	5.5	0.6	20.9	1.1	0.7	0.03
180-3	1.9	0.2	2.6	0.04	26.3	0.2	0.9	0.00
180-2	0.3	0.1	13.7	1.1	8.1	1.5	0.3	0.1
180-1	0.4	0.2	13.3	3.0	8.3	3.8	0.3	0.1
182-3	4.2	0.4	0.6	0.04	28.9	0.1	1.0	0.00
182-1	0.4	0.1	10.5	1.4	13.3	2.2	0.4	0.1
186-1	1.7	0.3	3.3	0.8	24.7	1.3	0.8	0.04
168-1	0.5	0.1	12.2	2.7	7.9	2.5	0.3	0.1
168-2	0.4	0.1	14.7	1.8	5.8	2.2	0.2	0.1
164-2	0.8	0.5	9.9	4.0	13.9	6.7	0.5	0.2
163-1	0.4	0.1	15.9	2.1	2.9	2.3	0.1	0.1
173-2	0.7	0.1	3.1	2.1	25.7	3.5	0.8	0.1
173-1	0.8	0.2	2.5	2.2	26.4	4.2	0.9	0.1
175-3	1.0	0.4	5.9	0.8	20.8	1.1	0.7	0.04
175-2	0.7	0.2	4.7	2.1	23.0	3.3	0.8	0.1
175-1	0.7	0.1	2.7	1.7	25.8	3.4	0.9	0.1

Table 2-2 cont.	Partial 'Fahlore' Analysis							
	WDS Quantitative Analysis							
Sample	Avg Wt% Ag	Stdev Ag	Avg Wt% As	Stdev As	Avg Wt% Sb	Stdev Sb	Avg atm (Sb/(As+Sb))	St Dev
153-1	13.5	0.6	0.5	0.3	23.0	0.6	1.0	0.02
172-1	0.7	0.3	1.1	0.6	24.1	1.0	0.9	0.04
172-2	0.8	0.2	5.7	2.1	15.8	3.4	0.6	0.1
174-1	0.5	0.0	0.7	0.2	24.6	0.5	1.0	0.01
191-2	0.4	0.0	7.1	0.3	19.2	0.5	0.6	0.01
191-3	0.5	0.1	7.0	1.8	19.6	2.8	0.6	0.1
191-7	0.2	0.1	11.1	3.3	12.7	5.3	0.4	0.2
191-8	0.2	0.0	10.7	3.0	13.7	4.8	0.4	0.2
191-9	0.2	0.1	12.4	3.5	11.0	5.5	0.4	0.2
192-1	0.3	0.0	8.6	0.4	16.8	0.6	0.5	0.02
192-2	0.2	0.1	11.0	2.1	13.0	3.3	0.4	0.1
192-3	0.2	0.1	10.6	2.3	13.1	3.7	0.4	0.1
192-4	0.2	0.0	11.0	1.6	13.1	2.4	0.4	0.1
192-5	0.3	0.0	11.6	0.6	11.8	1.1	0.4	0.03
192-6	0.3	0.0	9.5	0.6	13.2	1.4	0.5	0.01
193-1	0.8	0.1	6.1	2.4	21.0	3.6	0.7	0.1
193-2	0.9	0.1	3.3	0.9	25.5	1.4	0.8	0.05
193-6	0.6	0.1	6.1	1.1	20.6	1.7	0.7	0.1
193-8	0.4	0.1	3.1	0.3	25.6	0.5	0.8	0.02
194-1 Tet	1.1	0.2	9.6	0.3	14.6	0.4	0.5	0.01
194-1 Tenn	0.6	0.2	15.2	0.9	5.7	1.7	0.2	0.1
194-3	0.2	0.0	16.2	1.7	4.2	2.7	0.1	0.1
194-4	0.6	0.1	13.3	0.5	8.3	0.6	0.3	0.02
194-5	0.5	0.1	4.9	1.0	22.8	1.6	0.7	0.1
195-1	0.5	0.1	8.3	1.1	17.5	1.8	0.6	0.1
195-3	0.5	0.2	1.9	0.5	27.6	0.8	0.9	0.03
196-2	0.2	0.0	18.4	0.3	0.7	0.0	0.0	0.00
196-3	0.3	0.1	9.6	2.7	14.2	2.6	0.5	0.1
196-5	0.5	0.1	10.0	2.0	14.2	2.9	0.5	0.1
196-6	0.2	0.0	18.4	0.4	1.4	0.4	0.0	0.01
200-2	1.9	0.0	3.1	0.4	25.9	0.6	0.8	0.02
200-3	1.1	0.2	0.7	0.1	29.2	1.3	1.0	0.00
200-4	0.4	0.1	2.7	1.0	26.3	1.4	0.9	0.1
200-8	4.9	0.7	1.3	0.2	28.1	0.4	0.9	0.01

Table 2-2 cont.	Partial 'Fahlore' Analysis							
	WDS Quantitative Analysis							
Sample	Avg Wt% Ag	Stdev Ag	Avg Wt% As	Stdev As	Avg Wt% Sb	Stdev Sb	Avg atm (Sb/(As+Sb))	St Dev
201-2	5.2	0.4	1.6	0.4	27.6	0.9	0.9	0.02
201-4	5.2	0.1	1.4	0.1	27.7	0.0	0.9	0.01
201-5	1.2	0.0	1.4	0.3	28.6	0.3	0.9	0.01
201-6	6.1	0.8	1.4	0.2	27.0	2.0	0.9	0.01

Appendix 3

Table 3-1	Magnetic Susceptibility Analyses		
Drillhole	Depth	Magnetic Susceptibility (SI units x 10^{-3})	Notes
AR08-0123	133.64	0.02	
	134.34	0.04	grey schist (not graphitic)
	135.14	0.06	grey schist (not graphitic)
	135.94	0.03	grey schist (not graphitic)
	136.64	0.13	ms
	137.34	0.09	ms
	138.04	0.06	ms
	138.74	0.12	ms
	139.44	0.14	Cu-rich stringer zone
	140.14	0.11	Cu-rich stringer zone
	140.84	0.1	Cu-rich stringer zone
	141.54	0.07	ms
	142.24	0.21	ms+tr mt
	142.94	9	ms+ mt
	143.64	7	ms+ mt
	144.34	0.22	ms+tr mt
	145.14	0.22	fw alt'd rock
	145.94	0.18	fw alt'd rock
	146.74	0.15	fw alt'd rock
	147.44	0.18	fw alt'd rock
	148.24	0.17	fw alt'd rock
	148.94	0.12	fw alt'd rock
AR11-0128	66.6	0.34	
	67.3	0.22	
	68	0.36	
	68.6	0.32	
	69.3	0.15	
	69.9	0.11	
	70.5	0.12	
	71.2	0.1	
	71.9	0.26	
	72.6	0.88	
	73.3	0.95	

Table 3-1 cont.	Magnetic Susceptibility Analyses		
Drillhole	Depth	Magnetic Susceptibility (SI units x 10^{-3})	Notes
AR11-0128	74	2.1	
	74.9	0.41	
	75.6	0.38	
	76.3	0.77	
	77.1	0.57	
	77.8	0.51	
	78.5	0.68	
	79.1	0.75	
	79.8	1.1	
	80.5	1.4	
	81	0.77	
	81.7	0.55	
	82.4	0.6	
	83	0.67	
	83.7	0.37	
	84.4	1.1	
	85	0.39	
	85.7	0.32	
	86.4	1.1	
	87.1	0.77	
	87.8	2.2	
	88.5	0.6	
	89.2	0.8	
	89.9	0.23	
	90.6	0.11	
	91.3	0.27	
	92	0.07	
	92.7	0.03	
	93.4	0.08	
	94.1	2.3	
	94.8	1	
	95.5	1.5	
	96.2	3.2	
	96.9	4.5	
	97.4	0.7	

Table 3-1 cont.	Magnetic Susceptibility Analyses		
Drillhole	Depth	Magnetic Susceptibility (SI units x 10^{-3})	Notes
AR11-0128	98.1	1.5	
	98.8	0.04	
	99.4	2.6	
	100.1	0.5	
	100.8	0.2	
	101.5	0.25	
	102.2	0.5	
	102.9	0.5	
	103.5	1.6	
	104.2	0.3	
	104.9	0.3	
	105.6	0.1	
AR11-0129	0	0.09	
	3	0.11	
	3.7	0.09	
	4.5	0.09	
	5.2	0.11	
	5.9	0.13	
	6.5	0.07	
	7.2	0.15	
	7.9	0.14	
	8.5	0.12	
	9.5	0.15	
	10.5	0.14	
	12.1	0.07	
	12.7	0.29	
	13.7	0.32	
	14.5	0.27	
	15.2	0.31	
	15.9	0.45	
	16.7	0.52	
	17.4	0.27	
	18.1	0.11	
	18.8	0.17	
	19.5	0.12	

Table 3-1 cont.	Magnetic Susceptibility Analyses		
Drillhole	Depth	Magnetic Susceptibility (SI units x 10^{-3})	Notes
AR11-0129	20.3	0.18	
	21	0.15	
	21.7	0.11	
	22.4	0.22	
	23	0.11	
	23.7	0.52	
	24.4	0.22	
	25.1	0.21	
	25.8	0.18	
	26.5	0.42	
	27.2	0.08	
	27.9	0.32	
	28.6	0.21	
	29.3	0.33	
	30	0.29	
	30.7	0.32	
	31.4	0.28	
	32.1	0.26	
	32.8	0.17	
	33.6	0.35	
	34.3	0.38	
	35	0.46	
	35.6	0.41	
	36.3	0.23	
	36.9	0.51	
	37.5	0.19	
	38.2	0.32	
	38.9	0.42	
	39.6	0.29	
	40.3	0.12	
	41.1	0.07	
	41.8	0.11	
	42.5	0.11	
	43.3	0.31	
	44.1	0.2	

Table 3-1 cont.	Magnetic Susceptibility Analyses		
Drillhole	Depth	Magnetic Susceptibility (SI units x 10^{-3})	Notes
AR11-0129	44.8	0.47	
	45.4	0.52	
	46	0.09	
	46.7	0.09	
	47.5	0.08	
	48.2	0.28	
	48.9	0.16	
	49.6	0.11	
	50.3	0.13	
	51	0.22	
	51.7	0.17	
	52.4	0.1	
	53.1	0.11	
	53.8	0.18	
	54.5	0.29	
	55.2	0.22	
	55.9	0.21	
	56.6	0.25	
	57.3	0.09	
	58	0.18	
	58.7	0.12	
	59.4	0.12	
	60.1	0.08	
	60.9	0.13	
	61.6	0.09	
	62.2	0.19	
	62.9	0.23	
	63.6	0.17	
	64.4	0.37	
	65.1	0.41	
	65.8	0.22	
	66.4	0.15	
	67	0.25	
	67.7	0.23	
	68.4	0.35	

Table 3-1 cont.	Magnetic Susceptibility Analyses		
Drillhole	Depth	Magnetic Susceptibility (SI units x 10^{-3})	Notes
AR11-0129	69.1	0.08	
	69.8	0.17	
	70.5	0.17	
	71.1	0.23	
	71.8	0.27	
	72.5	0.13	
	73.2	0.19	
	73.9	0.14	
	74.6	0.15	
	75.3	0.17	
	76	0.19	
	76.7	0.16	
	77.3	0.14	
	78	0.26	
	78.7	0.17	
	79.3	0.13	
	80	0.16	
	80.7	0.18	
	81.4	0.24	
	82.1	0.19	
	82.8	0.11	
	83.4	0.12	
	84.1	0.13	
	84.8	0.19	
	85.3	0.14	
	86	0.11	
	86.7	0.14	
	87.4	0.17	
	88.1	0.12	
	88.8	0.12	
	89.6	0.17	
	90.3	0.21	
	91	0.15	
	91.7	0.19	
	92.4	0.08	

Table 3-1 cont.	Magnetic Susceptibility Analyses		
Drillhole	Depth	Magnetic Susceptibility (SI units x 10^{-3})	Notes
AR11-0129	93.1	0.1	
	93.8	0.07	
	94.5	0.06	
	95.2	0.33	
	95.9	0.08	
	96.6	0.22	
	97.2	0.07	
	98	0.13	
	98.7	0.14	
	99.4	0.15	
	100	0.19	
	100.7	0.17	
	101.4	0.18	
	102	0.07	
	102.7	0.27	
	103	0.26	
	103.3	0.22	
	103.8	7.3	
	104.1	0.08	
	104.8	0.05	
	105.3	0.04	
	106	0.06	
	106.7	0.05	
	107.4	0.06	
	108.2	0.06	
	108.9	0.05	
	109.5	0.06	
	110.1	0.05	
	110.8	0.08	
	111.5	0.06	
	112.1	0.09	
	112.8	0.08	
	113.5	0.13	
	114.3	0.06	
	115	0.09	

Table 3-1 cont.	Magnetic Susceptibility Analyses		
Drillhole	Depth	Magnetic Susceptibility (SI units x 10^{-3})	Notes
AR11-0129	115.7	0.14	
	116.3	0.11	
	117	0.08	
	117.7	0.07	
	118.2	0.05	
	118.9	0.07	
	119.1	0.06	
	120.4	0.09	
	121.1	0.07	
	121.8	0.05	
	122.5	0.05	
	123.1	0.05	
	123.8	0.05	
	124.6	0.06	
	125.3	0.05	
	126	0.06	
	126.7	0.05	
	127.4	0.04	
	128	0.06	
	128.6	0.05	
	129.3	0.06	mu
	130	0.38	chl
	130.6	0.39	chl
	131.2	0.43	
	131.9	0.28	
	132.6	0.1	mu
	133.3134	0.12	
	134	0.11	
	134.7	0.14	
	135.4	0.1	
	136.1	0.09	
	137.2	0.06	
	137.9	0.04	
	138.7	0.04	
	140.5	0.03	

Table 3-1 cont.	Magnetic Susceptibility Analyses		
Drillhole	Depth	Magnetic Susceptibility (SI units x 10^{-3})	Notes
AR11-0129	141.2	0.04	
	141.9	0.02	
	142.6	0.02	
	143.3	0.04	grey schist
	144	0.16	
	145.2	0.17	ms
	145.9	0.18	ms
	146.4	0.05	ms
	146.9	0.11	chl
	147.6	0.13	
	148.3	0.14	
	149	0.17	chl
	149.7	0.16	
	150.4	0.14	
	151.2	0.16	ms
	151.9	0.18	ms
	152.6	0.16	ms
	153.1	0.17	ms
	153.8	0.13	
	154.5	0.2	
	155.1	0.43	
	155.8	0.21	
	156.3	0.3	
	157.1	0.34	
	157.8	0.19	ms
	158.5	0.29	ms
	159.2	0.16	ms
	159.9	0.12	ms
	160.6	0.34	ms
	161.1	0.27	ms
	161.8	0.38	ms
	162.5	0.13	ms
	163.1	0.17	chl-mu
	163.8	0.11	
	164.5	0.24	

Table 3-1 cont.	Magnetic Susceptibility Analyses		
Drillhole	Depth	Magnetic Susceptibility (SI units x 10^{-3})	Notes
AR11-0129	165.4	0.27	talc?
	166.1	0.17	
	166.8	0.23	ms
	167.6	0.13	grey schist
	168.3	0.21	
	169	1.5	
	169.6	0.7	
	170.3	1.8	
	171	0.7	
	171.6	0.76	
	172.3	1.2	
	173	0.46	
	173.7	2.5	
	174.4	1.5	
	175	2.2	
	175.6	2	
	176.3	2.2	
	177	1.6	
	177.5	2.5	
	178.2	2.2	
	178.9	2.5	
	179.5	3.8	
	180.2	2.2	
	180.9	2.2	
	181.5	0.4	
	182.2	1.1	
	182.9	0.18	
	183.5	0.04	
	184.1	0.57	
	184.8	0.07	
	185.6	0.1	ms
	186.3	0.16	ms
	187	0.14	ms
	187.7	0.14	ms
	188.4	0.29	ms

Table 3-1 cont.	Magnetic Susceptibility Analyses		
Drillhole	Depth	Magnetic Susceptibility (SI units x 10^{-3})	Notes
AR11-0129	189.1	0.21	ms
	189.8	0.6	ms
	190.5	0.33	
	191.2	2.7	
	192.5	0.47	
	193.2	0.43	
	193.9	0.48	
	194.6	12	
	195.3	4	
	196	14	
	197.1	4.9	
	197.8	0.4	
	198.5	0.3	
	199.3	0.15	ms
	200	1.5	ms
	200.7	0.08	ms
	201.2	0.05	ms
	201.9	0.14	ms
	202.6	9	ms
	203.1	0.1	ms
	203.8	0.24	ms
	204.5	4.1	ms
	205.3	0.4	ms
	206	0.06	
	206.8	0.07	
	207.5	1.5	
	208.2	0.07	
	209	0.73	
	209.4	1.8	
	210	2.2	
	210.7	2.1	
	211.5	3.3	
	212.2	3.2	
	212.8	3.3	
	213.4	4.9	

Table 3-1 cont.	Magnetic Susceptibility Analyses		
Drillhole	Depth	Magnetic Susceptibility (SI units x 10^{-3})	Notes
AR11-0129	214	4.5	
	214.7	2.2	
	215.4	4	
	216.1	3.1	
	216.8	2.8	
	217.4	2.7	
	218.1	4.8	
	218.8	4.9	
	219.5	1.9	
	220.2	2.8	
	220.9	3.5	
	221.4	1.1	
	222.1	2.5	
	222.8	1.7	
	223.4	1.3	
	224.1	1.5	
	224.8	2.2	
	225.5	5	
	226.2	6.5	
	226.9	3.7	
	227.6	3.6	
	228.3	1.1	
	229	1.3	
	229.6	2.8	
	230.3	3.3	
	231	5.8	
	231.7	2.2	
	232.4	2.7	
	233.1	1.9	
	233.7	3.5	
	234.4	2.7	
	235.1	3.5	
	235.7	3.7	
	236.4	1.4	
	237.1	2.4	

Table 3-1 cont.	Magnetic Susceptibility Analyses		
Drillhole	Depth	Magnetic Susceptibility (SI units x 10^{-3})	Notes
AR11-0129	237.8	0.4	
	238.5	0.25	
	239.1	0.26	
	239.8	0.43	
	240.5	12.5	
	241.2	0.26	
	241.9	0.19	
	242.6	0.17	
	243.1	0.3	
	243.8	0.22	
	244.5	0.15	
	245.3	0.2	
	246	0.18	
	246.7	0.14	
	247.4	0.25	
	248	0.23	
	248.7	0.26	
	249.4	0.22	
	250	0.25	
	250.7	0.21	
	251.4	0.22	
	252	1.1	
	252.7	5	
	253.4	0.16	
	253.8	0.23	
	254.5	0.14	
	255.2	0.13	
	255.9	0.16	
	256.6	0.15	
	257.3	0.12	
	258	0.13	
	258.7	0.09	
	259.3	0.18	
	260	0.21	
	260.7	0.15	

Table 3-1 cont.	Magnetic Susceptibility Analyses		
Drillhole	Depth	Magnetic Susceptibility (SI units x 10^{-3})	Notes
AR11-0129	261.3	0.12	
	262	0.17	
AR11-0130	149.3	0.08	mrp
	150	0.06	mrp
	150.7	0.05	mrp
	151.3	0.09	mrp
	152	0.05	mrp
	152.6	0.09	mrp
	153.1	0.11	mrp
	153.8	0.06	mrp
	154.5	0.07	mrp
	155.2	0.06	mrp
	155.9	0.06	mrp
AR11-0130	156.6	0.07	mrp
	157.3	0.11	mrp
	158	0.11	mrp
	158.7	0.09	mrp
	159.4	0.6	albitic seds?
	160.1	0.3	grey schist
	160.8	0.42	grey schist
	161.5	0.33	grey schist
	162.2	0.14	grey schist
	162.9	0.21	grey schist
	163.7	0.82	grey schist
	164.5	0.6	grey schist
	165.3	1.7	grey schist
	166.1	0.7	hi ba-grey schist
	166.9	0.1	wk mz
	167.7	0.03	Cu-rich stringer zone
	168.4	0.2	ms
	169.1	2.5	hi ba-grey schist
	169.6	4	
	170.3	missing	
	170.9	2	hi ba-grey schist
	171.5	0.2	wk mz

Table 3-1 cont.	Magnetic Susceptibility Analyses		
Drillhole	**Depth**	**Magnetic Susceptibility (SI units x 10^{-3})**	**Notes**
AR11-0130	172.2	missing	
	172.9	0.03	Cu-rich stringer zone
	173.6	0.05	Cu-rich stringer zone
	174.4	0.2	ms
	175.1	0.4	ms
	175.8	0.14	ms
	176.5	0.2	ms
	177.2	3	ms
	177.9	8	ms
	178.6	10	ms
	179.3	0.15	
	180	0.18	mrp?
	180.6	0.08	mrp
	181.3	0.2	mrp
	182	0.25	
	182.7	0.28	mrp
	183.5	0.18	
	184.2	0.17	
	185	0.18	mrp?
	185.7	4	grey schist
	186.4	1.5	
	187.2	1.8	grey schist
	188.4	1.6	
	189.3	5	
	190.5	3	grey schist
	191.3	0.15	ms
	192.1	1.7	grey schist
	192.8	4.3	grey schist
	193.5	5	
	194.2	3.5	
	194.8	1.6	hi ba-grey schist
	195.5	0.6	
	196.1	0.14	
	196.7	0.1	bio-alb?
	197.4	0.06	ms

Table 3-1 cont.	Magnetic Susceptibility Analyses		
Drillhole	Depth	Magnetic Susceptibility (SI units x 10^{-3})	Notes
AR11-0130	198.1	0.05	ms
	198.8	4.5	hi ba-grey schist
	199.5	5.5	grey schist
	200.2	5	grey schist
	200.9	3	grey schist
	201.6	1.5	grey schist
	202.2	2.5	grey schist
	202.8	2.3	grey schist
	203.5	2.7	grey schist
	204.2	4.4	grey schist
	204.9	5	grey schist
	205.6	0.4	grey schist
	206.3	0.07	mrp
	207	0.13	mrp
	207.7	0.12	mrp
	208.4	0.13	mrp
	209	0.11	mrp
	209.7	0.12	mrp
	210.4	0.19	mrp
	211.2	0.16	mrp
AR11-0131	106.8	0.4	
	107.5	0.4	
	108.3	0.4	
	109	0.1	
	109.7	0.2	
	110.4	0.3	
	111	0.3	
	111.7	0.1	
	112.4	0.4	
	113	0.7	
	113.7	0.2	
	114.4	0.2	
	115.5	0.4	
	116.2	0.1	
	116.9	0.3	

Table 3-1 cont.	Magnetic Susceptibility Analyses		
Drillhole	Depth	Magnetic Susceptibility (SI units x 10^{-3})	Notes
AR11-0131	117.6	0.5	
	118.3	0.5	
	119	1.3	
	119.7	0.4	
	120.4	1.4	
	121.1	0.1	
	121.8	0.1	
	122.5	0.1	
	122.5	0.1	
	123.2	0.1	
	124	0.4	
	124.7	0.4	
	125.4	0.7	ms
	126.1	1.6	
	126.8	2.3	
	127.5	0.6	
	128.2	2.2	
	128.9	1.3	
	129.6	1.8	
	130.4	1.1	
	131.1	1.9	
	131.8	0.8	
	132.3	1.7	
	133	1.6	
	133.7	1.3	
	134.4	1.2	
	135.1	0.7	
	135.8	1.8	
	136.3	0.2	
	137	0.9	
	137.7	0.9	
	138.1	0.2	
	138.8	2.7	
	139.5	2.3	
	140.4	1.5	

Table 3-1 cont.	Magnetic Susceptibility Analyses		
Drillhole	Depth	Magnetic Susceptibility (SI units x 10^{-3})	Notes
AR11-0131	141.1	1.7	
	141.8	2.5	
	142.3	1.9	
	143	1.1	
	143.7	0.7	
	144.3	3.8	
	145	0.5	
	145.7	1.2	
	146.5	0.9	
	147.2	2.1	
	147.8	1.7	
	148.4	0.8	
	149.1	0.6	
	149.8	0.7	
	150.5	0.8	
	151.2	1.7	
	151.9	1.6	
	152.5	0.4	
	153.2	0.1	mrp
	153.9	0.1	mrp
	154.5	0.1	mrp
	155.2	3.2	
	155.9	1.9	
	156.6	1.2	
	157.3	1.1	
	158	1.2	
	158.7	0.9	
	159.4	1.6	
	160.1	0.5	
	160.8	0.3	
	161.5	0.4	
	162.2	1.1	
	163	2.7	
	163.7	3.2	
	164.3	3.5	

Table 3-1 cont.	Magnetic Susceptibility Analyses		
Drillhole	Depth	Magnetic Susceptibility (SI units x 10^{-3})	Notes
AR11-0131	165	8	dssm po
	165.7	5.9	dssm po
	166.4	3	
	167.2	3	ms
	167.9	0.6	
	168.6	1	
	169.3	1.5	
	170	0.7	
	170.7	2.7	
	171.3	0.7	
	172	0.6	
	172.7	0.8	
	173.4	0.5	
	174.1	1.4	
	174.8	1.8	
	175.6	1.6	
	176.3	3	
	177	2	
	177.5	1.1	
	178.3	1.2	
	178.9	0.4	
	179.5	2.1	
	180.2	1.7	
	180.9	0.8	
	181.5	1.1	
	182.2	1.9	
	182.9	2.1	

Notes:
ms = massive sulfide, dssm po = disseminated pyrrhotite, mrp = meta-rhyolite porphyry, ba = barite, bio = biotite, alb = albite, wk minz = weak mineralization, seds = sedimentary, chl = chlorite, mu = muscovite, fw alt'd = footwall altered, tr mt = trace magnetite, mt = magnetite

Appendix 4

Table 4-1	Microprobe Analytical Conditions							
Beam conditions for all elements								
Kilovolts (keV)	25							
Current (nA)	100							
Size (μm)	2							
Magnification	1000							
Analytical Conditions								
Element	Manganese	Sulfur	Iron	Zinc	Silver	Antimony	Bismuth	Arsenic
Element Symbol	Mn	S	Fe	Zn	Ag	Sb	Bi	As
X-Ray	ka	ka	ka	la	la	la	la	la
Crystal	PET	PET	LIF	TAP	PET	PET	LIF	TAP
Spectrometer	1	2	3	4	1	2	3	4
On Peak Position (Sinθ x 10^{-5})	24026	61440	48217	47700	47503	39343	28678	37697
High Background Position (Sinθ x 10^{-5})	363	596	509	975	664	745	663	1097
Low Background Position (Sinθ x 10^{-5})	-398	-596	-509	-975	-664	-745	663	-1097
Count Times								
On Peak	11	10	11	10	20	20	20	20
High Background	10	5	10	10	10	10	1	1
Low Background	1	5	1	1	10	10	20	20

Appendix 5

Ag Accounting Example:

STEP 1: Determine Galena composition (from microprobe): $= wt\%\ Ag \rightarrow convert\ to\ ppm\ Ag$

STEP 2: Divide ppm Ag in Galena by %Pb in Galena where:

Galena standard composition = 86.6 wt% Pb and 14.4 wt% S

$$= \frac{ppm\ Ag\ (from\ microprobe)}{\%\ Pb}$$

STEP 3: Determine %Pb in Rock (from XRF): $= wt\%\ Pb\ in\ Rock$

STEP 4: Calculate amount of total Ag due to Galena by:

$$\boldsymbol{STEP\ 3} * \boldsymbol{STEP\ 2} \rightarrow \%\text{Pb in rock from XRF } (\textbf{Step 3}) * \frac{ppm\ Ag}{\%Pb}\ (\boldsymbol{Step\ 2})$$

$$= (\cancel{\%Pb}\ in\ rock) * \frac{(ppm\ Ag)}{(\cancel{\%Pb})} = ppm\ Ag\ calc'd from\ Gal$$

STEP 5: Determine Fahlore composition (from microprobe):

$$= wt\%\ Ag\ and\ wt\%\ Sb \rightarrow convert\ wt\%\ Ag\ to\ ppm\ Ag$$

STEP 6: Divide ppm Ag in Fahlore by %Sb in Fahlore: $= \frac{ppm\ Ag\ (from\ microprobe)}{\%\ Sb}$

STEP 7: Determine %Sb in Rock (from XRF): $= wt\%\ Sb\ in\ Rock$

STEP 8: Calculate amount of total Ag due to Fahlore by:

$$\boldsymbol{STEP\ 7} * \boldsymbol{STEP\ 6} \rightarrow \%\text{Sb in rock from XRF } (\textbf{Step 7}) * \frac{ppm\ Ag}{\%Sb}\ (\boldsymbol{Step\ 6})$$

$$= (\cancel{\%Sb}\ in\ rock) * \frac{(ppm\ Ag)}{(\cancel{\%Sb})} = ppmAg\ calc'd from\ Fah$$

STEP 9: Determine **Calculated Total** Ag in rock (ppm) by:

$$= ppmAg\ calc'd from\ Gal + ppmAg\ calc'd from\ Fah$$
$$\boldsymbol{STEP\ 4} + \boldsymbol{STEP\ 8}$$

STEP 10: Determine **Actual Total** ppmAg in rock (from XRF): $= Measured\ ppmAg\ from\ XRF$

STEP 11: %Ag due to Galena by:

$$= 100\ * \frac{cal'd\ ppm\ Ag from\ Gal}{total\ ppm\ Ag} = \%Ag\ due\ to\ Galena$$
$$\boldsymbol{STEP\ 4/STEP\ 9}$$

Table 5-1 Ag Accounting Example

Sample 201-2:

Galena contains (std composition):	86.6	wt% Pb	14.4	wt% S
Galena contains (from microprobe):	0.16	wt% Ag		
	1600	ppm Ag		
$\frac{\text{ppmAg}}{\%\text{Pb}}$	18.5	$= \frac{\text{ppmAg}}{86.6\%\ \text{Pb}}$		
%Pb in Rock (from XRF):	16.5	wt%		
Ag calc'd from Galena:	305	=(%Pb in rock (from XRF)) x (ppmAg/%Pb)		
Fahlore contains (from microprobe):	5.0	wt% Ag	27.5	wt% Sb
	50000	ppm Ag		
$\frac{\text{ppmAg}}{\%\text{Sb}}$	1821	$= \frac{\text{ppmAg}}{\%\ \text{Sb}}$		
%Sb in Rock (from XRF):	0.10	wt%		
Ag calc'd from Fahlore:	187	=(%Sb in rock (from XRF)) x (ppmAg/%Sb)		
Calculated total Ag in rock (ppm):	492	=Ag calc'd from Gal + Ag calc'd from Fah		
Actual total Ag in rock (ppm from XRF):	459	=measured amount of Ag from XRF		

Calculated and Measured agree within 10%

%Ag due to Galena:	62	=100*(Ag calc'd from Galena/Calc'd total Ag in rock)